Ultrahigh Resolution Optical Coherence Tomography for the Detection of Early Stage Neoplastic Pathologies

by

Pei-Lin Hsiung

M.S. in Electrical Engineering
Massachusetts Institute of Technology, 2000
B.S.E. in Electrical Engineering
Princeton University, 1997

Submitted to the
DEPARTMENT OF ELECTRICAL ENGINEERING AND COMPUTER SCIENCE
in partial fulfillment of the requirements for the degree of
DOCTOR OF PHILOSOPHY in ELECTRICAL ENGINEERING AND
COMPUTER SCIENCE

at the

MASSACHUSETTS INSTITUTE OF TECHNOLOGY
April 2005

Signature of Author:_____
Department of Electrical Engineering and Computer Science
April 2005

BARKER

Certified by:_____
James G. Fujimoto
Professor of Electrical Engineering
Thesis Supervisor

Accepted by:_____
Arthur C. Smith
Chair, Department Committee on Graduate Students

Ultrahigh Resolution Optical Coherence Tomography for the Detection of Early Stage Neoplastic Pathologies

by

Pei-Lin Hsiung

Submitted to the Department of Electrical Engineering and Computer Science
in April, 2005 in Partial Fulfillment of the
Requirements for the Degree of
Doctor of Philosophy

ABSTRACT

Identification of changes associated with early stage disease remains a critical objective of clinical detection and treatment. Effective screening and detection is important for improving outcome because advanced disease, such as metastatic cancer, can be difficult to impossible to cure. Many existing diagnostic modalities, including x-ray imaging, magnetic resonance imaging, ultrasound, and endoscopy do not have sufficient resolution to detect changes in architectural morphology associated with early neoplasia and other pathologies. Diagnostic modalities capable of identifying pre-malignant tissue at an early stage could therefore significantly improve treatment outcome.

Optical coherence tomography (OCT) is an emerging biomedical imaging technique that can potentially be used as an *in vivo* tool for identifying early stage neoplastic pathologies. Recent advances in solid-state laser and nonlinear fiber technology have enabled the development of ultrahigh resolution and spectroscopic OCT techniques which promise to improve tissue differentiation and image contrast. Previous *ex vivo*, benchtop ultrahigh resolution OCT imaging studies suggest that differentiation of architectural morphology associated with pathology is feasible. This thesis covers the development and investigation of ultrahigh resolution OCT for studies of early neoplastic pathologies. A section of this thesis will focus on development and evaluation of a novel turn-key broadband source for OCT. Feasibility studies were performed using ultrahigh resolution OCT for imaging human tissues *ex vivo* in the clinical pathology laboratory setting. Imaging results will be presented examining a variety of normal and neoplastic lesions in preliminary studies of the thyroid gland, large and small intestine, and breast. These experiments elucidate the optimal imaging parameters, potential and limitations of the technique, and establish the microstructural markers visible in OCT images that are characteristic of pathologic tissues. These studies establish a baseline which should help interpret future *in vivo* ultrahigh resolution OCT imaging studies.

Thesis Supervisor: James G. Fujimoto
Title: Professor of Electrical Engineering

Dedication

To My Family

For their love, support, and sacrifice

Acknowledgements

Biomedical research is a particularly difficult field because it requires the participation and interaction of people with different backgrounds and training. Boundaries between disciplines must be overcome and new languages must be learned in order to facilitate work toward the common goal of improving healthcare and quality of life. I have been fortunate in my graduate career to be surrounded by extremely dedicated people who have each brought their hard work and expertise to support the projects discussed in this thesis.

I would first like to thank Prof. James Fujimoto, my thesis advisor at MIT. He has provided the opportunity, resources, and freedom to complete this thesis. His guidance and patience in sharing his many years of experience in this field will always be appreciated.

Drs. Liron Pantanowitz, Darshan Phatak, James Connolly, and the residents, fellows, and support staff in the pathology department at Beth Israel Deaconess Medical Center provided their time, expertise, and innumerable surgical specimens to support this work. I am grateful for their willingness to put up with the constant prowl of someone with no medical background in their grossing room. I particularly thank Gene Mercado for his help preparing slides and his patience with our special tissue orientation and registration requirements.

Dr. Hiroshi Mashimo of the Boston VA Healthcare System provided careful reading and insightful feedback of many drafts of our colon manuscript. His continued enthusiasm and support as been the driving force behind our gastrointestinal projects.

Sergei Popov, Cristiano de Matos, and Prof. Roy Taylor at the Imperial College in London developed the Raman light source and were gracious to bring it to MIT for our group to characterize and evaluate for OCT.

Back at MIT, Dr. Prashant Nambiar in the Division of Comparative Medicine at MIT provided guidance and helped interpret our tissue preservation study. Katie Madden has helped our group of novice animal handlers treat our furry experimental friends with respect and compassion. Kathy Cormier in DCM, like Gino at the BIDMC, supported our in-house histology requirements with skill and patience.

In the optics group at MIT, I am grateful to Dorothy Fleischer and Cindy Kopf for their help keeping the group running smoothly and for their pearls of wisdom.

Current group members Yu Chen, Aaron Aguirre, and Tony Ko have provided their expertise for all of the projects discussed in this thesis. I admire Yu for his patience, Aaron for his perseverance, and Tony for his frankness in speaking his mind. I hope to someday live up to the examples of Kaoru Minoshima, Thomas Schibli, Ingmar Hartl, and Stephane Bourquin, former

postdocs whom I respect for being both great scientists and great people. Aurea, Robert, and Vikas have been recent officemates whom I sincerely thank for providing distraction and putting up with my grumpiness over the last years as I finish my thesis. I promise to be a more pleasant person soon! I have yet to really get to know Maciej, Kenji, Vivek, Mariana, and Kenya, but I hope that we will have the opportunity to be colleagues again in the future. The world is an amazingly small place. John Fini, my officemate for many years before he moved on to better things, taught me an appreciation for good coffee when combined with good company. Juliet Gopinath and I started in the optics group together and our research has since taken us in separate directions. I have appreciated our conversations about life and lab over the years, and I will always remember our shared experiences in the SAA studio, our home away from lab. And Drew, you better keep playing baseball because I'm never going to stop playing ultimate!

Over the many times life has been difficult over my graduate career, my longtime friend and roommate Eden Miller Medina has always been there for a warm hug and a witty joke to remind me of the value of humor in any situation. I wouldn't be here without her. Nicole Morgan and I shared studio time and many thoughtful-provoking conversations over excellent coffee at the former Tosci's. With Erik Deutsch I have imbibed many glasses of fine beverage over the years. His hard work and love for his family and friends blows me away. Christine Chin made an entrance into my graduate life right when I needed her. She has provided support, adventure, and inspiration to the half of my brain which never seems to get enough exercise. I will always love her for being who she is.

Finally, I certainly wouldn't have survived the roller-coaster that is MIT without the camaraderie of the Boston ultimate scene. James and Stacy McGeever Sarvis, mom and pop of MIT women's ultimate, taught me that there is more to ultimate than just overwhelming your opponent with sheer analytical ability – heckling is also important. Tessa Warren, friend and sometime coach, was an inspiration as a player, graduate student, postdoc, and now professor. My various teammates on MIT, Bad Egg and Rogue are too many to name. Through these years they have together provided encouragement, community, and remind me that family is the most important thing in life.

Table of Contents

Chapter 1

Introduction

Overview

According to the America Cancer Society, almost 574,000 Americans are expected to die of cancer in 2004. Cancer is the second leading cause of death in the United States, exceeded only by heart disease.[1] Despite these grim statistics, the age-adjusted mortality rate for the four most common cancer types have remained constant or declined since 1990.[2] Greater awareness of risk factors, improvements in screening methods and increased compliance with screening guidelines, and advances in treatment have undoubtedly improved patient outcome.

As with any disease, early detection and treatment can significantly improve patient prognosis. Detection of cancer at an early stage before it becomes metastatic increases treatment options. For these reasons, techniques for early cancer detection and treatment are active fields of research. Optical coherence tomography (OCT), emerging optical imaging technique capable of rapid noninvasive imaging of tissue cross-sectional microstructure, could provide a useful adjunct to current diagnostic tools for detecting early stage cancer and managing treatment once disease is diagnosed.[3, 4] Early *ex vivo* studies in our group suggested the feasibility of using OCT for the detection of early neoplasia in the reproductive, gastrointestinal, respiratory, and urinary tracts. [5-9] Recent advances in OCT technology have improved imaging resolution and speed, enabling ultrahigh resolution OCT imaging in the clinical setting to be performed.

In order to provide a background for the remainder of this thesis, this introductory chapter will give a brief overview of cancer management, highlighting the role of various emerging imaging techniques. The advantages and shortcomings of these imaging techniques will be discussed. Optical coherence tomography will then be presented as a method to overcome some of these shortcomings. Finally, foreseeable limitations of OCT will be discussed.

Cancer Management

Cancer is a group of diseases characterized by genetic alterations that result in loss of the normal control mechanisms that regulate cell growth, morphogenesis and differentiation, often termed "neoplasia." Normal cell growth is accompanied by orderly development and specialization. In contrast, all cancers are associated with genetic mutations which alter cell growth and division. Roughly 5-10% of all cancers are associated with an inherited genetic component that predisposes the patient to a significantly increased risk of a particular cancer.[2] The remainder are associated with genetic mutations which may result from internal factors, such a hormonal effects, or external factors, such as smoking, exposure to carcinogenic toxins, or sunlight.[10] Viruses have also been implicated in the development of cancer.[11, 12] Not all neoplasms are malignant, and those that are invade and become metastatic through complex multi-step processes. After initial cell proliferation, secretion of several angiogenic factors and neovascularization from the surrounding tissue must occur if the tumor mass is to grow beyond a few millimeters in size.[13, 14] Invasion of the host stroma occurs[15, 16] and tumor cells spread to locations throughout the body via the lymphatic and vascular system resulting in secondary tumor development in specific host sites.[17] Once metastatic cancer is established, treatment efficacy is often limited.

Cancer exacts a costly toll in human suffering, lost productivity, and cost associated with medical care. However, many cases of cancer in the United States could be prevented by reducing exposure to known risk factors. Of the estimated 563,700 cancer deaths expected to occur in the United States in 2004, approximately 32% will be caused by tobacco use.[2] Roughly one-third will be related to poor nutrition, physical inactivity, overweight/obesity, and other lifestyle factors.[18] Poverty is the most critical factor affecting health and longevity, influencing lifestyle factors such as tobacco use and obesity, awareness of and compliance with screening guidelines, and access to appropriate medical care.[19] Significant disparities in cancer incidence, mortality, and survival exist between various demographic and socioeconomic groups. In an effort to reduce the disparity that exists in the socioeconomically disadvantaged, the American Cancer Society is working to raise awareness of inequalities in health care through education and advocacy at the local through federal levels, lobbying for increased funding for targeted research, and developing outreach services tailored to be culturally appropriate and language-specific for underserved communities. The ultimate goal of these efforts is to reduce cancer incidence and mortality and increase cancer survival in disadvantaged groups to levels comparable to that of the general population.[2]

Surveillance and Early Detection

Early detection of cancer is important because it increases the likelihood of treatment being effective. Surveillance tests must detect early stage disease at a point where appropriate treatments exist. The likelihood of the particular disease progressing to a more advanced stage must also be taken into consideration. The most appropriate candidates for surveillance are therefore cancers which are associated with significant morbidity, high prevalence of detectable early stage disease, possibility of improved outcome because of early detection due to availability of improved early stage treatments methods, and existence of an effective, low-cost screening test.[20] Surveillance and screening programs have been shown to reduce mortality

associated with cancers of the breast, cervix, colon and rectum. Surveillance programs have also been linked to reduced mortality associated with other cancers, but studies are less conclusive.[2] An unfortunate number of cancers are still discovered only after the onset of secondary symptoms.

Staging

Cancer is further described as *in situ* if it is confined to the tissue of origin. The goal of early detection would be to identify disease at an *in situ* stage or earlier, before the onset of either local invasion or metastasis.

Once a diagnosis of cancer is established, the disease must be staged in order to estimate patient prognosis and determine appropriate treatment. Staging is the process used to describe the extent or spread of disease with malignant potential from the site of origin. Summary descriptive staging systems are used to categorize invasive cancers as local (confined to organ of origin), regional (extension into surrounding organs, tissues, or involvement of regional lymph nodes), or distant (spread to regions remote from primary tumor). The commonly used TNM staging system classifies tumors into categories based on extent of the primary tumor (T), involvement of lymph nodes (N), and absence or presence of metastasis (M). Stage numbers I, II, III, and IV further subdivide these categories into early (I) through late stage (IV). [2]

Treatment

Treatment methods depend on the stage of the cancer and in many cases on the particular cancer subtype. The benefit of treatment must be balanced with age, the overall health of the patient, and treatment risk. This is especially important as over 76% of cancers occur in people age 55 and over.[2] Radiation therapy is one of the most common treatments for cancer. Over half of all cancer patients receive radiation at some point in their treatment process, whether as the sole treatment or as adjuvant therapy post-surgery to eliminate possible residual disease. Radiation is usually given locally through external means or through internally delivery via a radioactive implant. Because it is given locally, side-effects are usually limited to the region of treatment.[21] Chemotherapy, in contrast, is a systemic treatment which is useful for dealing with metastatic disease. More recently, drugs can be targeted to local regions by local delivery methods such as infusion pumps or controlled release implants. Chemotherapeutic drugs exist to cure disease, control disease spread, and provide palliative care. Chemotherapy is also used as neoadjuvant therapy to shrink the size of a tumor before subsequent radiation treatment or surgery. Combinations of adjuvant therapies are also commonly used with surgery.[22] Surgical procedures themselves are the oldest form of cancer treatment. Advances in surgical techniques have enabled procedures to be performed less invasively, often resulting in improved outcome and shorter recovery time. Surgery also maintains an important role in staging of disease.[23]

In addition to radiation, chemotherapy, and surgery, promising recent advances in harnessing the body's natural immune system to fight cancer have led to the development of immunotherapy, now considered a fourth treatment type for a number of cancers. Two categories of immunotherapy include non-specific immunotherapies, which stimulate the immune system to fight any cancer cells present, and monoclonal antibodies, which can be targeted to antigens

produced by cancer cells or cancer-associated targets. Interleukin-2 was the first FDA-approved immunotherapy for primary (non-adjuvant) use in treating advanced cancer.[24] Interferons and other cytokines, which are produced naturally by white blood cells in the body in response to infection, have also been demonstrated to have an anti-tumor effect. Interferon-alfa, one of the first interferons shown to slow tumor growth, is now FDA-approved for use for the treatment of a number of cancers such as hairy cell leukemia, malignant melanoma, and follicular lymphoma.[25] Monoclonal antibodies have been widely used in scientific studies of cancer, as well as in cancer diagnosis.[26] As a therapy for cancer, monoclonal antibodies can be injected into patients to identify cancer cells and potentially disrupt activity or enhance immune response against the disease. Many clinical trials using monoclonal antibody treatments are underway, and the FDA has approved several approaches for treating breast cancer, non-Hodgkin's lymphoma, acute myelogenous and chronic lymphocytic leukemia, and colorectal cancer.[27] Much current research is directed toward developing further methods to link cytotoxic drugs or radioisotopes to monoclonal antibodies to enhance their specificity for tumor cells. The development of highly specific delivery mechanisms could greatly enhance both early detection and treatment.

Imaging Techniques in Cancer Management

Of the many imaging techniques employed in cancer management, the only proven effective imaging technique associated with cancer screening and improved patient outcome is low-dose x-ray mammography for breast cancer.[28] Increased use of mammography has been credited in part for the majority of new breast cancer cases which are now detected at a localized stage, where the five-year survival rate is currently 97%.[18] Newer methods such as spiral computed tomography (spiral CT) are being investigated for efficacy and cost-effectiveness as a screening tool for lung cancer.[29, 30] Magnetic resonance imaging (MRI) and positron-emission tomography (PET) have also been investigated,[31, 32] but because of their complexity, cost, and limited sensitivity, have been used primarily for research investigations and for assessing distal involvement.[33, 34] Transvaginal and transabdominal ultrasound have been investigated for screening for ovarian cancers in high-risk populations because of the significantly increased mortality associated with metastatic disease. [35, 36] With the exception of mammography, all of these techniques are used after initial symptoms have arisen, and are unable to detect early stage disease or assess abnormal lesions before they become invasive.

Once advanced disease is suspected, techniques such as CT and MRI provide high resolution three-dimensional information useful for localizing lesions and staging disease for further therapeutic procedures. Ultrasound has also been widely used and can be effective for a variety of diagnostic applications. However, the effectiveness of ultrasound is operator-dependent and limited to situations where direct probe contact is possible. Scarring and calcifications can complicate ultrasound image interpretation. The presence of air also presents a formidable barrier to ultrasound imaging, limiting applications in the respiratory tract.[37] Transrectal ultrasound and MRI has also been investigated for preoperative staging of prostate cancers,[38] but effectiveness has been limited due to inability to determine microscopic spread of disease. [34] More recently, endoscopic ultrasound (EUS) has proven itself to be a useful tool in the assessment and staging of esophageal cancer[39] and is being investigated for other organ systems.[37, 40-42] Endoscopic ultrasound enables higher resolution imaging than CT and MRI and

can enable detection of some lesions less than 5 mm in diameter. However, EUS imaging is still plagued by the fundamental resolution and contrast limitations of ultrasound.

A relatively new approach being investigated for gastrointestinal applications is real-time magnification of endoscopic views to enable high-resolution imaging of mucosal surface features, known as magnification endoscopy. Magnification endoscopes include adjustable focusing mechanisms that allow magnification of the endoscopic image by 1.5x to 150x.[43] Magnification endoscopy is designed to be used with topical application of dyes such as methylene blue to enhance visualization of mucosal structures. Improvements in endoscope CCD technology have increased pixel densities from 100,000 to 200,000 pixels for conventional endoscopes to 850,000 pixels some of the newest commercially available endoscopes.[44, 45] These high-resolution magnification endoscopes are capable of visualizing structures as small as 10-71 microns in diameter,[45] and have been investigated for assessing flat colonic lesions and polyps,[46, 47] Barrett's esophagus,[48] and esophageal adenocarcinoma.[49] While initial results are promising, insufficient data exists to suggest routine use of magnification endoscopy in clinical procedures.

Limitations of Biopsy

Regardless of type of cancer, however, confirmation of the existence of disease is still based on the "gold standard" of microscopic examination of representative tissue specimens obtained from the suspicious lesion. Methods to obtain tissue samples include: fine-needle aspiration (FNA) biopsy, used for the breast and hard-to-reach organs such as lung and liver; core needle biopsy, which is more invasive than FNA but obtains more histologic material; cone biopsy, used to diagnose and sometimes treat cervical cancer; endoscopic biopsy, performed in luminal organs under visual endoscopic guidance; surface and punch biopsy, used for easier-to-access areas such as skin and oral mucosa; and excisional and incisional biopsy.[50] The particular type of biopsy method chosen depends on the tissue type being sampled, how suspicious the lesion appears from previous diagnostic tests, the location and number of suspicious lesions, the general health and preference of the patient, as well as the technical expertise available at the host hospital.

The choice of appropriate treatment ultimately depends on accurate and definitive diagnosis. Although histologic assessment remains the gold standard by which a diagnosis of cancer is determined, conventional biopsy followed by cytology or histolopathology still suffers from a number of limitations which affect diagnostic outcome. Early disease, such as dysplasia and *in situ* carcinoma, may not be visible using clinically available imaging methods. Ultrasound and CT are often used to guide biopsy procedures for macroscopic lesions, but cannot identify early disease or visualize the full extent of abnormal lesions because of the limited imaging resolution and contrast. Screening biopsies, which are performed in patients with conditions which predispose them toward developing certain cancers, are often performed using unguided sampling protocols. An imaging technique capable of detecting early neoplastic changes and microscopic invasion could therefore complement existing diagnostic modalities by guiding biopsy, reducing sampling error and false negative rates, and guiding interventional procedures.

Optical Coherence Tomography

Optical coherence tomography (OCT) is an emerging biomedical imaging technology which permits rapid, noninvasive imaging of tissue microstructure *in situ* and in real time.[3, 4] OCT is similar to ultrasound, except that near-infrared light is used instead of sound to probe tissue internal structure. OCT detects backscattered light from different depths within a tissue sample, thus generating a two-dimensional map of optical scattering as a function of depth. Optical coherence tomography has several advantages over existing clinical imaging techniques which make it attractive for a number of applications. OCT has resolutions higher than clinical ultrasound and imaging can be performed without contact and without the use of a tranducing medium. In addition, since OCT is an optical imaging technique, it can be incorporated into a number of imaging devices such as laparoscopes, fiber-optic catheters, and imaging needles.[51-53]

Since the technique was initially reported in 1991, optical coherence tomography has been extensively investigated in ophthalmology,[54-59] in part because of the unique accessibility of the anterior and posterior eye to optical imaging techniques. The lack of a competing clinical technology for cross-sectional imaging of retinal microstructure has led to relatively rapid development and adoption of OCT technology for ophthalmology as an adjunct to standard clinical care. Progress has also been made in the development of OCT for high-resolution catheter-based imaging of architectural morphology associated with cardiovascular disease.[60-63] Feasibility studies have also been performed in preliminary studies of the respiratory, female reproductive, and urinary tracts.[6-8] With the development of fiber optic catheters, *in vivo* endoscopic OCT imaging in an animal model was demonstrated.[51] Today, with the exception of ophthalmology and cardiology, the majority of *in vivo* OCT investigations have been pursued in the gastrointestinal tract.[64-73] Much of this clinical work has focused on the upper gastrointestinal tract, where excellent sensitivities and specificities have been demonstrated for detecting Barrett's esophagus, a condition which predisposes patients to increased risk of developing esophageal adenocarcinoma.[72] Recent work has shown that OCT has potential to distinguish hyperplastic from adenomatous polyps in the colon.[73]

OCT for early detection

Over 55% of new cancer cases in the United States in 2004 will occur in the lung and bronchus, breast, prostate, colon and rectum.[2] Of these new cases, approximately 95-98% will be cancers of epithelial origin, known as "carcinomas." Early detection techniques would be particularly powerful if epithelial abnormalities known as dysplasia could be identified. Advanced stages of dysplasia are correlated with high likelihood of progressing into cancer.[74, 75] Dysplastic tissue exhibits specific alterations in epithelial cells which are typically characterized histologically. These can include dark-staining nuclei (hyperchromatism), enlarged and prominent nuclei, increased mitotic figures (indicating abnormal cell division), and increased nuclear-to-cytoplasmic (N/C) ratio. Epithelial cells may also appear crowded and bunched together. In stratified squamous epithelium, abnormal cell maturation from the basal layer to the superficial layer is also a hallmark of dysplasia. These microstructural changes affect the optical scattering properties of the epithelium and may be detectable using OCT. Dysplastic changes may also be associated with architectural changes, such as alterations in the size, shape, and distribution of glandular structures. Specific mucosal pit patterns viewed using magnification endoscopy have

been correlated with neoplastic colonic lesions well as Barrett's esophagus.[76, 77] While identification of features associated with cellular-level changes may prove to be difficult, OCT may still enable identification of neoplastic lesions based on architectural microstructure.

The large numbers of patients involved in studies performed in the upper gastrointestinal tract indicates significant interest in the potential of OCT for detecting early stage esophageal cancers. Carcinomas of the gastrointestinal tract are particularly amenable to catheter-based imaging techniques. Current endoscopic methods for biopsy guidance provide only surface information and are prone to sampling errors. If microstructural changes associated with early stage neoplasias prove to be visible, OCT could be used to guide excisional biopsy, potentially increasing diagnostic yield and reducing false negative rates. OCT could also potentially be used to identify tumor margins and guide minimally invasive surgery.

Limitations of OCT

While OCT is promising for detecting a number of architectural changes associated with early neoplastic lesions, a number of limitations exist which may eventually limit the role of OCT in cancer management. OCT performs imaging using light in the near-infrared range, avoiding the primary absorption bands of water and the primary tissue chromophores. Even in this wavelength range, OCT image penetration depth is limited to a few millimeters because of depth-dependent attenuation due to scattering. Variations in penetration depth are apparent in individual images which are composed of different tissue constituents, complicating image interpretation. Adipose tissue and certain protein colloids, for example, exhibit less attenuation than fibrous connective tissue. While the penetration depth can be increased to some degree by increasing optical power used for imaging, incident power is ultimately limited by American National Standards Institute (ANSI) values established to prevent tissue damage. Imaging sensitivity can also be increased at the expense of imaging speed. However, the penetration depth in OCT images should be sufficient to assess mucosal microstructural features associated with most hollow organs. OCT imaging may therefore complement standard ultrasound by providing high resolution assessment of mucosal features which cannot be visualized using current imaging methods. In addition, OCT imaging needles may eventually enable imaging of solid organs. In this scenario, image penetration depth would primarily be limited by the depth of insertion of a needle-based device.

The most significant limitation of OCT may be inherent lack of contrast between structures which must be visualized in order to differentiate normal tissue from neoplastic pathology. Although it is recognized that the source of contrast in OCT is related to tissue microstructure and index of refraction, the nature of this relationship is still poorly understood. Light scattering in tissue is affected by the shape, size, and distribution of tissue constituents and their relative indices of refraction. Various theoretical models have been proposed which suggest that the primary sources of scattering in tissue are cellular components on the order of the wavelength of the incident light or smaller.[78, 79] For imaging in the 600-1400 nm near-infrared range, this suggests that nuclei, other cytoplasmic organelles, and membranes strongly contribute to tissue scattering. In addition, scattering would also be expected from supporting tissue constituents such as collagen, which range from ~100 nm diameter individual fibrils to several micron diameter bundles.[80] The utility of OCT for differentiating normal tissue from pathology will therefore likely depend on alterations in normal scattering properties of these constituents which

can be detected using OCT. This suggests that new diagnostic criteria for early cancers different from those used in standard histopathology may need to be developed in order to realize the full potential of OCT as a diagnostic tool. Research and development focused on novel contrast mechanisms may eventually overcome the inherent visualization limitations of standard scattering intensity-based OCT imaging.[81-84]

Scope of Thesis

The main goal of this thesis is to investigate the hypothesis that OCT can be used as an *in vivo* tool for the identification of early neoplastic pathologies. Previous *ex vivo*, benchtop ultrahigh resolution OCT imaging studies have suggested that differentiation of architectural morphology associated with neoplastic pathology is feasible. However, imaging in the laboratory setting limited access to tissue and imaging could often only be performed on fixed specimens or postmortem tissue. Recent advances in solid-state laser and nonlinear fiber technology have enabled the development of ultrahigh resolution and spectroscopic OCT techniques which can now be used in the clinical setting.

This thesis covers the development of a new source for ultrahigh resolution OCT imaging and investigation of the performance of ultrahigh resolution OCT for studies of several human early neoplastic pathologies in the clinical setting. In Chapter 2, the development and evaluation of a novel broadband source for OCT will be presented. This source is compact, turn-key, and should enable a wide range of new ultrahigh resolution, high-speed, OCT imaging applications. Early features of cancer are often focal, with diagnosis which may often differ from slide to slide. Precise registration with histology is therefore required for correlation of OCT imaging with pathology and accurate interpretation. Chapter 3 first presents ultrahigh resolution OCT imaging *in vivo* and *ex vivo* in an animal model to investigate the effects of tissue preservation and fixation on optical contrast. This study establishes proper specimen handling protocol for *ex vivo* imaging as well as provides a reference for interpreting histologic correlation with OCT in a model system with representative tissue constituents. Chapters 4-6 will then present results examining normal and neoplastic lesions in the thyroid gland, large and small intestine, and breast. These studies establish a baseline which should help interpret future *in vivo* ultrahigh resolution OCT imaging studies. Finally, Chapter 7 discusses possible future work investigating OCT for identifying markers of dysplasia and presents preliminary *in vivo* ultrahigh resolution OCT imaging results in the human gastrointestinal tract.

Chapter 2

High-power, Continuous-wave, Raman Continuum Light Source for Optical Coherence Tomography

INTRODUCTION

Optical coherence tomography (OCT) is an emerging biomedical imaging technology that can perform high-speed, micron scale, noninvasive imaging of tissue morphology *in vivo*. The principles of OCT have been described previously.[3, 4] Since OCT is based on low-coherence interferometry, the axial image resolution, Δz, is determined by the bandwidth $\Delta\lambda$ and the center wavelength λ_0 of the light source: $\Delta z = [2\ln(2)/\pi](\lambda_0^2/\Delta\lambda)$. Standard OCT systems use superluminescent diode light sources, which achieve an axial resolution of 10-15 μm. Compact and portable high performance broadband light sources with sufficient power and bandwidth are important to achieve ultrahigh resolution, high-speed OCT imaging outside the laboratory setting.

Femtosecond solid-state lasers have been demonstrated to directly generate broad bandwidths which can be used for ultrahigh resolution OCT imaging, but are difficult to operate outside the laboratory.[85, 86] Nonlinear and microstructure fibers pumped by femtosecond bulk and fiber systems have also enabled imaging with unprecedented resolutions, but require the use of femtosecond lasers.[87-89] Reductions in cost can be achieved using low-threshold femtosecond lasers which use inexpensive low-power pump lasers, but these systems are still relatively complex.[90, 91] Femtosecond fiber laser-based sources promise to be compact and robust.[92] The 1300 nm wavelength region is of particular interest for biomedical applications because it permits improved imaging depth when compared with shorter wavelengths due to reduced scattering in biological tissue.[93] The development of broadband light sources for OCT imaging in scattering tissue has therefore focused on this wavelength range.[87, 89, 92, 94] Recent work has also investigated light source development and imaging in the 1000-1100 nm wavelength range, which provides a compromise of higher resolution for a given bandwidth at the expense of reduced image penetration.[95, 96] A portable source suitable for *in vivo* clinical applications has been demonstrated in this wavelength range using a femtosecond diode-pumped Nd:Glass laser with a highly nonlinear fiber.[96]

This chapter describes a novel approach for broadband continuum generation in microstructure fibers using a high-power, continuous-wave, all-fiber pump light source. This new light source promises to enable ultrahigh resolution, high-speed OCT imaging with lower cost and complexity than with femtosecond laser-based light sources. Microstructure fibers typically have been pumped with femtosecond lasers to provide the peak powers necessary to initiate nonlinear effects for continuum generation under conditions of anomalous or near-zero dispersion. However, the use of high intensity femtosecond pulses for broadband continuum generation under these conditions leads to severe spectral modulation of the continuum in the vicinity of the pump wavelength. This spectral modulation produces sidelobes and reduced contrast in the interferometric axial point spread function which degrades OCT image contrast. Femtosecond pumping of microstructure fibers may also result in excessive temporal instability of the continuum and nonlinearly amplified quantum noise, which can lead to excess intensity noise.[97]

An alternative to using high peak powers is to increase the effective nonlinear interaction length of the Raman interaction, which is governed by optical losses in the fiber and dispersive walk-off between the pump and continuum pulses. The use of longer pump pulses reduces this dispersive walk-off effect. Stimulated Raman scattering has been shown to be the principle nonlinearity for continuum generation by using nanosecond-scale pump pulses.[98, 99] Recently, the possibility of low peak power and even continuous-wave, multiwatt Raman continuum generation in highly nonlinear fibers has been demonstrated.[100] Continuous-wave pumping of nonlinear fibers can enable the development of robust and turnkey continuum light sources which require no optical alignment, enabling high-speed, ultrahigh resolution OCT imaging in a wide range of applications outside the laboratory.

This chapter demonstrates a new light source for ultrahigh resolution, high-speed OCT imaging using Raman continuum generation from a continuous-wave pumped microstructure fiber. This source achieves bandwidths of ~140 nm in the 1300 nm wavelength range with output powers of 330 mW, higher than achieved using any other technique. The light source is compact (25 x 25 x 20 cm), robust, completely turnkey, and requires no optical alignment. Ultrahigh resolution, high-speed OCT imaging is demonstrated with < 5 μm axial resolutions. High-speed ultrahigh resolution imaging is demonstrated *in vivo* in the hamster cheek pouch and in human skin.

SYSTEM PARAMETERS

The broadband all-fiber Raman continuum light source was based on a 10 W continuous-wave, non-polarized, multimode diode-pumped, single-mode Yb-fiber laser (IPG Photonics) directly spliced to an anomalously dispersive microstructure fiber (Crystal Fiber). The microstructure fiber was 100 meters long, had a dispersion of +35 ps nm^{-1} km^{-1}, a pitch of $\Lambda = 1.72$ μm, and an air-hole diameter of 0.65 μm. Figure 2.1 shows a schematic of the source and the Raman continuum output. The Raman-soliton continuum had 5.5 W of total power and a spectral width of 318 nm (at 20 dB). The spectral range from 1090 to 1370 nm was flat to ±5 dB and contained 2.3 W of power. This output was filtered using a special WDM coupler to remove the pump wavelength and to achieve a smooth, Gaussian-like spectrum in the 1300 nm wavelength range. Figure 2.2A shows a typical spectrum before and after spectral shaping by the WDM coupler. The output power after the coupler was ~330 mW and the spectrum was Gaussian-shaped with a

bandwidth of ~140 nm, corresponding to a theoretical resolution of 5 μm in free space. The all-fiber light source contains no bulk optical components, requires no alignment, and is turnkey, compact and robust.

The intensity noise of the light source system was characterized using an RF spectrum analyzer. Figure 2.2B shows the noise spectrum of the Raman continuum generated by the source, the detection system noise, and the calculated shot noise level. Excess intensity noise is caused in part by feedback from the fiber-grating-based design of the Yb pump laser and reflection from the splices between the microstructure fiber and the pump laser and WDM coupler. Dual-balanced detection was used in the OCT system to reduce excess intensity noise.

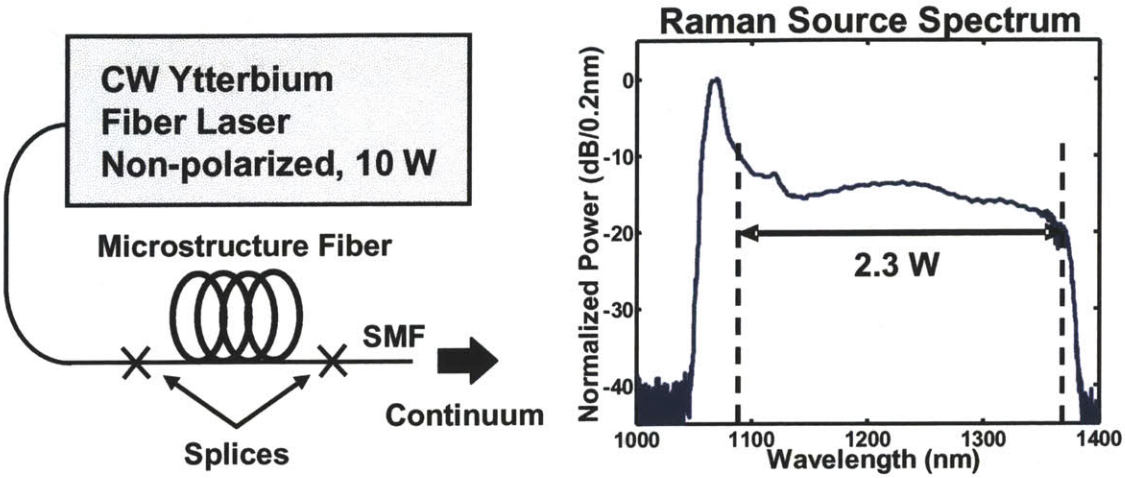

Figure 2.1: Left, Schematic of Raman continuum source. SMF: Single-mode fiber. Right, Output spectrum. The output was 5.5W total, with 2.3 W in the spectral range from 1090 to 1370 nm. The output was filtered using a special WDM coupler to remove the pump wavelength and shape the spectrum.

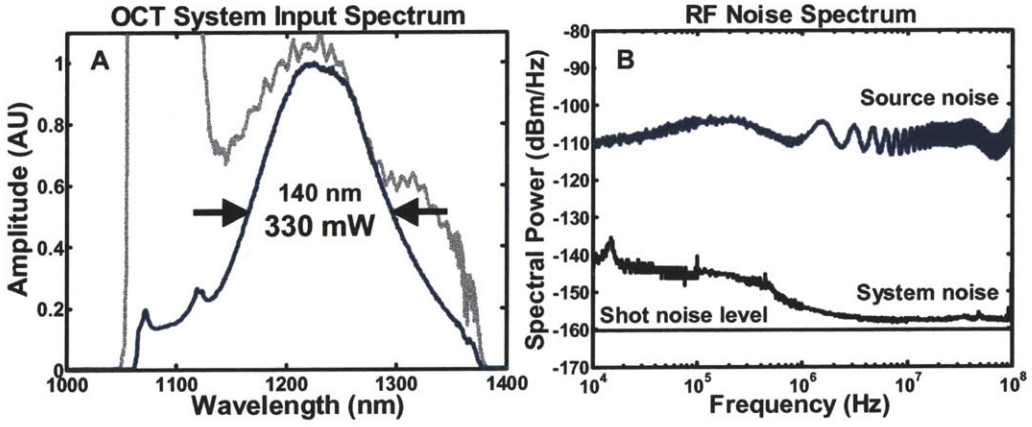

Figure 2.2: A. Typical output spectrum of the Raman fiber light source before and after spectral shaping. B. RF noise spectrum. High frequency oscillations are caused by spurious reflections from the fiber splices. Dual-balanced detection is used to reduce excess noise.

Figure 2.3 shows the schematic of the experimental setup for OCT imaging. The system consists of a dual-balanced interferometer with broadband 80/20 and 50/50 fiber couplers to optimize power coupled back to the detectors. The reference arm was scanned using a reflective delay scanner at a velocity of 6.2 m/s and 1600 Hz repetition rate. Polarization controllers were used in both the sample arm and the reference arm. Dual-balanced detection with two InGaAs photodiodes (D1 and D2) was used to reduce excess intensity noise in the light source. Since the interference signal occurs 180 degrees out of phase at the two detectors, subtracting the two signals adds the heterodyne interference signal but subtracts excess noise. The input to photodiode D2 is attenuated to match the input to photodiode D1. It was important to match the path lengths of the two arms of the double-detector receiver in order to achieve optimum noise reduction.[101] The interference signal was electronically bandpass filtered, logarithmically demodulated, low-pass filtered, and digitized. Detection was performed at a Doppler frequency of 9.8 MHz with a bandwidth of 1.2 MHz.

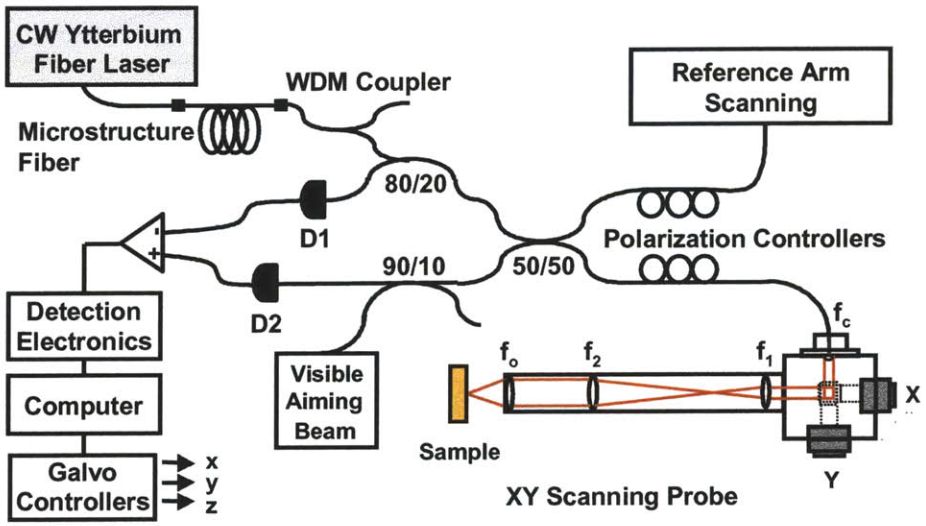

Figure 2.3: Schematic of high-speed, ultrahigh resolution OCT system using an all-fiber Raman continuum light source. The system uses broadband 80/20 and 50/50 couplers to optimize the power on the sample and coupled back to the detectors. Dispersion was matched in the sample and reference arms of the interferometer in order to maintain high axial resolution.

In vivo imaging was performed using an XY galvanometer scanning probe. Near-infrared achromatic lenses were used to minimize chromatic aberration. The fiber collimating lens had a focal length of $f_c = 10$ mm, followed by a Hopkins relay pair of lenses with focal lengths $f_1 = 25$ mm and $f_2 = 40$ mm, and an objective of focal length $f_o = 25$ mm. A pair of galvanometer-controlled scanning mirrors was used between the fiber collimating lens and the Hopkins relay to perform high-speed transverse scanning. The focused spot size was $2\omega_0 = 18$ µm, corresponding to a full-width-half-maximum of ~11 µm. To minimize the effect of wavefront aberration, dehydration, and to achieve better index matching, the tissues were irrigated with saline and covered with a thin cover glass.

RESULTS

The performance of the OCT system using the fiber Raman continuum light source was characterized using an isolated reflection from a single mirror. To maintain axial resolution, the dispersion in the interferometer sample and reference arms was carefully matched. Appropriate thickness glass blanks of fused silica, SFL6, and LakN22 were inserted into the reference arm to balance the dispersion of the achromatic lenses in the imaging probe. Dispersion mismatch was monitored by taking the Fourier transform of the interferometer fringe signal. Figure 2.4A and Figure 2.4B show the interference signal after bandpass filtering and the logarithmic demodulated signal after lowpass filtering. The measured axial resolution was 6.3 μm in air, corresponding to 4.8 μm in tissue. The detected optical spectrum was measured to be 110 nm by Fourier transformation of the interferometric signal. This reduction in bandwidth may be the result of wavelength dependence of the fiber couplers as well as wavelength variations in the sensitivity of the InGaAs photodiodes.

The system sensitivity was measured using the minimum visible intensity of a reflection from a mirror and was 95 dB with an incident power of 20 mW. The theoretical sensitivity for this incident power and detection bandwidth is 103 dB. Parasitic losses in the sample arm optics, fiber couplers, and fiber connectors account for ~4 dB of the reduction in sensitivity. Incomplete noise cancellation from mismatches in the fiber couplers and detectors may account for the additional 4 dB reduction in sensitivity.

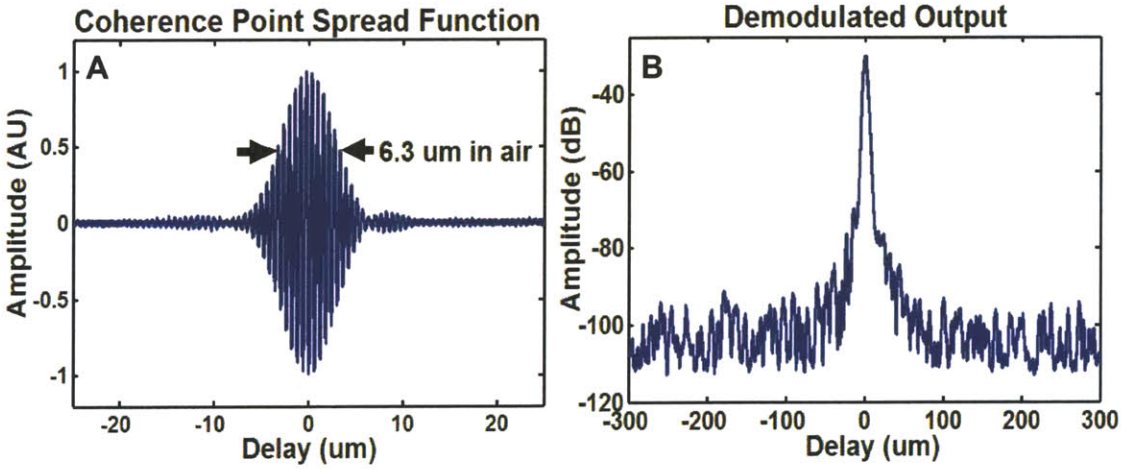

Figure 2.4: A. Point spread function measured using an isolated 3.0 OD attenuated reflection from a mirror. The axial resolution is 6.3 μm in air, corresponding to <5 μm in tissue. B. Logarithmically demodulated signal showing low sidelobes.

Ultrahigh resolution, high-speed, *in vivo* OCT imaging using this source was demonstrated in human skin as well as in the hamster cheek pouch, a well-established model for studies of cancer progression. Imaging was performed using an XY scanning probe. Figure 2.5 shows high-speed, ultrahigh resolution *in vivo* images of human skin. The image had 500 transverse pixels and 1000 axial pixels and covered an area of 2.25 mm by 1.8 mm. Imaging was performed at a rate of 3.2 frames per second. The axial dimension was scaled by 1.38 to account for the approximate index of refraction of skin.[102] Distinct morphological features such as the

keratinized stratum corneum, the junction between the dermis and epithelium, and sweat ducts are clearly visualized in the ultrahigh resolution images.

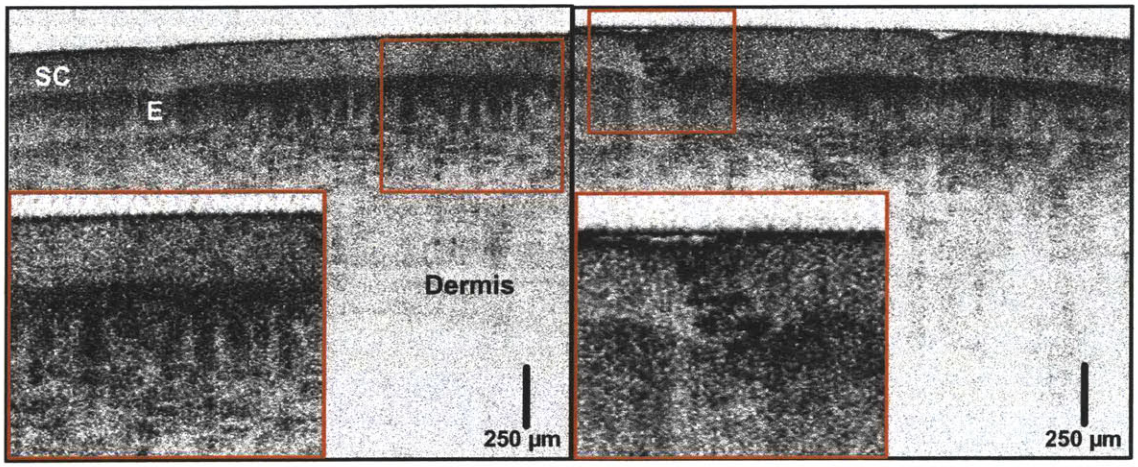

Figure 2.5: *In vivo* high-speed OCT images of human skin. The stratum corneum layer (SC), epithelium (E), dermis, dermal-epidermal junction (arrows, inset left) and a spiraling sweat duct (arrow, inset right) can clearly be seen. Images were acquired at 3.2 frames per second. (~18 µm x 4.8 µm transverse x axial resolution; 500 x 1000 pixels; 2.25 mm x 1.8 mm).

Figure 2.6: High-speed, ultrahigh resolution *in vivo* OCT image of Syrian hamster cheek pouch. The keratinized epithelial layer (e), muscular layers (m), and two prominent vessels (v) are clearly visible. A microscope cover glass (c) was placed over the top of the cheek pouch. (~18 µm x 4.8 µm transverse x axial resolution; 500 x 1000 pixels; 2.4 mm x 1.4 mm).

Figure 2.6 shows an *in vivo* image of hamster cheek pouch. Imaging was performed with the animal under anesthesia and in accordance with approved protocol reviewed by the Massachusetts Institute of Technology Committee on Animal Care (CAC). The ultrahigh resolution images had 500 transverse pixels and 1000 axial pixels and covered an area of 2.4 mm by 1.4 mm. The ultrahigh resolution OCT image exhibits structure associated with the normal hamster cheek pouch. A thin, keratinized layer which is highly backscattering is present near the surface, followed by an epithelial layer (e), muscular (m) layers, and connective tissue. Two

prominent blood vessels (v) are also clearly visible within the muscular layers and connective tissue. Image depths are comparable to those achieved with other 1.3 μm light sources.

To demonstrate the high-speed imaging capability of this ultrahigh resolution OCT system, *in vivo* three-dimensional imaging of human skin and hamster cheek pouch was also performed. High-speed imaging enables volume datasets to be acquired, permitting tracking of morphological features through the imaging volume. Each three-dimensional data set consisted of sequentially acquired transverse OCT images, each containing 500 transverse pixels and 1000 axial pixels. Volume imaging of human skin consisted of 50 transverse images with 15 μm spacing between frames, spanning an imaging volume of 2.25 mm x 0.750 mm x 1.8 mm. Imaging of hamster cheek pouch consisted of 50 transverse images with 20 μm spacing between frames, spanning an imaging volume of 2.4 mm x 1.0 mm x 1.8 mm. The data was acquired at 3.2 frames per second, for a total acquisition time of ~15 seconds for 500 x 50 x 1000 = 2,500,000 data points or voxels. The three-dimensional dataset can be displayed in various orthogonal planes or rendered using image processing and rendering software.

Figure 2.7 shows an example of three-dimensional imaging of the hamster cheek pouch. In Figure 2.7A, the three-dimensional data can be viewed in sequential transverse slices, corresponding to the normal OCT view. This enables features such as the epithelial layer, muscular layers, connective tissue, as well as two large blood vessels to be tracked through successive image planes. In Figure 2.7B, the three-dimensional data is viewed using *en face* slices at different depths, perpendicular to the normal OCT view, corresponding to the view typically provided by confocal microscopy. The *en face* slices enable surface features such as folds in the epithelium to be better visualized than in the transverse slices. Figure 2.8 shows a rendered volume of the hamster cheek pouch constructed from the three-dimensional data set. The rendered tissue volume can be viewed from arbitrary virtual perspectives. Videos showing animations of sequential slices through the imaging volume are available in the supplementary materials.

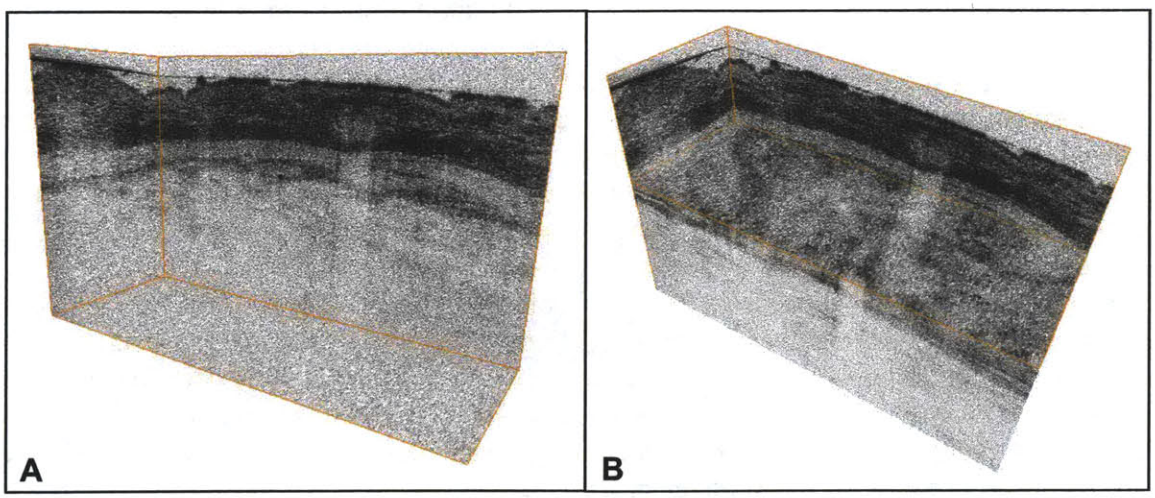

Figure 2.7: Three-dimensional volume imaging using *in vivo* ultrahigh resolution OCT images acquired at 3.2 frames per second. A. Sequential transverse slices of hamster cheek pouch with two large vessels, corresponding to the normal OCT view. B. *En face* slices at different depths, perpendicular to the OCT view, allowing features such as epithelial folds and vessels to be visualized. Movies showing animations of sequential slices are available in the supplemental materials. The rendered volumes cover 2.4 mm x 1.0 mm x 1.8 mm.

Figure 2.8: Rendered volume of hamster cheek pouch constructed from a three-dimensional dataset. The tissue volume can be viewed from arbitrary virtual perspectives. The rendered volume covers 2.4 mm x 1.0 mm by approximately 1.8 mm. A movie showing the rendered volume from arbitrary perspectives is available in the supplemental materials.

Figure 2.9 shows examples of three-dimensional imaging in human skin. In Figure 2.9A, the volume data can be displayed in *en face* slices at different depths through the human fingerpad. Structures such as ridges in the stratum corneum associated with the fingerprint could be clearly

seen. Sweat ducts could also be clearly seen spiraling along the ridges of the fingerpad through the stratum corneum and into the epithelium. Three-dimensional rendering and segmentation can be performed as shown in Figure 2.9B, enabling the density of sweat ducts as well as individual ducts to be assessed (inset). Other structures such as the rete ridges in the junction between the epithelium and dermis can also be visualized. Videos showing animations of sequential slices through the fingerpad and the rendered ducts are available in the supplementary materials.

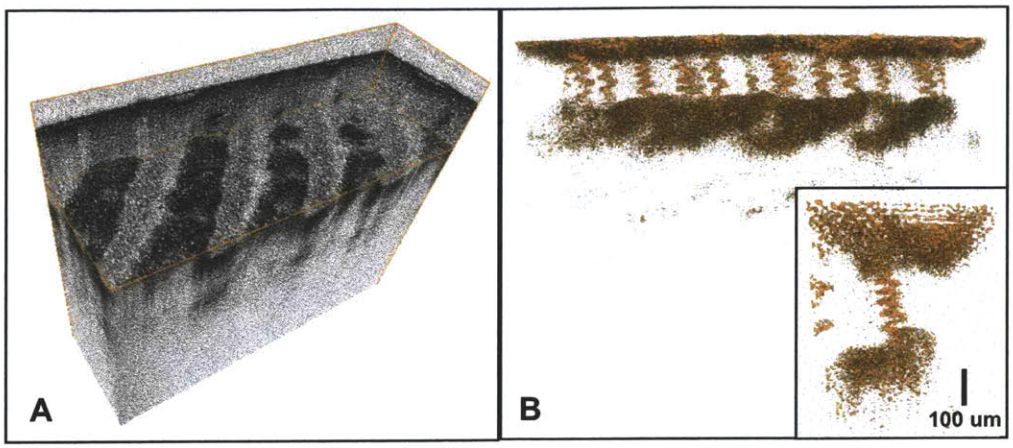

Figure 2.9: A. *En face* slices of human fingerpad created from cross-sectional images. Spiraling sweat ducts could be seen along the fingerpad ridges (2.25 x 0.75 x 1.8 mm) B. 3D rendering and segmentation of sweat ducts. Duct density as well as individual ducts can be assessed. Movies showing virtual *en face* slices and animations are available in the supplemental materials.

CONCLUSION

In conclusion, this chapter demonstrated a new, high performance light source for high-speed, ultrahigh resolution OCT imaging. Bandwidths of 140 nm in the 1300 nm wavelength range are achieved, yielding axial resolutions of < 5 μm in tissue. The axial resolution of < 5 μm is comparable to that achieved using much more complex femtosecond solid state sources such as the Cr:Forsterite laser. Output powers of 330 mW enable high-speed, OCT imaging *in vivo*. Output powers are comparable to or better than those available from femtosecond lasers, and more than one order of magnitude higher than superluminescent diode sources. Since this light source is all-fiber, it requires no alignment and provides completely turnkey operation. The source is extremely compact, measuring only 25 x 25 x 20 cm, and can easily be integrated into portable OCT systems. Excess noise is relatively high, but can be reduced using dual-balanced detection. Further reduction in noise should be possible by reducing parasitic feedback effects in the fiber splices and by techniques such as active seeding of the Raman process. Broader output bandwidths should be achievable using higher pump power Yb-fiber lasers and different fiber geometries. The bandwidth will ultimately be limited by the water absorption of microstructure fibers which reduces the effective interaction length of the Raman scattering. The current cost of the source is still relatively high due to the cost of the microstructure fiber. However, since demand for microstructure fiber is increasing, the price of these fibers is decreasing and can be

expected to approach that of other specialty fibers. The cost of continuous-wave Yb-fiber lasers has also dramatically decreased in recent years. The cost of fiber Raman continuum light sources will therefore be significantly lower than that of bulk solid-state femtosecond laser-based light sources. The high performance and ease of use of the fiber Raman continuum source promises to enable a wide range of new ultrahigh resolution, high-speed, OCT imaging applications.

Chapter 3

Effect of Tissue Preservation on Imaging using Ultrahigh Resolution Optical Coherence Tomography

INTRODUCTION

Optical coherence tomography (OCT) is an emerging imaging modality which can generate micron-resolution, cross-sectional images of tissue microstructure in situ and in real time.[3, 4] Since the first demonstration in 1991, OCT has been investigated for imaging a number of neoplastic pathologies.

Early OCT studies initially focused on *ex vivo* imaging to establish correlations with histopathology and feasibility for future *in vivo* studies. [6-9, 103-109] With the development of fiber optic endoscopes, *in vivo* OCT imaging in animals was demonstrated, [51] and not long afterwards the first *in vivo* endoscopic imaging in humans was performed. [110] However, accurate registration of OCT images with histology is difficult to achieve with *in vivo* imaging. Subsequent studies investigating the effect of OCT imaging parameters on tissue structure identification in the gastrointestinal tract have been performed *ex vivo* partly for this reason. [111] Previous studies in ophthalmology have also investigated the effect of nonlinear shrinkage and sectioning stress during histology preparation on subsequent interpretation of retinal microstructures.[112]

It is generally believed that non-negligible changes in tissue scattering characteristics are visible within a few hours, motivating investigations to be performed as soon as possible after tissue excision. However, the effect of tissue ischemia on optical scattering is still not well understood. Prior studies in animal models have shown negligible changes in tissue reflectance up to 25 minutes after excision during immersion in 0.9% isotonic saline,[113] and fluorescence and diffuse reflectance studies showed preservation of 70-90% of spectroscopic signal intensity up to 1.5 hours after biopsy.[114] In addition, the timecourse of these changes post-excision has not been investigated. Previous studies involving *ex vivo* imaging of tissue specimens have reported imaging times after tissue harvest ranging from 30 minutes[109, 115, 116] to 5 hours.[105-108] Imaging has also been performed on formalin-fixed specimens,[111] previously frozen specimens,[107, 117] and on specimens harvested from cadavers.[6, 105, 106, 108, 118] Isotonic saline has typically been used for specimen irrigation and transport,[8, 9, 67, 107, 109, 115] but buffered saline[6, 105, 106, 108] and Hank's

solution have also been used.[109] Studies comparing protocols for tissue preservation for *ex vivo* imaging have not been reported in the literature.

The objectives of this study were to investigate the effect of formalin fixation on imaging using ultrahigh resolution OCT, and to test the effect of two commonly used laboratory culture media on *ex vivo* preservation of tissue optical scattering characteristics over time. Standard formalin fixation followed by paraffin-embedding leads to shrinkage and processing artifacts which complicate image interpretation. Imaging at sequential timepoints during the fixation process allows one-to-one correlation of tissue structures with histology, enabling accurate interpretation of *in vivo* tissue architectural features. As it is not always possible in human studies to image tissue specimens immediately after excision, the effect of post-excision imaging time on optical scattering characteristics was also investigated. Imaging was performed on the same tissue specimens *in vivo* and up to a maximum time of 10-18 hours after excision, enabling direct comparison of *in vivo* versus *ex vivo* imaging.

This chapter investigates the effect of formalin fixation on imaging contrast using ultrahigh resolution OCT, and describes the effect of two commonly used laboratory media on *ex vivo* preservation of tissue optical contrast. The hamster cheek pouch was chosen for this study because it consists of representative tissue components and is a commonly used system for the study of tumorigenesis. When dosed with carcinogen, histological features in this model have been shown to correspond closely with premalignant and malignant lesions in human oral mucosa.[119] The tissue constituents in the hamster cheek pouch are representative of the composition of human epithelial tissues such as oral mucosa, esophagus, and cervix. There has been recent interest in investigating tumor development in this model using non-invasive optical techniques. Fluorescence spectroscopy has been shown to detect biochemical changes associated with early tumor development in this model.[120, 121] Multiphoton microscopy and optical coherence tomography have also recently demonstrated ability to detect early morphological changes associated with cancer development in the hamster cheek pouch.[122, 123]

In this study, three solutions were tested to assess their affect on tissue optical scattering characteristics. First, 10% neutral-buffered formalin was investigated to determine the effect of the fixation process on imaging using OCT. Formalin, consisting of 4% formaldehyde, is the most common fixative used for routine paraffin-embedded sections. Formaldehyde acts by forming cross-linkages between tissue proteins, fixing cellular constituents in their *in vivo* positions and thus preventing autolytic processes.[124] Although formalin penetrates tissue well, the rate of tissue penetration is relatively slow.[125] The second solution tested was isotonic phosphate-buffered saline (PBS). PBS is a common solution used in many laboratory procedures, often serving as medium for irrigating, transporting and diluting fluid. Isotonic PBS maintains intra- and extra-cellular osmotic balance and a buffering system keeps the medium within the physiological pH range. The third solution tested was Dulbecco's Modified Eagle's Media (DMEM), a commonly used synthetic cell culture media. DMEM includes higher concentrations of amino acids and vitamins than basal salt solutions as well as additional supplementary components so that the medium more closely approximates the protein composition of mammalian cells. The autolysis process begins immediately after tissue harvest. Tissue culture media was expected to slow autolytic processes, slowing changes which may influence tissue contrast. Sera, which contain additional supplements and growth factors and are typically added

to media used for cell culture, were not added to DMEM in this study because the goal was to investigate the performance of individual solutions on preservation of *in vivo* optical scattering characteristics in order to minimize complexity associated with tissue handling protocols.

METHODS

Ultrahigh Resolution OCT System and Imaging Parameters

Ultrahigh resolution OCT imaging was performed using a state-of-the-art broadband Ti:Al_2O_3 laser operating at a center wavelength of 800 nm.[86] Imaging was performed with an axial resolution of 2 μm in free space, corresponding to ~1.5 μm in tissue. To achieve high transverse resolution, an imaging probe consisting of two specially-designed achromatic doublets with 10 mm focal length was used, yielding a transverse resolution of ~5 μm in air. The system sensitivity was measured to be 103 dB with 3 mW of optical power on the sample. The imaging probe was mounted on two precision computer-controlled micrometer stages to control imaging in two lateral dimensions. All images acquired were 1 mm x 1 mm in dimension and consisted of 1000 axial x 1000 transverse pixels. This enabled an imaging sample density of 1 pixel/μm in both axial and transverse dimensions.

Specimen selection and handling

All animal procedures were approved by the Committee on Animal Care (CAC) at the Massachusetts Institute of Technology. The Golden Syrian hamster (*Mesocricetus auratus*) cheek pouch model was chosen for this study because it consists of keratinized squamous epithelium, collagen, skeletal muscle, blood vessels, adipose tissue, sebaceous glands, and other representative tissue constituents.[126] Imaging in an animal model allows *in vivo* and *ex vivo* imaging to be performed on the same tissue specimen, enabling direct investigation of *ex vivo* handing protocol on image characteristics. In addition, the hamster cheek pouch carcinogenesis sequence closely resembles the events involved in the development of premalignant and malignant human oral cancers,[119] and is thus a relevant model for investigations of tumorigenesis using optical techniques. Hamsters were anesthetized using intraperitoneal pentobarbital sodium 50 mg/kg with diazepam 10 mg/kg and kept warm using an isothermal heating pad (Braintree Scientific, Braintree, MA) during the *in vivo* portion if the imaging procedures.

Prior to imaging, the anesthetized hamster cheek pouch was everted using a specially-designed and fabricated clamp which was fastened rigidly to the optical table surface. Figure 3.1 shows a photograph of the *in vivo* and *ex vivo* imaging set-up. The clamping device consisted of a top aluminum piece with a window which enabled imaging and irrigation of the tissue surface and a bottom plastic piece which enabled the periphery of the cheek pouch specimen to be pinned post-mortem. *In vivo* imaging was initially performed. The animal was subsequently euthanized and the zero time point was recorded at the time of cessation of respiration. The periphery of the cheek pouch was then pinned to the bottom piece of the clamp, enabling the cheek pouch to be excised from the animal with minimal disturbance to the *in vivo* imaging plane. Specimens of approximately 1 cm x 1 cm size were used in this study to minimize the effect of changes in optical scattering induced by loss of local supporting tissue structure. A custom-designed and fabricated containment well was subsequently fixed around the clamp and the specimen was

immersed in 10% neutral-buffered formalin (Fisher Scientific Co., Agawam, MA), isotonic phosphate-buffered saline (OmniPur, EMD Chemicals Inc, Gibbstown, NJ), or Dulbecco's Modified Eagle's Media (Gibco/Invitrogen, Carlsbad, CA). All preservation solutions were refreshed every 15-20 minutes to maintain solution tonicity. Imaging was performed at room temperature (21-23 deg C) to approximate the conditions present in most laboratory settings. Imaging using PBS solution was additionally performed at body temperature (37 deg C using an isothermal heating pad) and using an ice bath (solution temperature 8 deg C) to investigate the temperature dependence of tissue preservation over time.

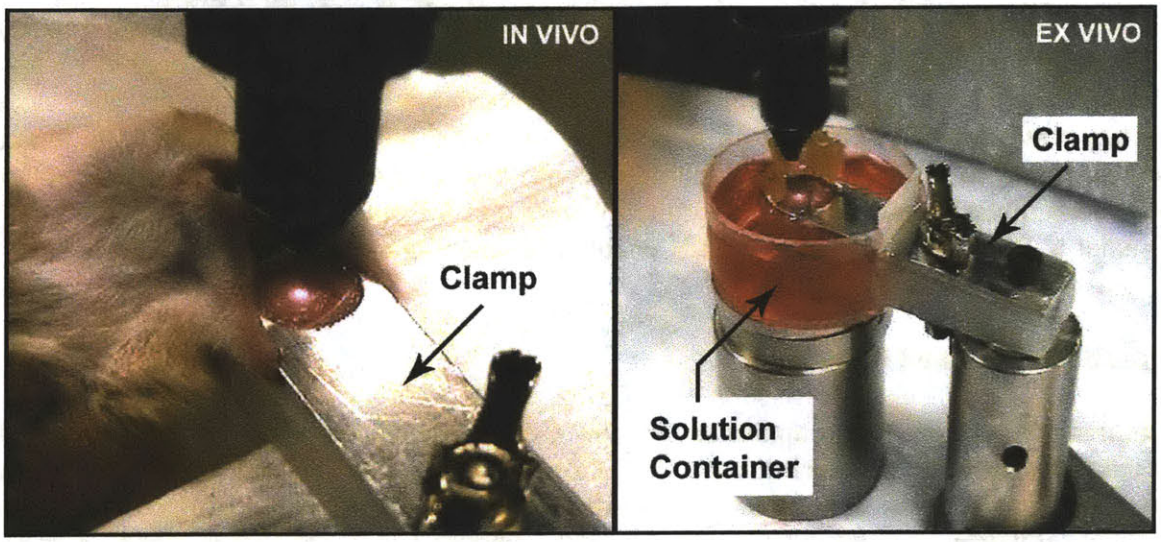

Figure 3.1: Photograph of the *in vivo* and *ex vivo* imaging set-up. The custom-built clamping device consisted of a top aluminum piece with a window which enabled *in vivo* imaging and a bottom plastic piece which allowed the periphery of the cheek pouch specimen to be pinned post-mortem for accurate registration during the imaging timecourse. A custom-designed and fabricated container fixed around the specimen enabled complete immersion of the excised specimen in preservation solution.

Imaging protocol

Separate animals were used for each solution and temperature investigated in this study in order to enable registered imaging *in vivo* and *ex vivo* over the entire time course. Imaging on an additional animal was performed for DMEM solution preservation in order to verify consistency of the observed results. For each solution, imaging was performed *in vivo,* at 15 min, 30 min, 1 hr, 1.5 hours, 2 hours, 2.5 hours, 3 hours, 3.5 hours, 4 hours, 5 hours, 6 hours, 7 hours, 8 hours, and 10 hours. Imaging formalin solution was additionally performed at 12, 14, 16, and 18 hours in order to insure complete fixation. For each imaging time point, eleven images were taken. The first ten images were each sequentially offset in the sagittal direction by 100 μm, enabling imaging over a tissue volume of 1 mm x 1 mm x 1 mm in dimension. This allowed representative images over a cross-section of architectural morphology of the hamster cheek pouch to be acquired and also to facilitated subsequent registration with histology. The final image was taken in the same location as the first image to verify the accuracy of the registration

protocol and to determine if contrast had changed over the course of the imaging procedure itself. Each set of 11 images was acquired in approximately 10 minutes. After completion of the imaging time course, the OCT imaging plane was marked with two microinjections of ink, placed in 10% neutral-buffered formalin, routinely processed and paraffin embedded. Multiple 5 μm thick tissue sections were obtained from the OCT imaging planes and stained. Standard Hematoxylin-Eosin as well as Masson's Trichrome stains were used to visualize the imaged tissues for light microscopy. OCT images and corresponding histology sections were compared. Minor discrepancies between histology and OCT images can be attributed to residual tissue fixation, processing and sectioning artifacts.

RESULTS

OCT images and histology photomicrographs at 100x and 200x magnification are shown scaled with the same magnification as the OCT image. All OCT images were scaled in the axial direction by 1.38x to account for the approximate index of refraction of tissue.[102]

10% Neutral-buffered formalin

A magnified view of the cheek pouch *in vivo* and at 18 hours with Hematoxylin and Eosin and Masson's trichrome histology is shown in Figure 3.2. One-to-one correlation clearly identified the keratinized squamous epithelium, lamina propria, skeletal muscle bundles, blood vessels, adipocytes, and collagen-rich connective tissue. *In vivo*, the epithelium appeared uniformly scattering. Muscle bundles appeared low scattering relative to highly scattering intervening connective tissue. Collagen layers appeared relatively high scattering. Adipose tissue appeared low scattering, with clearly septated borders between individual adipocytes. Intravascular leukocytes in the blood vessel were seen in the OCT image as focal spots of increased scattering.

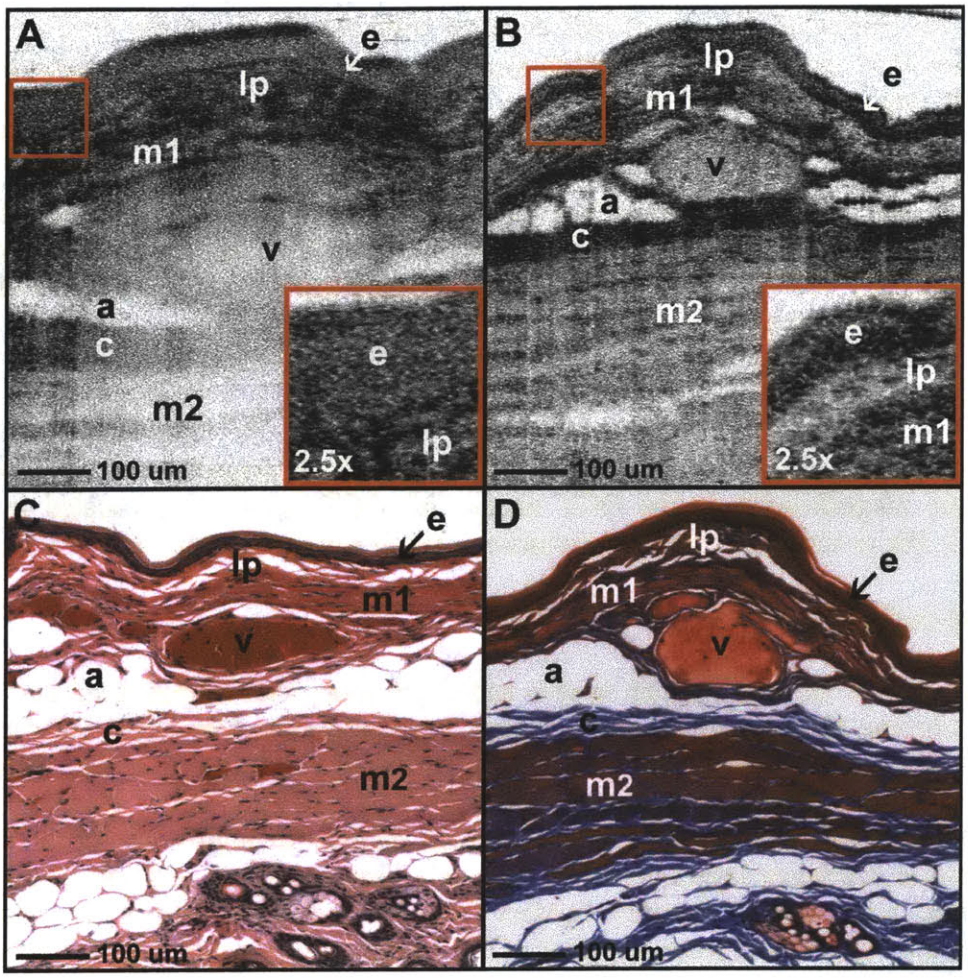

Figure 3.2: Magnified view of the cheek pouch *in vivo* (A) and at 18 hours (B) with Hematoxylin and Eosin (C) and Masson's trichrome (D) histology. One-to-one correlation clearly identified structures corresponding to the epithelium (e), lamina propria (lp), superficial muscle layer (m1), blood vessel (v), adipocytes (a), collagen-rich connective tissue (c), and deep muscle layer (m2). Leukocytes appear in the OCT image as focal spots of increased scattering. (Wavelength 800 nm, Resolution 1.5 μm axial x 5 μm transverse)

Figure 3.3 illustrates a sequence of representative OCT images acquired *in vivo* and over 16 hours in 10% neutral-buffered formalin. During the fixation process, change in contrast was visible within the squamous epithelial layer itself, with an increase in scattering signal in the lower 1/3-1/2 of the epithelium nearer the basal boundary (Figure 2, inset). Decrease in scattering within the lamina propria was apparent, whereas scattering within muscle bundles appeared to increase. Overall contrast between tissue architectural features appeared to increase during fixation over 18 hours and corresponded in time with significantly noticeable tissue shrinkage. Shrinkage was visible in the deeper muscle bundle and connective tissue layers by 1 hour after immersion in formalin and increase in scattering was significantly noticeable by 2 hours. The squamous epithelial layer, loose connective tissue, and muscle layers exhibited approximately 50% overall shrinkage. Little or no shrinkage was observed in adipose tissue, however, boundaries between adipocytes sharpened over the 18 hour time course. Shrinkage and

distortion of the surrounding connective tissue is most likely responsible for visible architectural changes in the adipose tissue layers. A large blood vessel visible at the center of the image also exhibited shadowing *in vivo* and over the first 2 hours which disappeared completely by 4 hours. A representative video showing the time course of formalin fixation is available in supplemental material. The video shows sequential ultrahigh resolution OCT images acquired at each of the imaging time points from *in vivo* to 18 hours.

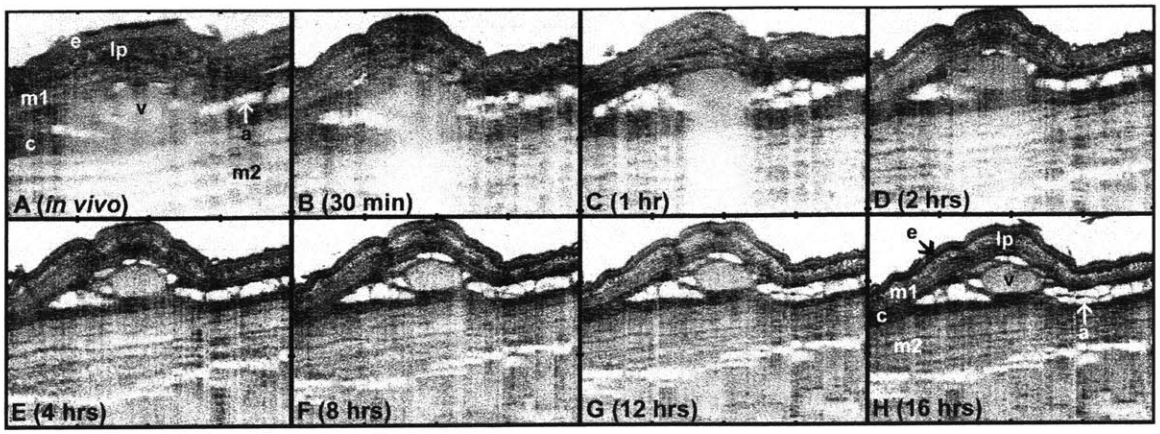

Figure 3.3: Sequence of representative OCT images acquired *in vivo* and over 16 hours in 10% neutral-buffered formalin: A, *In vivo*; B, 30 minutes; C, 1 hour; D, 2 hours; E, 4 hours; F, 8 hours; G, 12 hours; H, 16 hours. Shrinkage was visible in all tissue layers. e: epithelium; lp: lamina propria; m1, m2: muscle layers; c: connective tissue; a: adipose tissue; v: blood vessel. Tick marks represent 250 μm. (Wavelength 800 nm, Resolution 1.5 μm axial x 5 μm transverse)

Isotonic phosphate-buffered saline (PBS)

Figure 3.4 illustrates OCT images acquired *in vivo* and over 6 hours after excision and immersion in isotonic phosphate-buffered saline at room temperature. Appearance of tissue architectural features *in vivo* was consistent with the *in vivo* appearance of the formalin timecourse specimen discussed previously. However, post-excision optical scattering intensity appeared to decrease monotonically after immersion in PBS. Decrease in overall signal intensity was visible in the image within 30 minutes after tissue excision and was significant by 2 hours. Loss of scattering signal appeared first in the deeper muscle and connective tissue layer (m2) and was consistently noticeable within 3-4 hours. Swelling in the superficial muscle (m1) and thick connective tissue layer (c) was visible. Settling of blood vessel contents was also visible, as was some collapse of vessel walls. Significant overall changes in the epithelial layer were not observed during immersion in isotonic PBS at room temperature over the 10 hour timecourse, although shrinkage is visible in the histology due to formalin fixation.

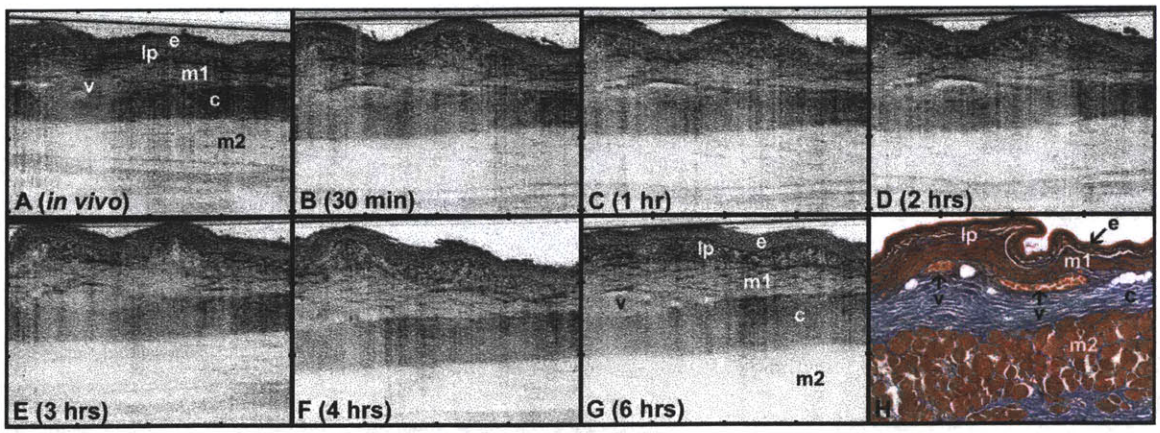

Figure 3.4: Sequence of representative OCT images acquired *in vivo* and over 6 hours in isotonic phosphate-buffered saline solution at room temperature: A, *In vivo*; B, 30 minutes; C, 1 hour; D, 2 hours; E, 3 hours; F, 4 hours; G, 6 hours; H, Masson's trichrome. Loss of scattering signal was significant within 2 hours and appeared to decrease monotonically after tissue excision. Swelling in the muscle (m1 and m2) and thick connective tissue layer (c) was visible. e: epithelium; lp: lamina propria; v: blood vessel. Tick marks represent 250 μm. (Wavelength 800 nm, Resolution 1.5 μm axial x 5 μm transverse)

Figure 3.5 illustrates images acquired *in vivo* and at 6 hours post-excision obtained after immersion in PBS at body temperature, room temperature, and under hypothermic conditions. Each of the separate tissue specimens exhibited loss of scattering signal in the deeper muscle and connective tissue layer (m2) by 3-4 hours which were significantly noticeable by 6 hours. Tissue maintained at body temperature in PBS saline seemed to preserve higher signal intensity in the deeper muscle layers relative to PBS at room temperature and using an ice bath, although differences were not significant. Some swelling of the superficial muscle layer (m1) and thick connective tissue layer (c) was observed at all temperatures.

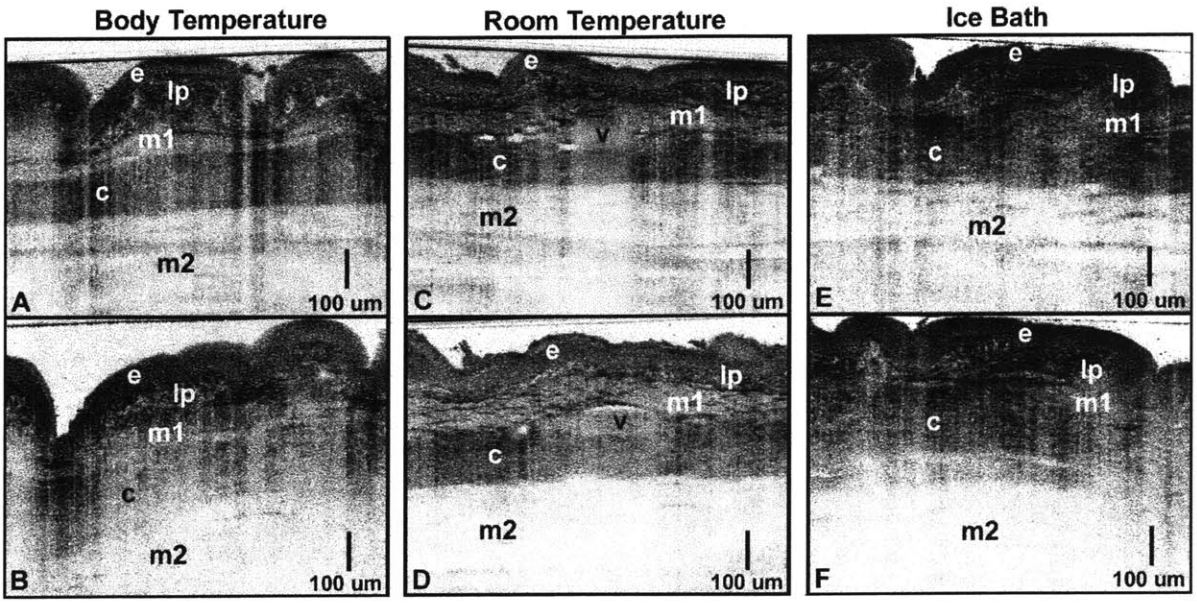

Figure 3.5: Images acquired *in vivo* (A,C,E) and at 6 hours (B,D,F) post-excision obtained after immersion in PBS at body temperature (top), room temperature (middle), and under hypothermic conditions (bottom). Tissue maintained at body temperature in PBS saline seemed to preserve higher scattering signal intensity in the deeper tissue layers relative to PBS at room temperature and using an ice bath, although differences were not significant. e: epithelium; lp: lamina propria; m1, m2: muscle layers; c: connective tissue; v: blood vessel. (Wavelength 800 nm, Resolution 1.5 µm axial x 5 µm transverse)

Dulbecco's Modified Eagle's Media (DMEM)

Figure 3.6 illustrates OCT images acquired *in vivo* and over 10 hours after excision and immersion in DMEM at room temperature. Visualization of tissue architectural morphology *in vivo* was also consistent with *in vivo* imaging for both formalin and PBS specimens discussed previously. Scattering signal intensity was maintained close to *in vivo* conditions during immersion in DMEM up to 4-6 hours after excision. Slight decrease of scattering signal visible at the 6-8 hour time point also appeared first in the deep muscle and connective tissue layer (m2), but was not significantly noticeable until 8-10 hours after tissue excision. No significant overall swelling in any of the tissue layers was observed during immersion in DMEM at room temperature. Significant changes in the epithelial layer were not observed during immersion in DMEM at room temperature over the 10 hour timecourse, although shrinkage is again visible in the histology due to formalin fixation. Preservation in DMEM maintained the most similar image appearance and overall signal intensity compared with *in vivo* imaging.

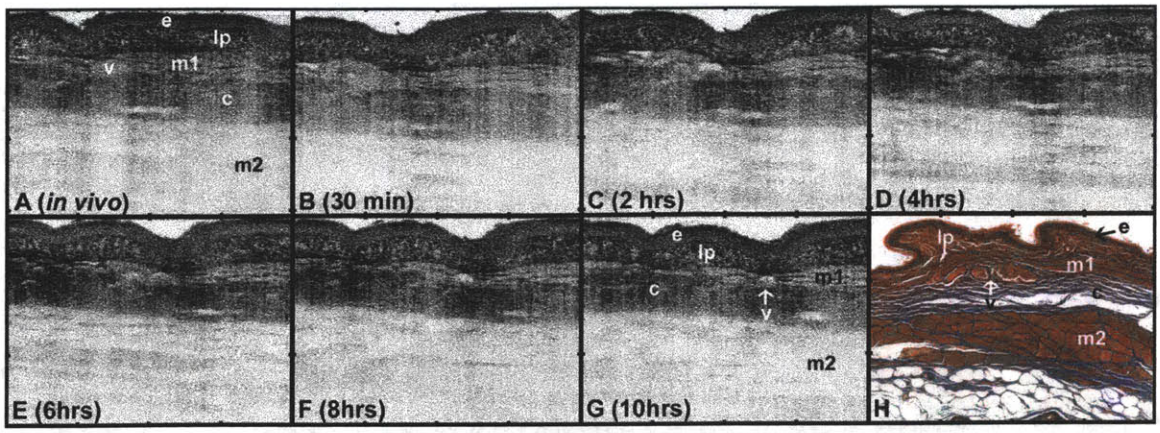

Figure 3.6: Sequence of representative OCT images acquired *in vivo* and over 10 hours in DMEM solution at room temperature: A, *In vivo*; B, 30 minutes; C, 2 hours; D, 4 hours; E, 6 hours; F, 8 hours; G, 10 hours; H, Masson's trichrome. Optical scattering characteristics were maintained close to *in vivo* conditions up to 4-6 hours after excision and remained similar over the entire timecourse. e: epithelium; lp: lamina propria; m1, m2: muscle layers; c: connective tissue; v: blood vessel. Tick marks represent 250 μm. (Wavelength 800 nm, Resolution 1.5 μm axial x 5 μm transverse)

Figures 3.7 and 3.8 show a comparison of representative axial scan profiles for DMEM and PBS *in vivo*, at 4 hours, and at 10 hours. Scan profiles were averaged over 10 consecutive axial scans to minimize fluctuations due to noise. Axial scan profiles for PBS show loss of signal intensity between layers over the time course and decrease in overall reflectivity, particularly in the deep muscle and connective tissue layers. Overall tissue scattering signal was best preserved similar to *in vivo* conditions using DMEM.

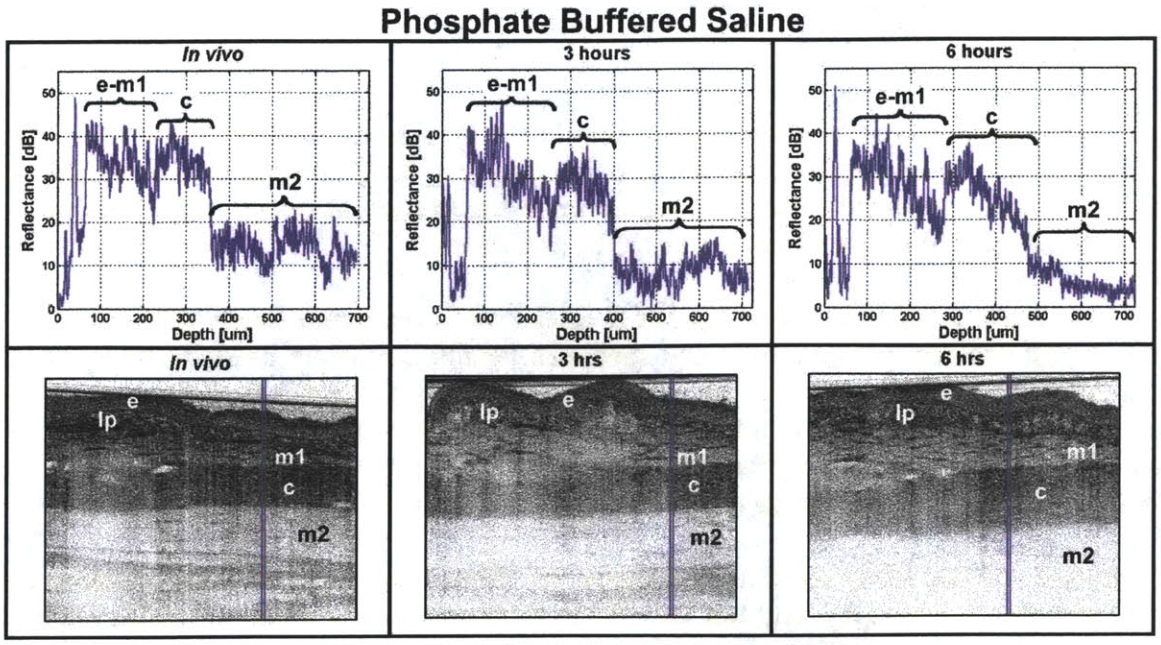

Figure 3.7: Measured reflectance profiles as a function of depth for PBS *in vivo*, at 4 hours, and at 10 hours. Profiles were averaged over ten consecutive axial scans to reduce noise fluctuations. Scan profiles for PBS show loss of contrast between layers over the timecourse and decrease in overall signal intensity, particularly in the deep muscle and connective tissue layers. e: epithelium; lp: lamina propria; m1, m2: muscle layers; c: connective tissue.

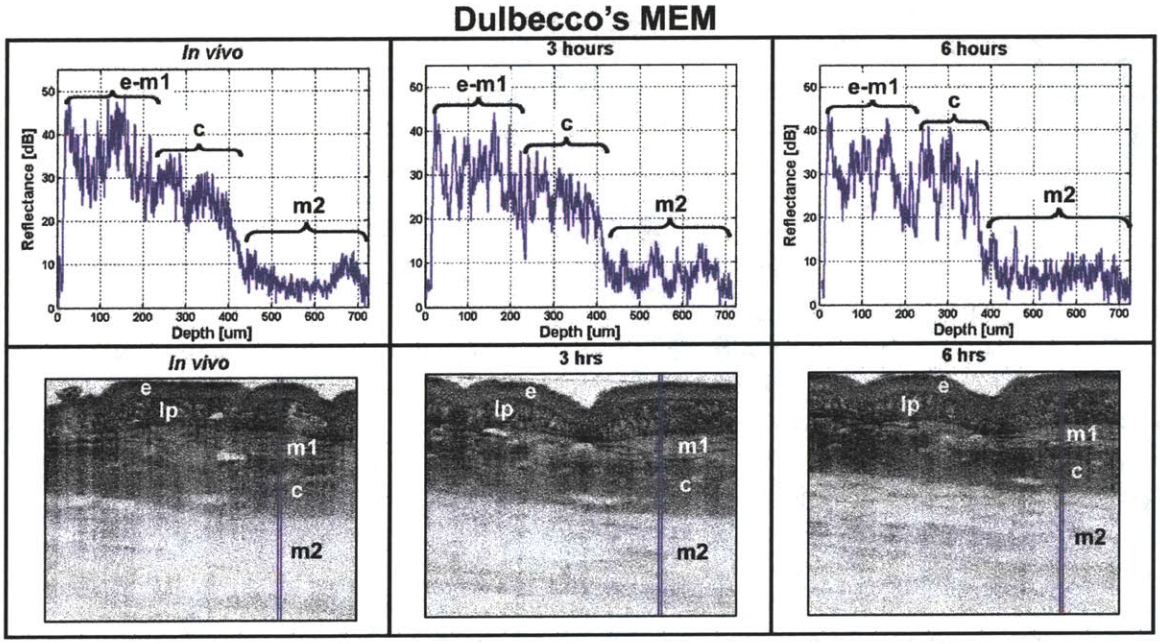

Figure 3.8: Measured reflectance profiles as a function of depth for DMEM *in vivo*, at 4 hours, and at 10 hours. Profiles were averaged over ten consecutive axial scans to reduce noise fluctuations. Overall contrast and scattering signal intensity for DMEM was preserved similar to *in vivo* conditions. e: epithelium; lp: lamina propria; m1, m2: muscle layers; c: connective tissue.

DISCUSSION

Ex vivo investigations are often a necessary step in the process of validating new technologies and devices for clinical applications. *Ex vivo* imaging has the advantage of allowing careful control of imaging parameters and enabling accurate registration of images with histology and allowing feasibility for future *in vivo* studies to be established.

As it is not always possible in human studies to image specimens immediately after excision, the impact of post-excision imaging time and specimen handling protocol needs to be assessed in order to minimize deviation of tissue *ex vivo* optical scattering properties from those observed *in vivo*. Effects of ischemia, such as cell lysis, alter tissue microstructure and therefore could affect optical scattering and imaging contrast. In addition, standard post-excision fixation and paraffin-embedding may result in processing artifacts which can complicate image interpretation.

The objectives of this study were to investigate the effect formalin fixation on imaging using optical coherence tomography, and test the effectiveness of two commonly available laboratory solutions for *ex vivo* preservation of optical scattering over time. Accurate registration of images with histology is particularly difficult to achieve with *in vivo* imaging. Prior studies have relied on animal models using architectural landmarks to interpret tissue structures.[127] Imaging through the fixation process minimizes artifacts introduced by fixation and allows one-to-one correlation of tissue structures with histology, enabling direct interpretation of *in vivo* tissue architectural features.

In this study, the formalin fixation process was seen to lead to changes in scattering and tissue architectural distortion due to shrinkage of epithelial, muscle, and connective tissue layers. This is consistent with results reported for human colorectal resection specimens.[128] Formalin solution is hyperosmotic relative to tissue, therefore shrinkage and scattering changes visible in OCT images may be due to tissue dehydration. Recent studies investigating the effect of hyperosmotic agents have shown that local dehydration may contribute to increased scattering due to greater packing of inter- and intracellular tissue components which contribute to scattering.[113, 115, 129] In addition, the extensive cross-linking of tissue proteins by formalin changes the tissue microstructural features and may also result in changes in tissue optical scattering properties. Changes in scattering during fixation therefore likely results from a combination of alterations in tissue structural properties due to the fixation process and overall tissue dehydration. Although significant distortion was evident during the fixation process, comparison of OCT images of fixed specimens with histology showed that little cumulative structural artifact was introduced during subsequent processing and sectioning.

Tissue preservation in PBS solutions resulted in gradual loss of tissue scattering intensity over time, with some appearance of swelling in the superficial muscle and thick connective tissue layer. Although significant changes in optical scattering characteristics were initially expected within 30 minutes, pronounced changes in PBS were not evident until 2 hours after tissue excision. Loss of scattering signal was most evident in the deep muscle and connective tissue layer. In contrast, preservation in DMEM solution yielded only slight loss of overall scattering signal over the entire time course and little tissue shrinkage or swelling. For both solutions, little

overall change was visible in the keratinized squamous epithelial layer over the entire timecourse. These results are consistent with examination of histology specimens from PBS and DMEM solutions. Histology from PBS solutions showed evidence of mild to moderate edema of the underlying connective tissue stroma which was not evident in histology from DMEM solution. It is therefore possible that tissue edema is the dominant effect resulting in decreased optical scattering. The osmolarity of PBS (~308 mOsm) is somewhat lower than that of DMEM (~366 mOsm), therefore hydration and swelling is more likely during immersion in PBS solution. No post-mortem autolysis was observed in any of the specimens, although evidence of subtle cellular changes in the epithelium, such as mild to moderate intracellular edema and swollen nuclei with open chromatin, was present which could reflect the effect of the preservation solutions.

Tissue preserved at body temperature in PBS saline seemed to maintain slightly higher signal intensity in the deep muscle and connective tissue layers relative to PBS at room temperature and using an ice bath, although differences were not significant. *In vivo* tissue scattering characteristics were expected to be best preserved using an ice bath because cryopreservation is known to slow metabolic processes which result in accumulation of metabolic wastes and hasten tissue autolysis. Lack of a significant effect of temperature on optical scattering over time suggests that inherent cellular metabolic processes did not significantly contribute to visible architectural changes within the investigated 10 timecourse. This is consistent with histology from the specimens, which showed no significant differences between tissue specimens maintained at different temperatures. It is also possible that changes in tissue scattering characteristics were not dramatic post-excision because the hamster cheek pouch is relatively robust and less sensitive to autolytic processes. Tissues with more fragile morphology, such as gastric cardia or colonic mucosa, may experience faster post-mortem tissue degradation and be more sensitive to *ex vivo* handling protocol.

The relative scattering intensity of tissue layers was consistent for all solutions both *in vivo* and *ex vivo* over the imaging timecourse for both PBS and DMEM solutions. The squamous epithelium was observed to be uniform and relatively low scattering compared to the underlying lamina propria, and collagen and loose connective tissues were more highly scattering than the muscle bundles. These observations are similar to results reported *in vivo* and *ex vivo* for human esophagus, which consists of a uniform and lower scattering non-keratinized squamous epithelium, a lower scattering muscularis layer, and higher scattering collagen-rich lamina propria and submucosa.[67, 71, 111] Discrepancy between *in vivo* and *ex vivo* layer thicknesses have been observed which were attributed to specimen stretching and pinning artifacts, but may also have included shrinkage due to fixation.[111]

In this study, the focus zone of the image was held consistently 200-250 um below the surface of the tissue. This enabled comparison between images, but depth of field limitations may lead to different appearances of layers with the same tissue constituents. For example, the connective tissue of the lamina propria in the hamster cheek pouch appears with noticeable fine structure, while the thick connective tissue layer deeper in the tissue appears as a more uniformly scattering band. This may be partially due to different tissue morphology and composition. It is likely that focus tracking methods[86, 130] would yield a more consistent appearance of tissue layers in OCT images.

CONCLUSION

Ultrahigh resolution OCT consistently identified the normal keratinized squamous epithelial layer, lamina propria, collagen and muscle bundles, blood vessels, and adipose tissue *in vivo* and *ex vivo*. Formalin fixation can result in significant shrinkage of all tissue layers, resulting in tissue architectural distortion. Imaging through the fixation process allowed one-to-one correlation of hamster cheek pouch structures with histology, enabling accurate interpretation of *in vivo* tissue architectural features. Changes in optical scattering were significant within the first 2 hours post-excision after preservation with isotonic PBS. DMEM best preserved *in vivo* tissue scattering characteristics over the 10 hour imaging time course. While neoplastic lesions were not evaluated in this study, it is expected that similar benefits of imaging using DMEM or other tissue culture media would apply. Preservation at body temperature using PBS seemed slightly better than either room temperature or cold preservation, although differences were not significant. These results suggest that a tissue culture environment is preferable for preparation of recently excised tissue specimens for optical imaging. These results can also be used as a baseline to aid interpretation of tumor progression studies in the hamster cheek pouch model using optical methods.

Chapter 4

Ultrahigh Resolution Imaging of the Thyroid Gland using Optical Coherence Tomography

INTRODUCTION

Current technologies available for imaging the thyroid gland include scintigraphy, ultrasonography, computerized tomography (CT) and magnetic resonance imaging (MRI). Nuclear scintigraphy, employing radioisotopes, provides mainly functional information about the thyroid gland. The other non-isotopic, cross-sectional imaging techniques are better at providing adjunctive anatomic information. These imaging methods, however, only have limited utility in the evaluation of the thyroid gland. This is because none of these modalities have proven useful in differentiating between benign and malignant thyroid nodules that require surgical excision.[131-133]

An imaging modality capable of imaging the architectural morphology of the thyroid gland with high-resolution on the micron scale could considerably improve the evaluation and management of patients with thyroid abnormalities, as well as reduce the number of patients requiring hazardous surgical exploration. Typical clinical ultrasound systems using sound wave frequencies in the ten megahertz (10 MHz) range can yield spatial resolutions as fine as 150 μm. Even high-frequency ultrasound (30 MHz) devices, which have a maximal resolution of 110 μm, are insufficient to identify epithelial or other microstructure.[134] In contrast, optical coherence tomography (OCT), an emerging technology for *in vivo* high-resolution biomedical imaging, can achieve resolutions in the cellular and even subcellular range (1 - 15 μm).[3, 4, 86, 135-137]

The chapter explores the capability of OCT for imaging the human thyroid gland. Thyroid glands containing normal and pathologic tissue were scanned *ex vivo* at a micron-scale resolution, higher than has been accomplished by any available clinical imaging technology. OCT images obtained were correlated with histopathology from corresponding areas to confirm tissue identity.

METHODS

Ultrahigh Resolution OCT Systems and Imaging Parameters

In this study, OCT imaging was performed using a portable, ultrahigh-resolution imaging system and a surgical imaging probe. Ultrahigh resolution OCT imaging was performed with 4.5 μm axial resolution in tissue using a compact femtosecond Cr:Forsterite laser light source.[94] This source operates at a center wavelength of 1260 nm with a 180 nm bandwidth. The 1260 nm wavelength used is close to a minimum in tissue absorption and scattering, thus allowing imaging to be performed up to 2-3 mm depths. The transverse spot size was set to ~11 μm full width half maximum (FWHM), a factor of 1.5-2x finer than standard OCT systems. The depth of field was calculated to be ~400 μm. Imaging was performed using an imaging probe (~1 cm x 15 cm diameter x length) with a Hopkins lens relay system and beam scanning using galvanometer mirrors, enabling real time visualization and adjustment of the OCT imaging plane.

Preliminary studies were also performed using a portable ultrahigh resolution OCT system with 3.5 μm axial resolution in tissue. This OCT system used a femtosecond Nd:Glass laser light source at a center wavelength of 1090 nm with ~150 nm bandwidth.[96] This laser is commercially available (High Q Laser Productions, Hohenems, Austria) and is compact, robust, and turnkey, making it suitable for future clinical studies. Although shorter wavelengths are attenuated more rapidly by tissue scattering, they enable finer axial resolutions for a given bandwidth as well as smaller spot sizes. The transverse spot size for this system was set to be ~6 μm (FWHM) to examine the effects of improved transverse resolution on imaging the thyroid gland. The depth of field was calculated to be ~140 μm. OCT imaging was performed for this system using post objective scanning in order to avoid aberrations and preserve the small spot size.

Three-dimensional OCT imaging was also performed at 1.1 μm wavelengths. Three-dimensional data sets consisting of 200 to 350 individual OCT images spaced by 3 μm apart were generated by raster scanning the beam. Each OCT image in the raster scan consisted of 600-1800 transverse pixels over 1-2 mm. This resulted in an axial scan spacing of 0.6-3 μm by 3 μm. The 3D OCT data was processed and visualized using MRI software for 3D visualization and volume modeling (Amira, Mercury Computer Systems, Berlin).

Tissue Specimens

Studies were performed on post-mortem and freshly excised surgical thyroid specimens that were received in the Beth Israel Deaconess Medical Center pathology laboratory. Three adult thyroid glands were removed at autopsy and imaged within two hours of excision. Two post-mortem thyroid glands were entirely normal and one gland had an incidental papillary carcinoma. Fifteen thyroid gland specimens surgically excised from adult patients (median age 50 years; 13 female and 2 male) were imaged. Seven cases of multinodular goiter were imaged. These goiters were comprised of multiple thyroid nodules ranging in size from 0.3 cm to 3.5 cm, and were admixed with areas of cyst formation, hemorrhage, scarring and dystrophic calcification. Three other specimens with benign solitary nodules measuring up to 1.9 cm in

diameter were evaluated. Three adenomas, one (1.7 cm) with a predominant microfollicular growth pattern and two (1.5 cm and 3.1 cm) with Hürthle cell changes, were imaged. Two surgical specimens containing papillary carcinoma (both follicular variants), measuring up to 2.2 cm were also imaged. Lymphocytic thyroiditis was noted in two thyroid glands. Preliminary studies at were also performed at 1.1 μm wavelengths on five additional fresh surgical thyroid specimens with goiter, microfollicular adenoma, Hürthle cell changes, and papillary carcinoma. Grossly normal and scarred areas as well as nodular and cystic lesions were imaged.

Registration

Since the OCT source light was in the near infrared range and invisible to the naked eye, tissue registration was performed with a visible green light guiding beam. When necessary, irrigation of specimens (isotonic saline or RPMI 1640) was used to prevent dehydration during imaging. Specimens were marked with India ink to designate the plane of OCT imaging. The samples then underwent routine histologic processing. Tissue sections were placed in 10% formalin, routinely processed and paraffin embedded. Multiple tissue sections of 5 μm thickness were obtained and stained with Hematoxylin & Eosin. Samples were sectioned in the same plane as the scanning plane. Digital two-dimensional OCT images and histology sections corresponding to the imaged areas were compared to identify the sources of tissue contrast in the OCT images. Minor observed discrepancies between histology and OCT imaging were attributed due to tissue fixation, processing and sectioning artifacts.

RESULTS

Histology at 40x and 100x magnification are shown with corresponding size scale bars. All OCT images correlated well with histopathology. Ultrahigh resolution OCT imaging results at 1.3 μm wavelengths with 4.5 μm axial resolution and ~11 μm spot size are presented first.

Normal thyroid microstructure was clearly visualized using OCT. Individual follicles with lumens containing colloid could be identified (Figure 4.1). The smallest follicle visible measured 15 μm in greatest dimension. In normal thyroid glands the follicles were found to be round to oval in shape, with only occasional focal irregularities noted. Colloid appeared low scattering, and occasional follicles contained colloid with focal regions of high scattering. Normal follicular epithelium appeared as a thin, highly scattering, dark layer lining larger follicles and as a slightly thicker, dark rim around smaller follicles.

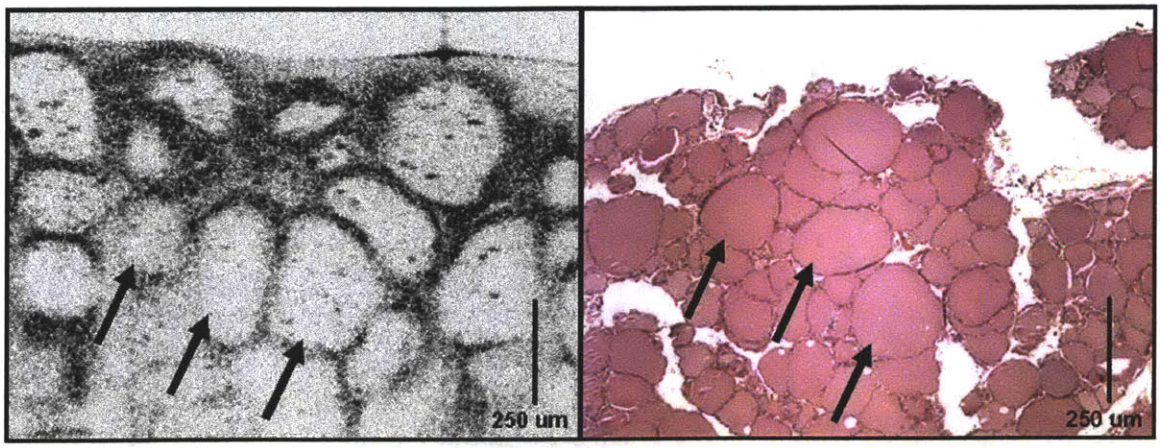

Figure 4.1: Left, Normal thyroid tissue imaged *ex vivo* showing multiple colloid-filled follicles. Right, Histology, Hematoxylin and Eosin 40x. (Wavelength 1.26 μm, Resolution 4.5 μm axial x 11 μm transverse)

Focal benign papillae and smaller follicles (Sanderson's polsters) were found protruding into the lumen of some follicles (Figure 4.2). The normal intervening connective tissue stroma was homogeneous and contained identifiable blood vessels. Areas of recent hemorrhage were noted to be highly backscattering. A dense outer capsule of the normal thyroid gland, measuring up to 150 μm in thickness, was imaged without difficulty and found to include focal clear adipose tissue.

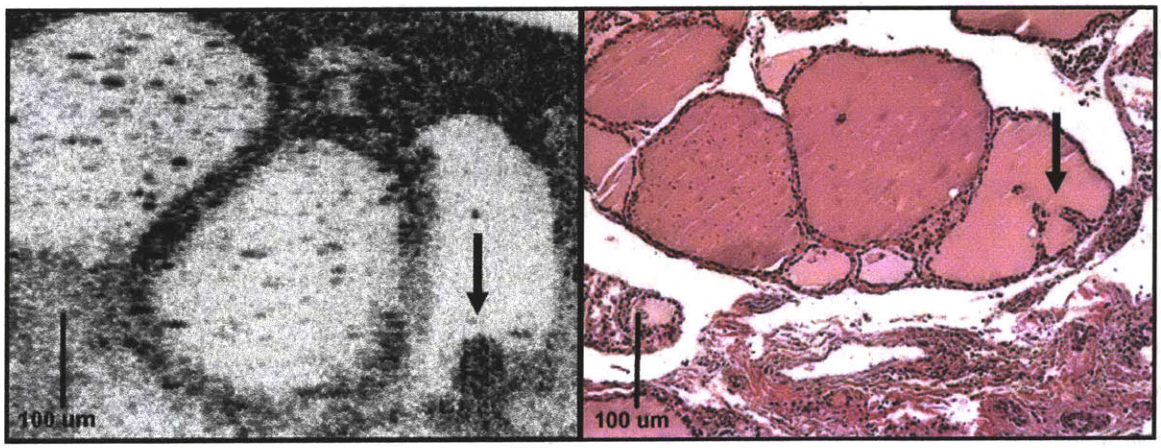

Figure 4.2: Left, Thyroid follicles showing a small intraluminal Sanderson's polster (arrow). Right, Histology, Hematoxylin and Eosin 100x. (Wavelength 1.26 μm, Resolution 4.5 μm axial x 11 μm transverse)

In all cases of multinodular goiter, OCT delineated multiple nodules comprised of mixed macro- and micro-follicles lined by a flattened epithelium. Incomplete fibrous septae demarcating many of these nodules were evident (Figure 4.3).

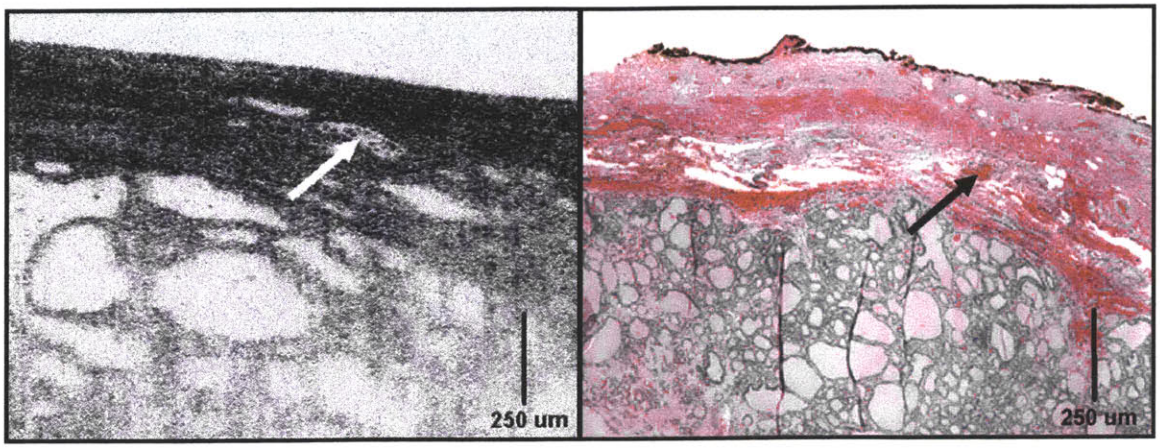

Figure 4.3: Left, Fibrous capsule containing blood-filled vessels (arrow) seen demarcating a mixed macro- and microfollicular thyroid nodule within a multinodular goiter. Right, Histology, Hematoxylin and Eosin 40x. (Wavelength 1.26 µm, Resolution 4.5 µm axial x 11 µm transverse)

Large cysts were readily identified (Figure 4.4).

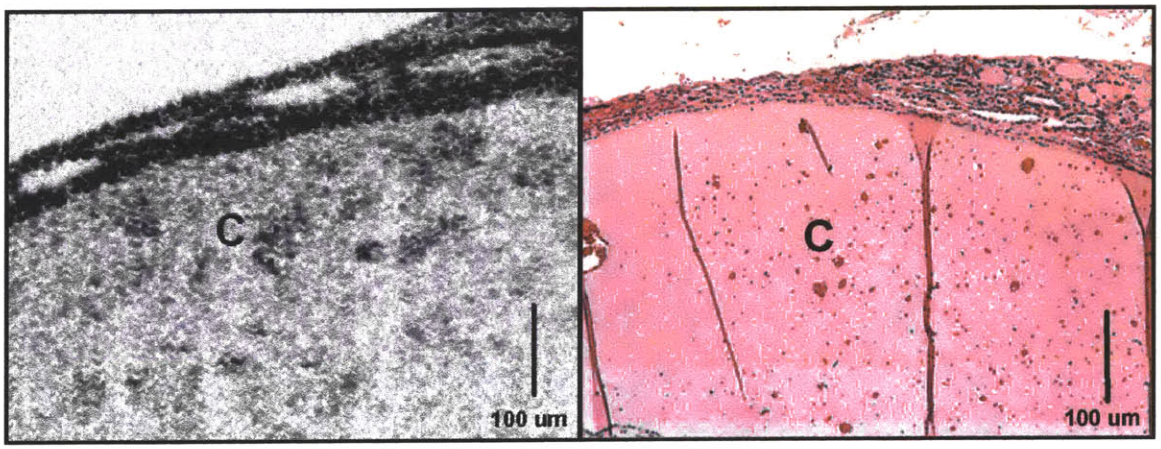

Figure 4.4: Left, Large colloid-filled cyst (C) with adjacent compressed follicles. Right, Histology, Hematoxylin and Eosin 100x. (Wavelength 1.26 µm, Resolution 4.5 µm axial x 11 µm transverse)

Specimens containing solitary benign hyperplastic nodules were also shown to contain both macro- and micro-follicles. Scattered aggregates of lymphocytes identified between follicles in cases diagnosed with lymphocytic thyroiditis were observed. A dense fibrous capsule was visualized around two of the adenomas. Adenomas consisting predominantly of microfollicles, averaging 90 µm in greatest diameter, were distinct in the OCT images (Figure 4.5). Even small abortive follicles could be recognized. Many of the follicles present within adenomas were oval in shape. Regions containing areas of trabecular and solid follicular growth patterns within adenomas were also recognized (Figure 4.6).

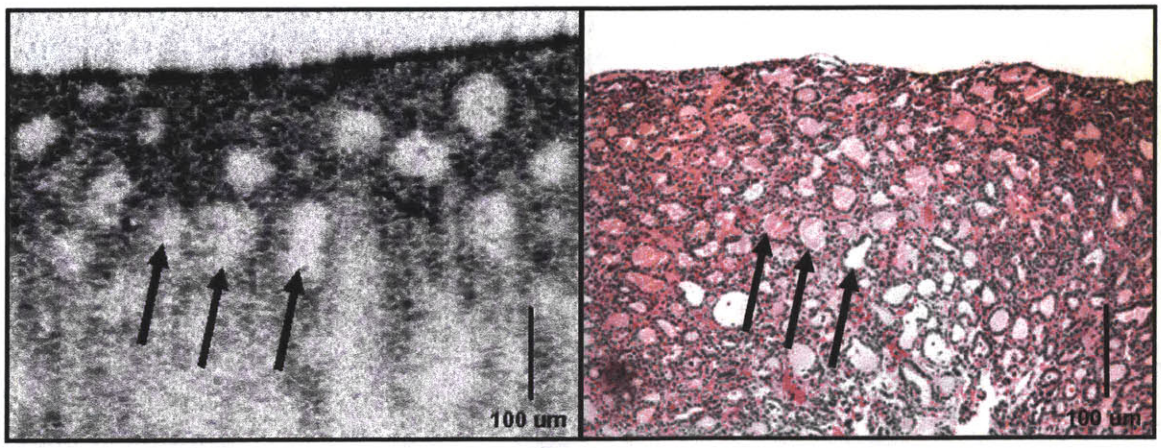

Figure 4.5: Left, Thyroid adenoma comprised of a predominantly microfollicular growth pattern. Right, Histology, Hematoxylin and Eosin 100x. (Wavelength 1.26 µm, Resolution 4.5 µm axial x 11 µm transverse)

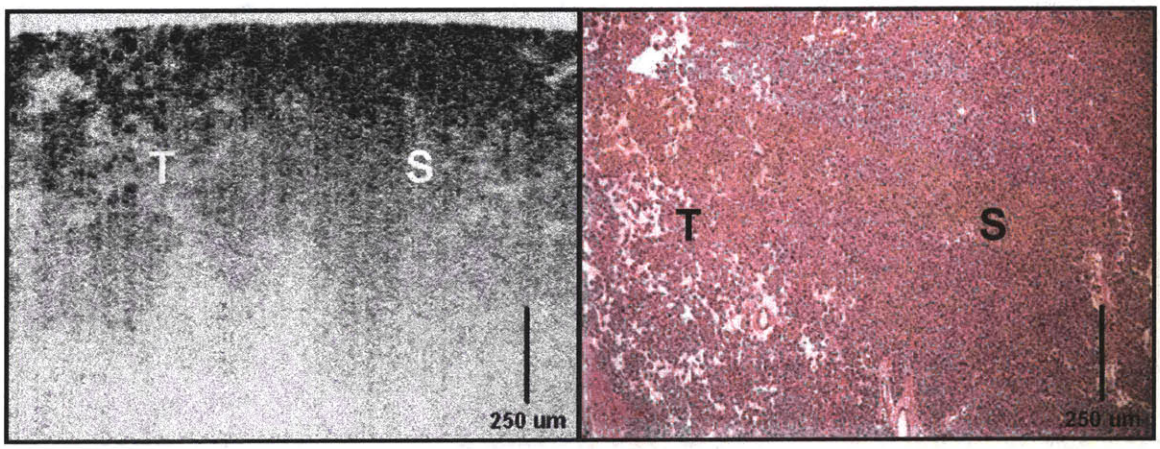

Figure 4.6: Left, OCT image of adenoma with areas showing trabecular (T) and solid (S) growth patterns. Right, Histology, Hematoxylin and Eosin 40x. (Wavelength 1.26 µm, Resolution 4.5 µm axial x 11 µm transverse)

The follicular epithelium in Hürthle cell adenomas was shown to be more highly scattering, and also formed a thicker (up to 30 µm) lining around follicles (Figure 4.7), compared to normal follicles. Many closely packed follicles ranging in size from 15 µm to 45 µm were seen in the follicular variant papillary carcinomas. Areas of dense fibrous scarring in these malignant nodules, often with entrapped malignant follicles, were also found.

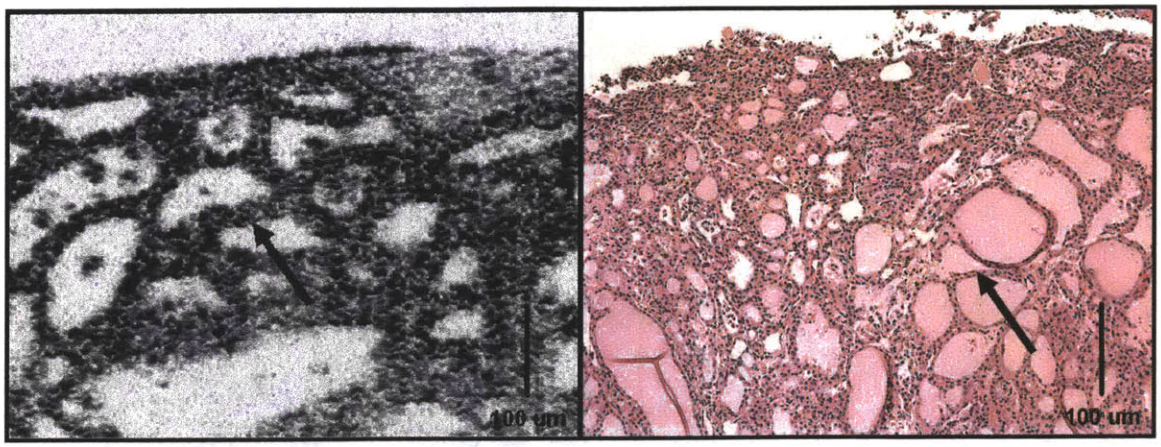

Figure 4.7: Left, OCT image of Hürthle cell adenoma. Note the thick backscattering layer of abundant granular appearing oncocytic epithelium lining follicles. Right, Histology, Hematoxylin and Eosin 100x. (Wavelength 1.26 µm, Resolution 4.5 µm axial x 11 µm transverse)

Such entrapped malignant follicles were markedly irregular, often with jagged edges (Figure 4.8). Finally, calcification (Figure 4.9) and even ossification were distinguished using OCT, and did not prevent tissue imaging.

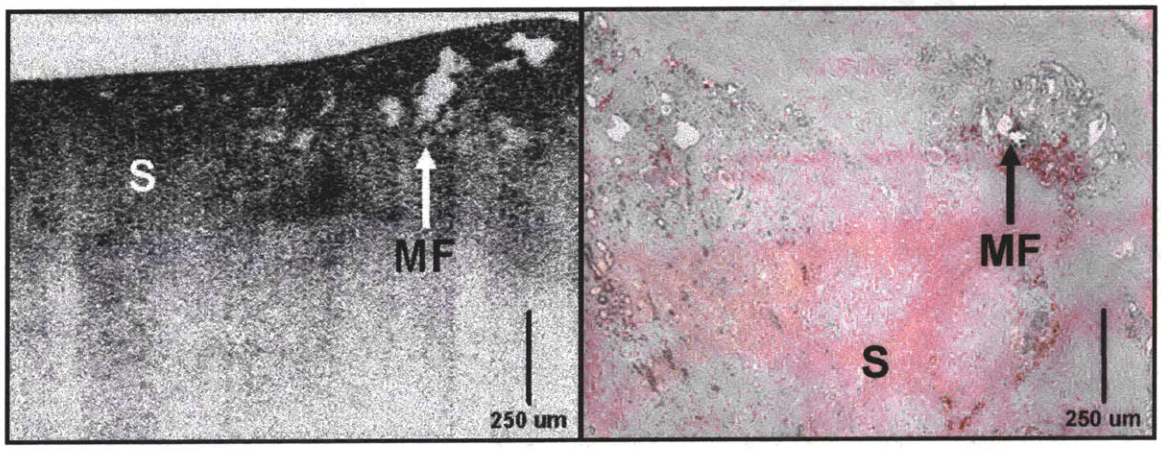

Figure 4.8: Left, OCT image of sclerosing papillary carcinoma. Irregular malignant follicles are entrapped in dense scar tissue. Right, Histology, Hematoxylin and Eosin 40x. (Wavelength 1.26 µm, Resolution 4.5 µm axial x 11 µm transverse)

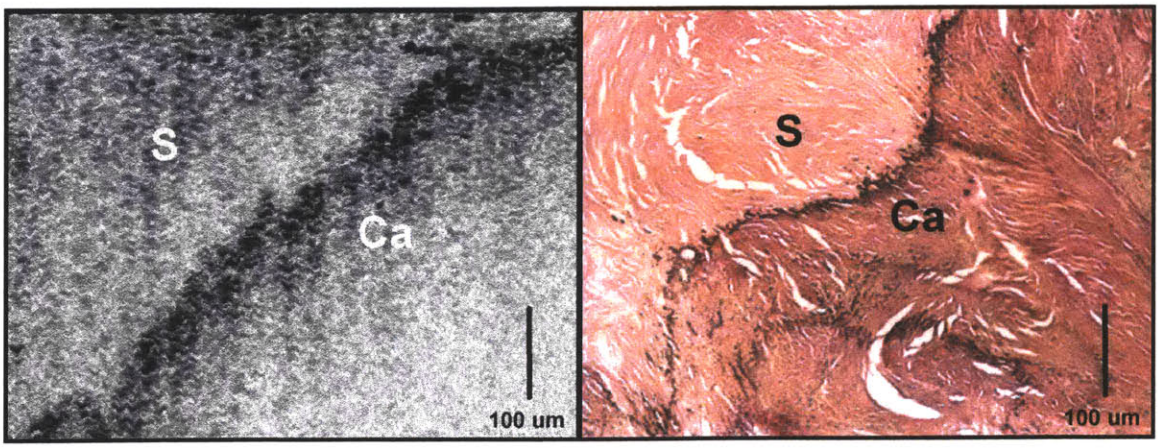

Figure 4.9: Left, Optical coherence tomography image of dystrophic calcification (Ca) adjacent to an area of dense (S) scar tissue. Right, Histology, Hematoxylin and Eosin 100x. (Wavelength 1.26 µm, Resolution 4.5 µm axial x 11 µm transverse)

Preliminary studies using ultrahigh resolution OCT imaging was also performed at 1.1 µm wavelengths with 3.5 µm axial resolution and ~6 µm spot size. This represents a ~25% finer axial resolution and a 2x finer transverse resolution than the previous study. Figure 4.10 shows an example image of thyroid goiter. The follicular cell layer lining individual follicles is clearly visible in the image. Epithelial features were more consistently visible in tissue specimens imaged at 3.5 µm axial resolution and 6 µm spot size compared to 4.5 µm axial resolution and 11 µm spot size.

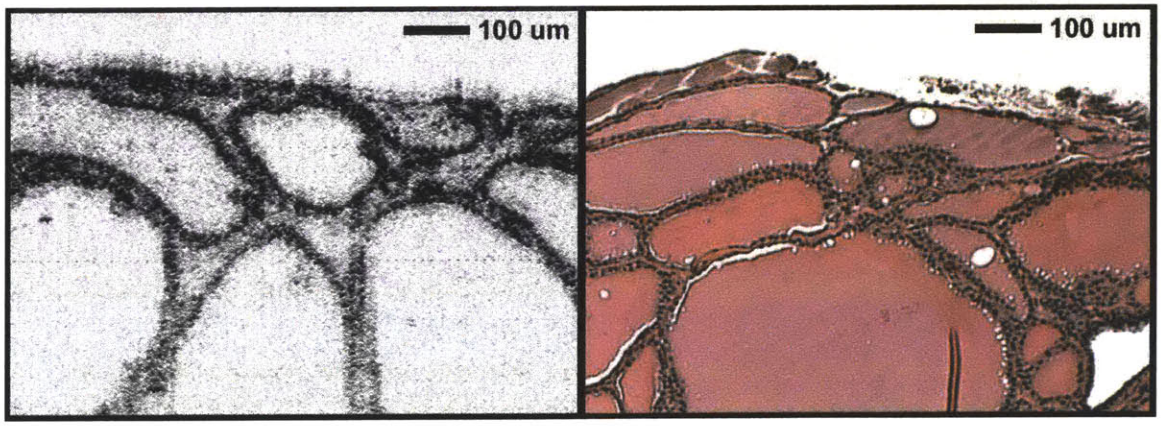

Figure 4.10: Left and center, Thryroid goiter imaged *ex vivo* using 1.1 µm wavelength and 6 µm transverse resolution. The follicular epithelial layer lining individual follicles can be clearly distinguished. Right, Histology, Hematoxylin and Eosin 100x. (Wavelength 1.09 µm, Resolution 3.5 µm axial x 6 µm transverse)

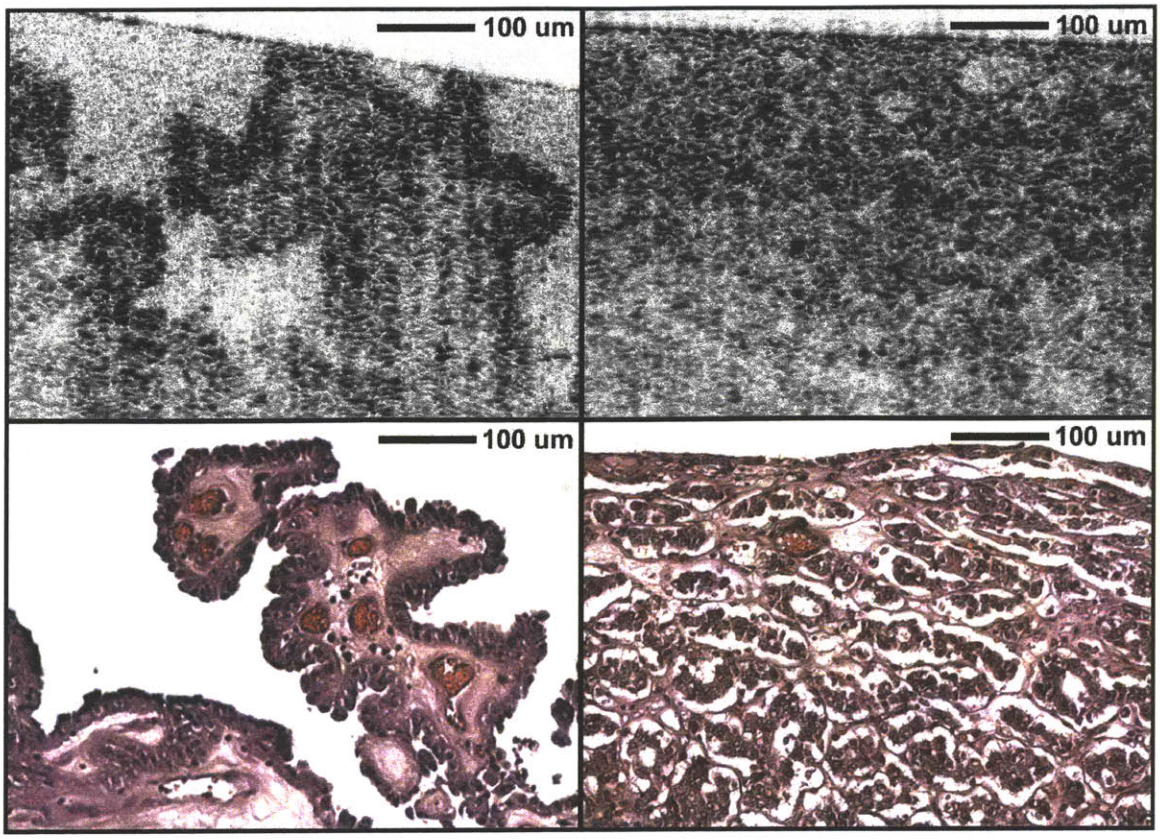

Figure 4.11: Preliminary OCT images of thyroid cancers at 1.1 μm wavelength and 6 μm transverse resolution. Left, Papillary tumor. Right, Solid tumor. Bottom left and right: Histology, Hematoxylin and Eosin 100x. (Wavelength 1.09 μm, Resolution 3.5 μm axial x 6 μm transverse)

Figure 4.11 shows two preliminary images of thyroid cancers at 1.1 μm wavelength and 6 μm transverse resolution. Epithelial lining appeared thickened in the papillary tumor. Microfollicular structures could be clearly identified in the solid tumor.

Figures 12 and 13 show representative 3D OCT sequential *en face* views at different depths beneath the surface of normal thyroid and papillary carcinoma. Three-dimensional imaging allows tracking of features through multiple cross-sectional planes. Three-dimensional information could allow accurate identification of tumor margins for interventional procedures.

Videos showing sequential *en face* slices through normal thyroid and papillary carcinoma are available in the supplemental materials.

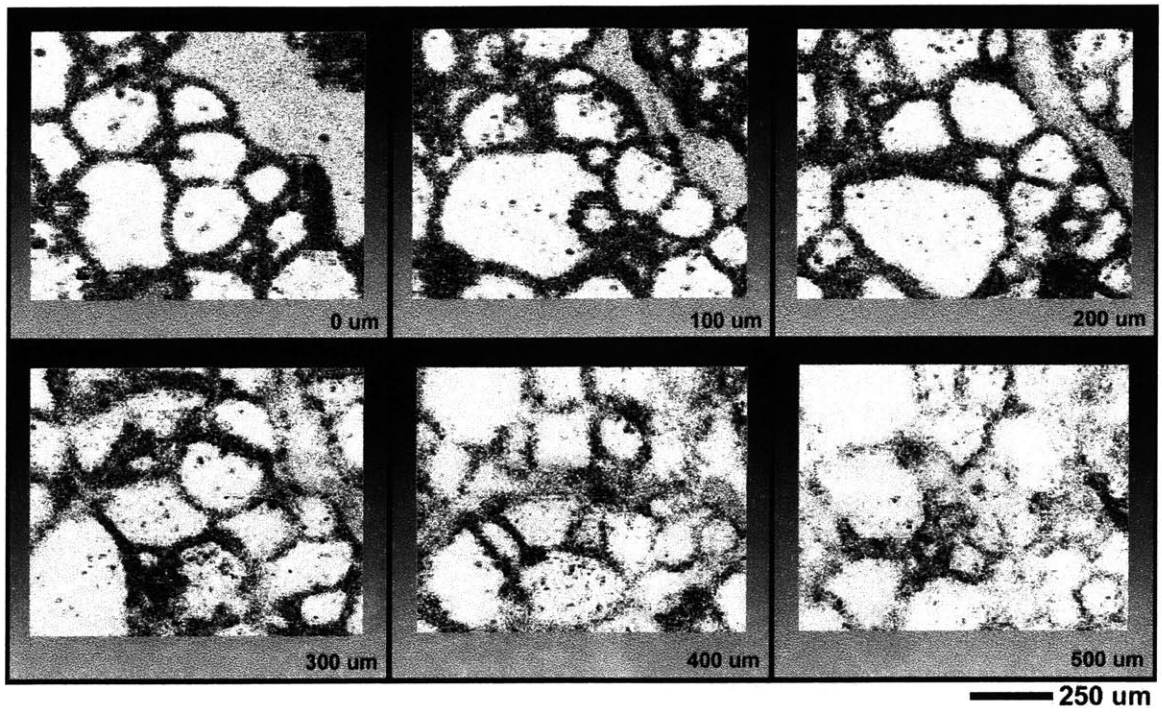

Figure 4.12: Sequential rendered *en face* views of normal thyroid. The rendered volume consisted of 330 transverse slices. Movies showing sequential en face slices are available in the supplemental materials. (Wavelength 1.09 µm, Resolution 3.5 µm axial x 6 µm transverse)

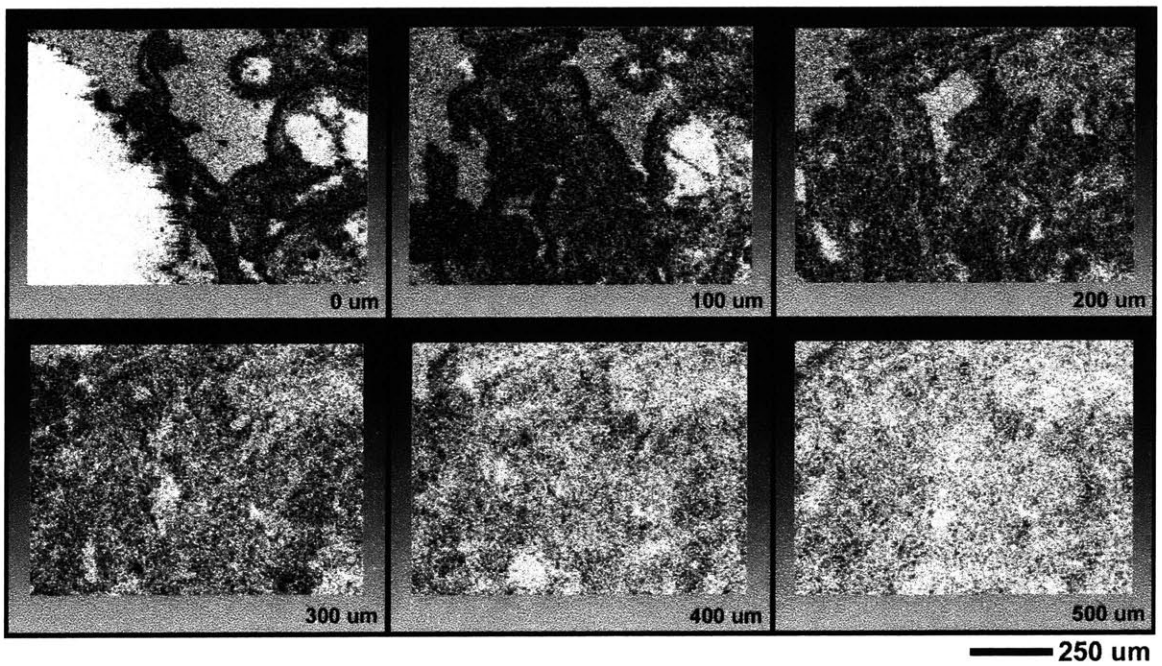

Figure 4.13: Sequential rendered *en face* views of tumor region from the same patient. The rendered volume consisted of 330 transverse slices. Movies showing sequential en face slices are available in the supplemental materials. (Wavelength 1.09 µm, Resolution 3.5 µm axial x 6 µm transverse)

DISCUSSION

Diseases involving the thyroid gland are common. Thyroid nodules, in particular, are a diagnostic challenge frequently encountered in clinical practice. Approximately 4-7% of adults have palpable thyroid nodules, and up to 50-70% can have nodules visible on thyroid ultrasonography.[96] The prevalence of thyroid carcinoma in solitary or dominant nodules is only about 5%.[138] In order to avoid unnecessary thyroidectomy, especially given the fact that thyroid malignancies rarely cause death, it is important to be able to differentiate malignant from benign nodules. However, none of the current imaging modalities can confidently distinguish benign from malignant nodules.[132] The sensitivity of preoperative ultrasound diagnosis, for example, was 86.5% for non-follicular neoplasms and 18.2% for follicular neoplasms in one study.[139]

Ultrasonography is capable of discriminating masses as small as 2 mm in the thyroid gland, and has proven to be most useful in differentiating solid from cystic lesions.[140] However, even large thyroid nodules with acoustic characteristics similar to normal thyroid tissue may be impossible to distinguish by ultrasound.[132] Moreover, acoustic signals are blocked by calcification in the thyroid. MRI permits thinner sections than CT with higher resolution, but at best can only detect thyroid nodules as small as 3-5mm.[132] Despite technical advances, the results of available thyroid imaging modalities have been found not to correlate well with histopathologic findings.[132] Because thyroid carcinoma cannot be distinguished from benign nodules using current imaging techniques, fine needle aspiration cytology has become the primary diagnostic procedure in the evaluation of patients with a thyroid nodule. However, both tissue biopsy and aspiration have limitations. Only a limited amount of tissue is obtained which may not be representative of the entire lesion. Biopsy is also not reliable in the diagnosis of follicular carcinoma, in which evidence of capsular or blood vessel invasion is required for the diagnosis. The potential for OCT to provide information about tissue microstructure, previously only obtained by conventional biopsy, could greatly help in the evaluation of the thyroid gland.

In this study, OCT was used to image thyroid tissue *ex vivo*. These results demonstrate the feasibility of this novel modality for clinical imaging of the thyroid gland. Individual thyroid follicles on the order of 15 μm were easily resolved. This resolution is higher than any available imaging technology of the thyroid gland. Normal thyroid follicles have an average diameter of 200 μm.[141] The ability to delineate individual follicles permits the growth pattern (macrofollicular, microfollicular, mixed and solid) of thyroid tissue including nodules to be determined. This conveys valuable information because lesions found to contain macrofollicles are likely benign, whereas nodules comprised predominantly of microfollicles are more likely to be neoplastic. Assessment of follicle shape may also provide valuable information. Normal follicles are round to oval in shape. Elongate follicles are abnormal, suggesting hyperplastic or neoplastic conditions, or could result from compression of an adjacent expanding mass.[142]

OCT was able to identify the backscattering epithelial layer lining follicles. This epithelial lining was found to be more prominent in lesions exhibiting oncocytic (Hürthle) cell changes. Improved resolution as shown in the preliminary imaging study at 1.1 μm wavelengths demonstrated that this epithelial lining could be more clearly visualized. Although not shown in this study, it is possible that OCT may be able to distinguish flat to low cuboidal epithelium of inactive follicles from columnar follicular cells of active follicles. Papillary projections into the

lumen of large follicles were recognized. These are normally present in thyroid tissue, but may be accentuated in hyperplastic conditions.[142] Epithelial-lined papillae containing fibrovascular cores, a feature of some papillary thyroid carcinomas, are therefore likely to be detected when imaged using OCT. In the imaged thyroid specimens, colloid was easily identified, including those follicles that contained debris and hemorrhage. The focal regions of high scattering visible in the colloid of many follicles corresponded to the basophilic flocculent colloid clumps normally found in thyroid tissue.[139, 141, 142] OCT was also able to clearly image the intervening connective tissue stroma, fibrous septae, capsules surrounding nodules and areas of degeneration (hemorrhage, scarring, and cyst formation). This study also demonstrated ultrahigh resolution 3D OCT imaging. 3D imaging and volume rendering provided complementary information to cross-sectional OCT images, enabling visualization of arbitrary planes and rendering of surface topography as well as subsurface tissue microstructure. The ability to visualize multiple imaging planes enables the three-dimensional follicular organization to be assessed in a way not possible using individual OCT images. No cases of follicular carcinoma were available to study. The utility of 3D OCT for assessing capsular or vascular invasion using OCT was not investigated.

The superficial location of the thyroid gland makes it an easy structure to image clinically. The major technical limitation of this study, however, is the fact that the micron-scale resolution we achieved was limited to a depth of approximately 1.5 mm. At present, this would restrict the clinical utility of OCT to the intraoperative setting, or would require insertion of an optical imaging device into the thyroid gland. Because OCT is fiber optically based, imaging can be performed inside solid tissues or organs using needles of 27 gauge or smaller.[53] A needle based OCT imaging device could image a cylindrical region of tissue measuring 6 mm in diameter and several mm in length. OCT imaging can also be integrated with biopsy devices to guide placement prior to excision of a specimen. Future developments currently underway to improve the performance of OCT promise to yield further improvements in both resolution and contrast. *In vivo* cellular level OCT imaging in embryology specimens has been achieved.[143] The capacity to identify individual cells and assess their nuclei may prove extremely useful in the assessment of papillary thyroid carcinoma. Modern OCT systems, as employed in this study, are compact and portable and can provide image acquisition rates in real time. Three-dimensional digital image data sets can also be generated. Moreover, color Doppler OCT is now available, enabling real-time flow velocity measurements to be obtained simultaneously with tissue structural information.[144, 145] This will allow the blood flow dynamics in thyroid lesions to be observed simultaneously with micron-scale resolution cross-sectional imaging.

CONCLUSION

This chapter demonstrates for the first time that high-resolution cross-sectional imaging of thyroid tissue using OCT is feasible. OCT images obtained correlate well with conventional histopathology and has the potential to provide reliable and clinically useful information of normal, benign and malignant thyroid tissue that until now has only attainable by conventional histopathologic examination. These results suggest that this OCT may be a promising diagnostic tool in the evaluation of patient's with thyroid disease, helping to better select patients with a high risk of having a malignant lesion. Since the prognosis of thyroid cancer is partially dependent on its size at surgery, earlier beneficial detection of cancer may be possible using OCT as an adjunct to current imaging techniques.

Chapter 5

Ultrahigh Resolution and Three-Dimensional OCT Imaging of the Large and Small Intestine

INTRODUCTION

Colorectal cancer (CRC) is a common, lethal, and preventable disease. Approximately 146,000 new cases of colorectal cancer are diagnosed each year in the United States, and approximately one in three people who develop CRC die of the disease. CRC ranks second only to lung cancer as a cause of cancer death, accounting for 10 to 11% of cancer deaths overall, and it is third both in frequency and in cause of cancer death in men and women separately. Despite these grim statistics, the incidence rate of CRC has declined slightly by approximately 3% per year since 1998, and mortality rates have decreased by an average of 1.7% per year since 1989. These declines have been attributed to both increased screening for and removal of polyps before they progress to invasive cancer and improved treatment methods.[2]

The majority of colonic carcinomas are endoluminal, making them amenable to early detection by means of endoscopy. There has therefore been significant interest in the development of improved diagnostic techniques to detect early stage colorectal disease. Identification of high-risk groups and endoscopic surveillance remains the best method for detecting early stage malignancy. Early detection and treatment can improve survival rates to 90%.[2] However, detection of microscopic changes within the mucosa and submucosa is still currently beyond the capabilities of routine endoscopic techniques. Recent analysis of missed lesions in the detection of both gastric and colon cancers suggests that there exists a need for more accurate diagnosis of non-polypoid mucosal lesions.[146, 147] Developments in endoscopic mucosal resection (EMR) as a minimally invasive technique for treating early-stage gastrointestinal cancers has also lead to a demand for improved endoscopic imaging for accurate staging of the depth of tumor invasion.

OPTICAL COHERENCE TOMOGRAPHY

Optical coherence tomography (OCT) is an emerging imaging modality which can generate micron-resolution, cross-sectional images of tissue microstructure in situ and in real time.[3, 4, 103, 148] OCT can be incorporated into a wide variety of endoscopic and laparoscopic imaging devices.[51, 52, 110] OCT has the advantage of enabling subsurface visualization of microscopic mucosal and submucosal architectural features which are not visible using standard endoscopy.

Early investigations of OCT imaging focused on *ex vivo* imaging of gastrointestinal tissues to establish correlations with histopathology and feasibility for future endoscopic studies.[9, 106-108, 117] With the development of fiber optic endoscopes, *in vivo* OCT imaging in animals was demonstrated.[51] Several groups have performed clinical endoscopic OCT imaging studies[64-72, 110, 149-153] Much of this clinical work has focused on the upper gastrointestinal tract, where Barrett's esophagus, esophageal adenocarcinoma, and normal gastric cardia were visualized. Excellent sensitivities and specificities were demonstrated for detecting Barrett's esophagus.[72] OCT imaging can also be applied to the large and small intestine, such as for endoscopic surveillance, detection, staging, and follow up of colorectal cancer. Recent work has shown that OCT has potential to distinguish hyperplastic from adenomatous polyps in the colon and suggests models for detecting dysplasia.[73]

Virtually all endoscopic studies to date have been performed with axial image resolutions of 10-15 μm at 1.3 μm wavelengths. However, OCT technology is rapidly evolving and performance has improved significantly. Standard OCT systems use superluminescent diode light sources which are commercially available, compact and low cost, but have limited bandwidths and wavelengths. For this reason, all previous endoscopic imaging studies had limited axial resolutions of 10-15 μm at 1.3 μm wavelengths. In addition, most endoscopic imaging studies used relatively low numerical aperture focusing, limiting transverse resolutions to ~15-30 μm. Using femtosecond laser light sources it is possible to achieve ultrahigh axial image resolutions approaching ~1-2 μm, a factor of ~10x improvement over standard resolution OCT.[86, 87, 89, 92, 96] These femtosecond laser light sources also enable new wavelength ranges which are not accessible by superluminescent diodes. Recently, ultrahigh resolution *in vivo* endoscopic OCT imaging in an animal model has been demonstrated with an axial resolution of 3.7 μm in tissue using a 1.3 μm wavelength femtosecond Cr:Forsterite laser light source.[154]

This chapter investigates new ultrahigh resolution OCT technology for imaging the large and small intestine. In this study, normal, inflammatory, and neoplastic tissues of the large and small intestine were imaged *ex vivo* and correlated with histology. Imaging was performed using portable, ultrahigh resolution OCT systems in the clinical pathology laboratory. Imaging in the pathology laboratory allows rapid access to surgical specimens, reducing possible artifacts from tissue degradation. This method also enables accurate registration of OCT images with histology, which is difficult to achieve in endoscopic OCT imaging.

Ultrahigh resolution OCT imaging at ~1.3 μm wavelength was performed with 4.5 μm axial resolution and 11 μm spot size using a compact Cr:Forsterite laser light source. This study evaluates improved resolution using the standard OCT imaging wavelength of 1.3 μm. Complementary studies on a smaller set of specimens were performed at ~1.1 μm wavelength with a 3.5 μm axial resolution and 6 μm spot size using a Nd:Glass laser light source. The Nd:Glass laser has the important advantage of being compact and commercially available and is therefore more suitable for future clinical endoscopic imaging studies. This system performs imaging at wavelengths shorter than the wavelength typically used in OCT. The transverse spot size was chosen to be small in order to improve transverse resolution. Finally, three-dimensional OCT imaging was performed to investigate the utility of 3D visualization of tissue architectural morphology. These studies are an important step toward developing new OCT technology for

future clinical endoscopic imaging applications and could help serve as a baseline for future ultrahigh resolution endoscopic OCT studies.

METHODS

Ultrahigh Resolution OCT Systems and Imaging Parameters

The physical principles of OCT have been described previously.[3, 4] Cross-sectional images of internal tissue microstructure are generated by scanning a beam of light on tissue and measuring the echo time delay and magnitude of backscattered or backreflected light. OCT images are two-dimensional data sets displayed as grey scale or false color images, representing the optical backscattering or backreflection in a cross-sectional plane. Three-dimensional volume datasets can be generated by combining a registered set of transverse OCT scans, allowing visualization from different virtual perspectives and rendering of tissue architectural morphology.

This study investigates new ultrahigh resolution OCT imaging technology for imaging normal and pathologic tissues of the large and small intestine and correlates images with histology. The study has three parts. Ultrahigh resolution OCT imaging was performed with 4.5 μm axial resolution in tissue, a factor of 2-3x finer than standard endoscopic OCT systems. This OCT system used a femtosecond Cr:Forsterite laser light source at a center wavelength of 1260 nm with a 180 nm bandwidth.[94] The transverse spot size was set to ~11 μm full width half maximum (FWHM), a factor of 1.5-2x finer than standard endoscopic OCT. The depth of field was calculated to be ~400 μm. Imaging was performed using an imaging probe (~1 cm x 15 cm diameter x length) with a Hopkins lens relay system and beam scanning using galvanometer mirrors, enabling real time visualization and adjustment of the OCT imaging plane. For comparison with ultrahigh resolution OCT imaging results, imaging was also performed on a specimen of normal colon using typical standard resolution OCT parameters at 1300 nm wavelength with 12 μm axial resolution in tissue. Imaging was performed using a commercially available superluminescent diode light source using equivalent system sensitivity parameters. The transverse spot size was set to ~23 μm (FWHM), comparable to endoscopic OCT imaging parameters. Imaging was also performed using a transverse spot size of ~9 μm (FWHM) in order to investigate the effect of improved transverse resolution at standard axial resolutions.

Ultrahigh resolution OCT imaging was also performed with 3.5 μm axial resolution in tissue. This OCT system used a femtosecond Nd:Glass laser light source at a center wavelength of 1090 nm with ~150 nm bandwidth.[96] This laser is commercially available (High Q Laser Productions, Hohenems, Austria) and is compact, robust, and turnkey, making it suitable for future clinical studies. Although shorter wavelengths are attenuated more rapidly by tissue scattering, they enable finer axial resolutions for a given bandwidth as well as smaller spot sizes. The transverse spot size was set to be ~6 μm (FWHM) to examine the effects of improved transverse resolution. This transverse spot size is a factor of 3-4x finer than standard endoscopic OCT. The depth of field was calculated to be ~140 μm. OCT imaging was performed using post objective scanning in order to avoid aberrations and preserve the small spot size.

Three-dimensional OCT imaging was performed at 1090 nm wavelengths. Three-dimensional data sets consisting of 200 to 350 individual OCT images spaced by 3 μm to 5 μm apart were

generated by raster scanning the beam. A 5 μm spacing was chosen for specimens with large architectural features and a 3 μm spacing was used for all other specimens. Each OCT image in the raster scan consisted of 600-1800 transverse pixels over 1-2 mm. This resulted in an axial scan spacing of 0.6-3 μm by 3-5 μm. The 3D OCT data was processed and visualized using MRI software for 3D visualization and volume modeling (Amira, Mercury Computer Systems, Berlin).

Specimen Imaging and Handling

Imaging studies were performed on freshly excised surgical specimens in the pathology laboratory of the Beth Israel Deaconess Medical Center. These studies were approved by the Institutional Review Board (IRB) at the Beth Israel Deaconess Medical Center and the Committee for the Use of Humans as Experimental Subjects (COUHES) at the Massachusetts Institute of Technology. Informed consent was not required since the study involved only database review and *ex vivo* surgical specimens. Fresh specimens were selected based on the presence of pathology upon gross examination, prompt arrival in the pathology laboratory, and large specimen size, allowing normal and pathologic tissue to be collected from each specimen for the study without interfering with routine diagnostic procedures. In selected cases, specimens used for clinical diagnostic purposes were imaged immediately prior to placement in cassettes for standard processing. Specimens experiencing excessive prior handling were excluded from the study because of possible damage to the fragile mucosa. All specimens available during the duration of the study which met these criteria were imaged. The study was concluded when a representative set of normal specimens and common neoplastic pathologies was obtained. The study duration was 4 weeks for the first part of the study imaging at 1.3 μm and 2 weeks for the second part of the study imaging at 1.1 μm wavelengths.

Normal and diseased intestinal tissues from surgical resections were imaged within three hours of excision. A total of 65 sites from 23 surgical specimens from adult patients were imaged. Both normal and pathologic sites from each specimen were imaged. Sites which had experienced excessive handling, such as within 1-2 mm of the surgical margin of the specimen, were not imaged. The majority of specimens were imaged with the 1.3 μm wavelength OCT system. Normal intestinal sites imaged in this first phase of the study included duodenum (n = 2), jejunum (n = 5), and colon (n = 11). Diseased tissue sites included inflammatory bowel disease (n = 9; ulcerative colitis n = 8; Crohn's disease n = 1), and neoplasia (n = 6), with one tubulovillous adenoma involving the duodenum, one submucosal lipoma, three sites of invasive adenocarcinoma involving the colon, and one squamous cell carcinoma in the anorectal region. A smaller set of specimens were imaged with the 1.1 μm wavelength OCT system. Sites imaged in the second phase of the study included normal colon (n = 11), ulcerative colitis (n = 2), and five sites of adenoma or invasive adenocarcinoma. Specimens with ulcerative colitis of varying severity, ranging from minimal to severe inflammation and ulceration were imaged. Grossly normal as well as ulcerated and scarred lesions (n = 14) were also imaged.

Since the OCT light was in the near infrared and invisible to the eye, image registration was performed with a visible green guiding beam which was coincident with the OCT imaging beam. Imaging was performed without contact to the tissue to prevent artifacts introduced from tissue compression. All images were scaled in the axial direction by 1.38x to correct for the

approximate index of refraction of tissue.[102] When necessary, specimens were irrigated (isotonic saline or RPMI 1640) to prevent dehydration during imaging. Specimens were marked at the beginning and end of each OCT scan with microinjections of ink to designate the imaging plane orientation. When necessary, after imaging and inking, specimens were immersed in Bouin's fixative for 2 seconds to fix the ink and prevent smearing. Specimens were then placed in 10% buffered formalin, routinely processed and paraffin embedded. Multiple 5 μm thick tissue sections were obtained from the OCT imaging plane and stained with Hematoxylin and Eosin. OCT images and corresponding histology sections were compared. Minor discrepancies between histology and OCT images can be attributed to tissue fixation, processing and sectioning artifacts.

RESULTS

OCT images and histology photomicrographs at 40x to 200x magnification are shown with corresponding size scale bars. Histology is scaled with the same magnification as the OCT image. Ultrahigh resolution OCT imaging results at 1.3 μm wavelengths with 4.5 μm axial resolution and ~11 μm spot size are presented first. This is 2-3x finer axial resolution and 1.5-2x finer transverse resolution than previous *ex vivo* and endoscopic studies and imaging is at the same wavelength as previous studies.

Imaging of normal colon produced distinct images of the mucosa and submucosa characteristic of normal colonic microstructure. Figure 5.1 shows a representative ultrahigh resolution OCT image of the normal colon and corresponding histology. OCT clearly visualized the full thickness of the colon mucosa in almost all specimens. The submucosa appeared as a lighter and less optically scattering layer. The muscularis mucosa appeared as a scattering band in the OCT image separating the mucosa and submusoca. Although the epithelial layer and single crypts were visible, they were not consistently visible in all images. Enhanced optical signal intensity beneath individual crypt structures was observed and may be the result of increased transmission of the light through the crypts.

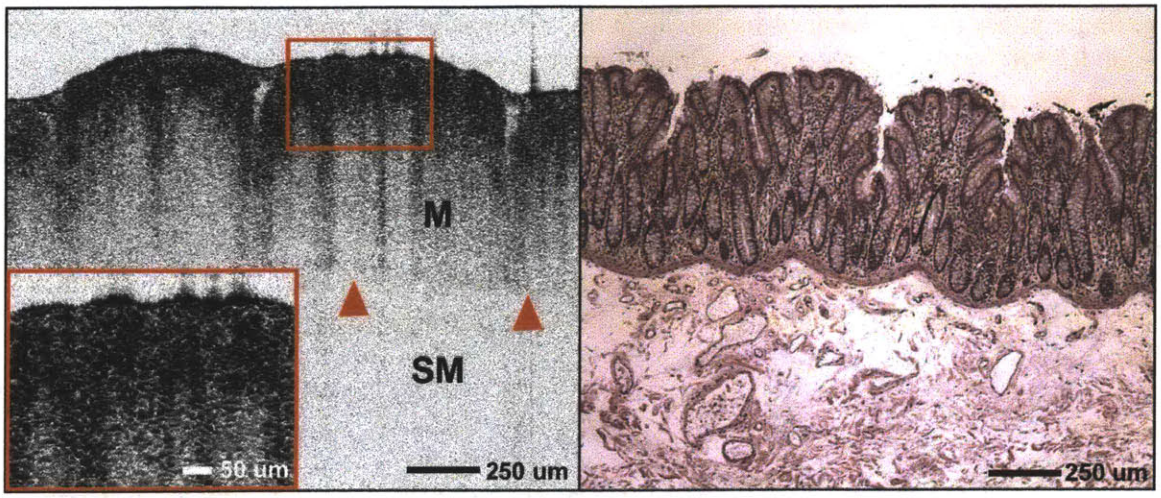

Figure 5.1: Left, Ultrahigh resolution OCT image of normal colon. Mucosa (M) is clearly delineated from underlying submucosa (SM) by a scattering band corresponding to the thin muscularis mucosa (arrows). The submucosa is visible as less optically scattering layer. Inset, Magnified view of the OCT image. Right, Histology, Hematoxylin and Eosin 40x. (Wavelength 1.26 μm, Resolution 4.5 μm axial x 11 μm transverse)

In comparison, Figure 2A shows a representative OCT image of normal colon mucosa acquired with typical standard resolution OCT imaging parameters at 1.3 μm wavelength, 12 μm axial resolution, and 23 μm transverse resolution. Speckle was clearly visible at standard resolutions, degrading overall image quality compared to the ultrahigh resolution OCT imaging in Figure 1. Figure 2B shows a standard resolution OCT image acquired on the same specimen with identical wavelength and axial resolution as Figure 2A, but with a further ~2.5x improvement in transverse resolution obtained by focusing to smaller spot sizes. Improving transverse resolution reduced speckle, yielding notable improvement in image sharpness. However, ultrahigh resolution OCT images with ~2.5x improvement in both axial and transverse resolution enabled visualization of the epithelial layer and fine structure in the mucosa. Imaging with improved overall resolution significantly reduced image degradation due to speckle, improving image quality.

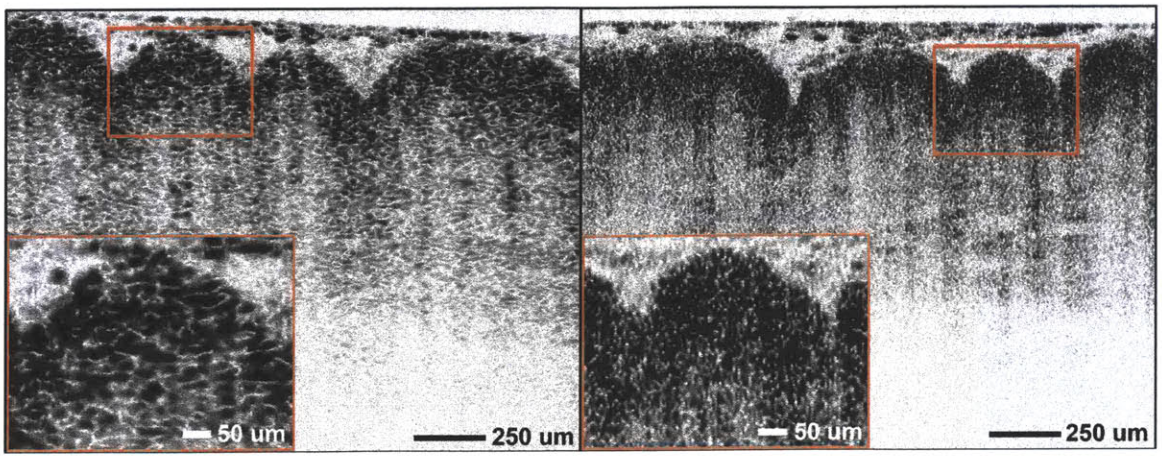

Figure 5.2: Left, OCT image of normal colon mucosa acquired using typical standard resolution imaging parameters. Image degradation due to speckle is clearly evident. (Wavelength 1.3 μm, Resolution 11.6 μm axial x 23 μm transverse) Inset left, Magnified view of the OCT image. Right, OCT image of the same specimen acquired with ~2.5x improved transverse resolution. (Wavelength 1.3 μm, Resolution 11.6 μm axial x 9 μm transverse) Inset right, Magnified view of the OCT image.

Figure 5.3 shows a representative ultrahigh resolution OCT image of normal small intestine and corresponding histology. Villi of varying sizes can be clearly distinguished in the OCT images. The epithelial cell layer lining individual villi was also visible in the small intestine as a band measuring 25-40 μm in thickness. The submucosa again appeared as a lighter and less optically scattering layer.

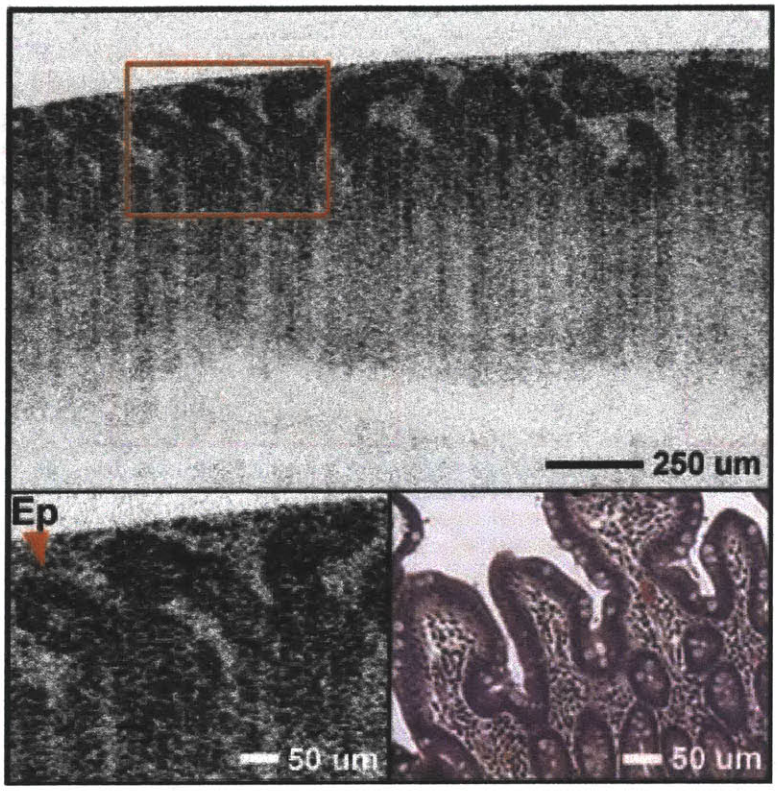

Figure 5.3: Left, Ultrahigh resolution OCT image of normal small intestine. Villi of varying sizes can be distinguished. The epithelial cell layer (Ep) was visible as a thin scattering band 25-40 μm in thickness lining individual villi. Mucus is visible between the villi in the images. Histology, Hematoxylin and Eosin 100x. (Wavelength 1.26 μm, Resolution 4.5 μm axial x 11 μm transverse)

Figure 5.4 shows a representative OCT image and histology of chronic ulcerative colitis. In mild disease, a disrupted mucosal surface due to ulceration and erosion of the epithelium was visible. With more severe disease, irregular and distorted glands characteristic of chronic inflammatory bowel disease were evident. Markedly increased inflammatory cells within the supporting lamina propria appeared as highly scattering. Figure 5.5 shows an image of Crohn's disease of the colon. Abundant irregular branching glands are apparent in the OCT images and histology. The dense inflammatory infiltrate in the lamina propria was again highly scattering. No cases complicated by dysplasia were available to study.

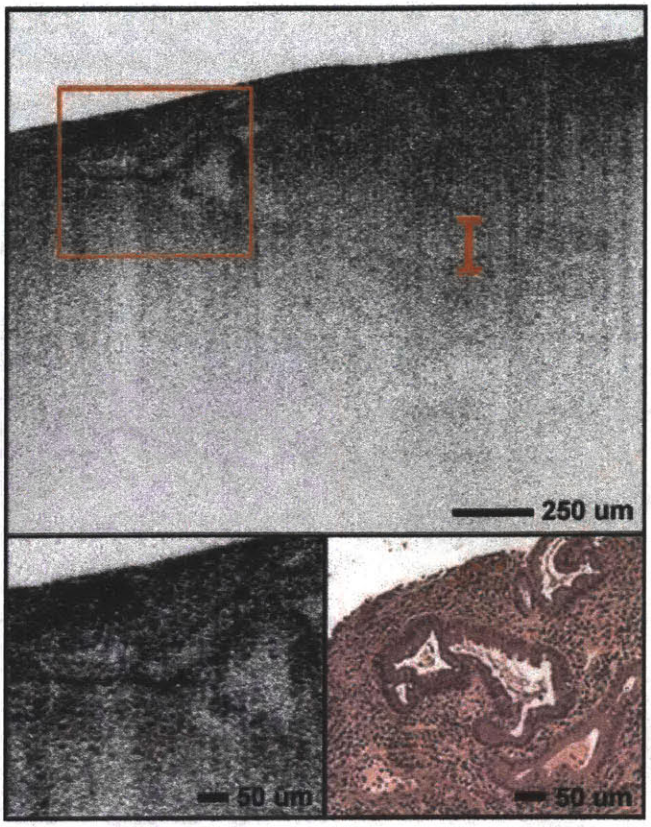

Figure 5.4: Ultrahigh resolution OCT image of ulcerative colitis showing a disrupted mucosal surface due to ulceration and erosion, architectural distortion of glands, and increased scattering due to chronic inflammatory infiltrate (I) in the lamina propria. Histology, Hematoxylin and Eosin 100x. (Wavelength 1.26 µm, Resolution 4.5 µm axial x 11 µm transverse)

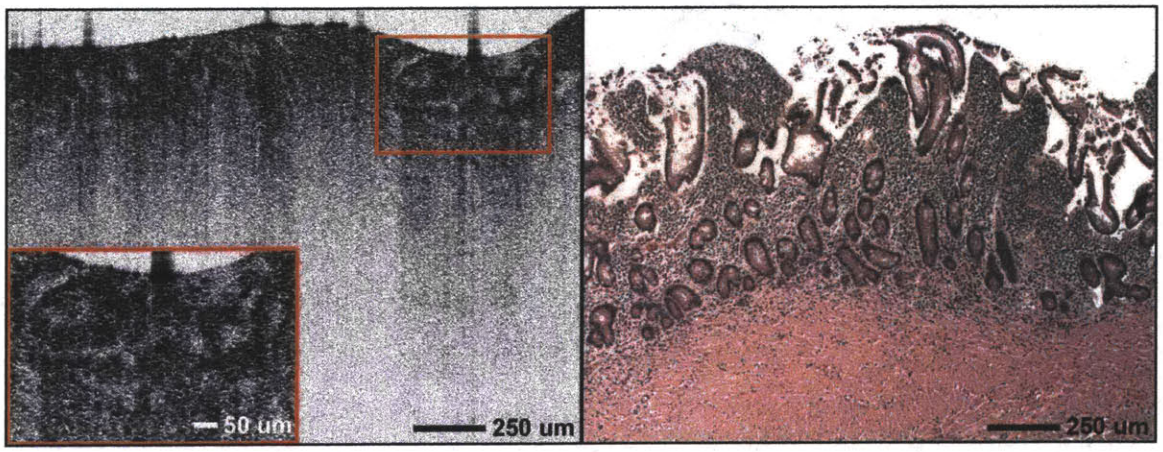

Figure 5.5: Left, Ultrahigh resolution OCT image of chronic colitis due to Crohn's disease showing branching irregular glands and increased scattering due to dense inflammatory infiltrate in the lamina propria. Inset, Magnified view of the OCT image. Right, Histology, Hematoxylin and Eosin 40x. (Wavelength 1.26 µm, Resolution 4.5 µm axial x 11 µm transverse)

Figure 5.6 shows an OCT image and corresponding histology of adenocarcinoma. Figure 5.7 shows an OCT image and corresponding histology of invasive squamous carcinoma of the anus. OCT images of both types of carcinoma revealed complete loss of normal mucosal architecture and invasion of the submuscosa. Highly scattering and irregular invasive glands were visible in OCT images of adenocarcinoma. Tongues of squamous epithelium in OCT images of squamous cell carcinoma also appeared with increased scattering compared to surrounding regions, and were seen to extend irregularly into the stroma. OCT images also showed areas with cysts and ulceration with overlying fibrinopurulent exudate.

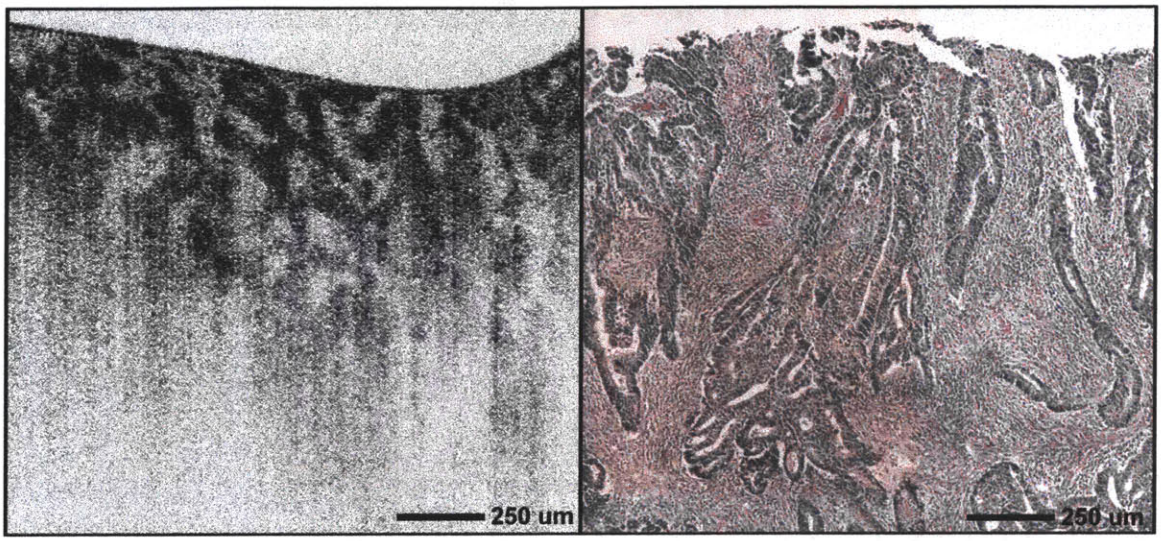

Figure 5.6: Left, Ultrahigh resolution OCT image of well-differentiated adenocarcinoma. Highly irregular invasive glands are visible in a desmoplastic stroma. No clear boundary between mucosa and submucosa is evident in this case. Right, Histology, Hematoxylin and Eosin 40x. (Wavelength 1.26 μm, Resolution 4.5 μm axial x 11 μm transverse)

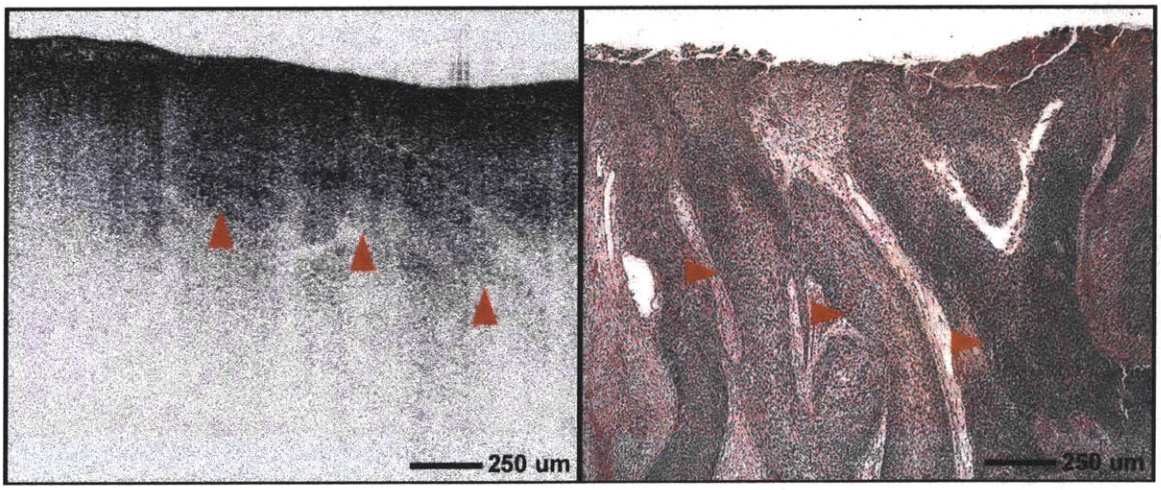

Figure 5.7: Left, Ultrahigh resolution OCT image of invasive squamous cell carcinoma of the anus with surface ulceration. Irregular tongues of malignant epithelium can be seen extending into the underlying stroma (arrows). Right, Histology, Hematoxylin and Eosin 40x. (Wavelength 1.26 μm, Resolution 4.5 μm axial x 11 μm transverse)

Figure 5.8 shows an OCT image and corresponding histology of a tubulovillous adenoma of the duodenum. OCT images of tubulovillous adenoma also showed loss of normal mucosa architecture with the formation of deep folds consistent with villous architecture. Regions of high scattering intensity were observed in the epithelium of the tubular adenoma. Figure 5.9 shows an OCT image and corresponding histology of a well-circumscribed lipoma within the submucosa. Adipocytes appeared clear and low scattering, with individual well-circumscribed cell borders and intervening septae. Loss of the epithelium is evident in the histology and is the result of processing artifacts.

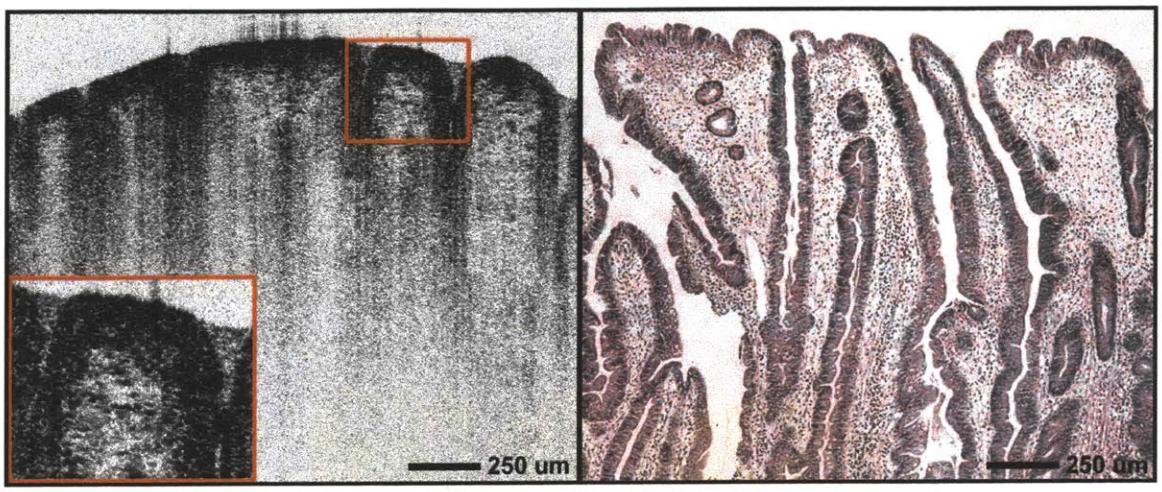

Figure 5.8: Left, Ultrahigh resolution OCT image of a tubulovillous adenoma of the duodenum. Loss of normal mucosal structure is apparent and architecture correlates well with histology. Inset, Magnified view of the OCT image. Right, Histology, Hematoxylin and Eosin 40x. (Wavelength 1.26 µm, Resolution 4.5 µm axial x 11 µm transverse)

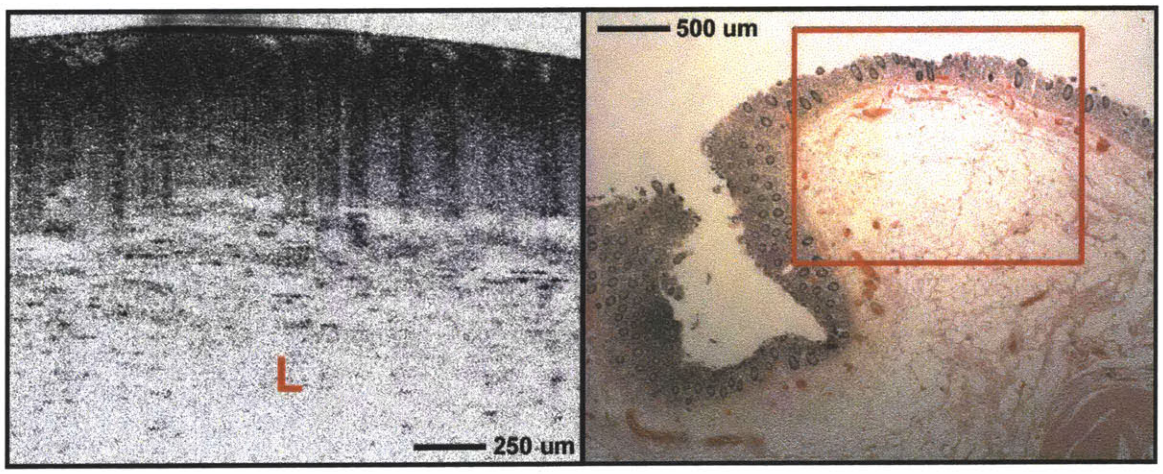

Figure 5.9: Left, Ultrahigh resolution OCT image of a submucosal lipoma (L). Adipocytes appeared low scattering, with circumscribed borders of increased scattering. Erosion of the colon mucosa is evident in the histology and is the result of processing artifacts. Right, Histology, Hematoxylin and Eosin 20x. (Wavelength 1.26 µm, Resolution 4.5 µm axial x 11 µm transverse)

Ultrahigh resolution OCT imaging was also performed at 1.1 µm wavelengths with 3.5 µm axial resolution and ~6 µm spot size. This represents a 2-3x finer axial resolution and a 3-4x finer transverse resolution than previous *ex vivo* and endoscopic studies. These studies use a Nd:Glass laser which operates at shorter wavelengths than previous studies. However, lasers at this wavelength are more readily available and suitable for future clinical use.

Figure 5.10 shows a representative OCT image and corresponding histology of normal colon at 1.1 µm wavelength with ~6 µm transverse resolution. The finer transverse resolution more clearly delineates the individual crypt structures and the epithelial layer than images at 1.3 µm wavelength. The epithelium is visible as a distinct layer, approximately 40-50 µm in thickness, delineated by a thin, highly scattering band from the supporting lamina propria. Individual crypts as well as the epithelial layer lining the crypts are visible. Enhanced scattering beneath the individual crypts was also observed. Since a smaller focused spot size of ~6 µm was used in the 1.1 µm wavelength studies, versus ~11 µm in the 1.3 µm wavelength studies, the depth of field is reduced. With the OCT beam focus set at ~100 µm below the surface, structures within 200-250 µm of the surface could be clearly resolved. Deeper structures were out of focus and appeared lower scattering. The submucosa was therefore not visible in most specimens.

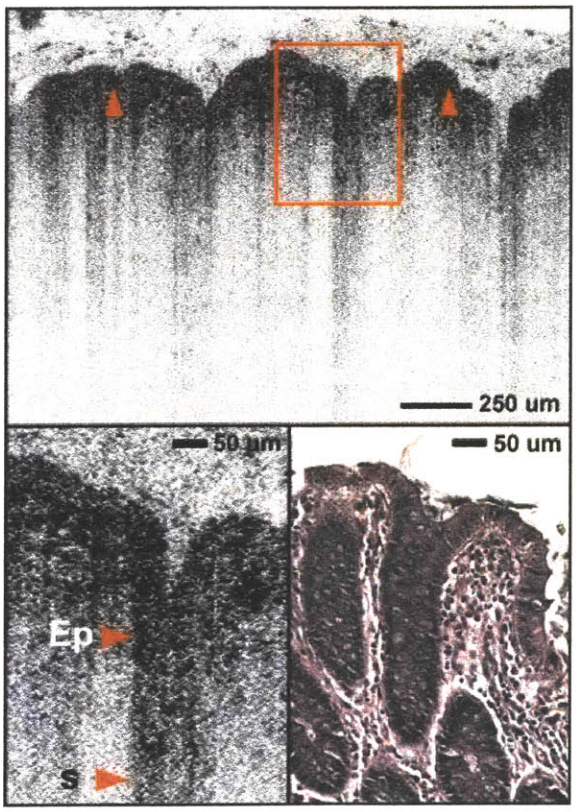

Figure 5.10: Ultrahigh resolution OCT image of normal colon mucosa acquired at 1.1 µm wavelength with 6 µm transverse resolution. The epithelial layer appeared as a distinct layer approximately 40-50 µm in thickness, delineated from the supporting lamina propria by a thin highly scattering band (arrows). Individual crypts as well as the epithelial layer (Ep) lining crypts were visible. Increased scattering (s) possibly due to multiple-scattering effects was often seen beneath crypt structures. Histology, Hematoxylin and Eosin 100x. (Wavelength 1.09 µm, Resolution 3.5 µm axial x 6 µm transverse)

Figure 5.11 shows a representative OCT image of ulcerative colitis and corresponding histology. OCT images at 1.1 μm wavelength were comparable to 1.3 μm wavelength. A disrupted mucosal surface due to ulceration and erosion of the epithelium and irregular branching glands were visible. Crypt abscesses were also present and visible in some specimens of ulcerative colitis. Areas of increased inflammatory cells as determined by histology correlation also appeared highly scattering.

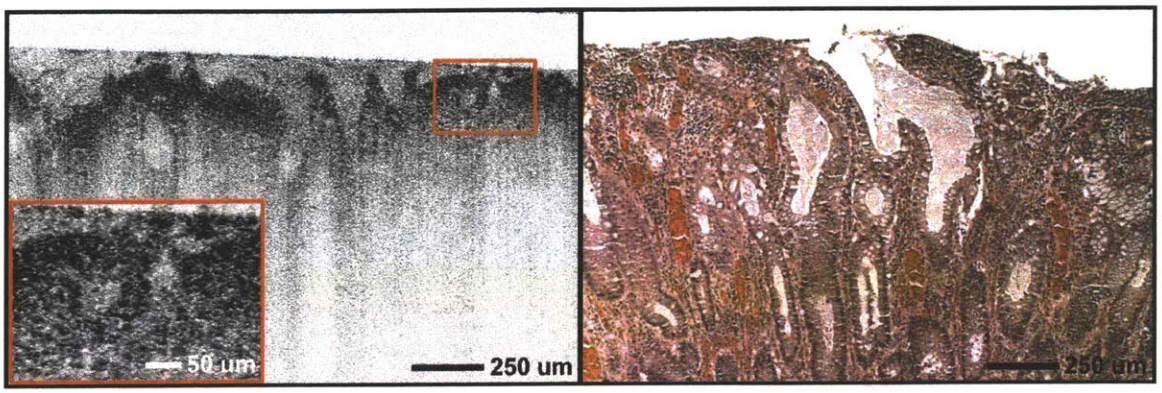

Figure 5.11: Left, Ultrahigh resolution OCT image of ulcerative colitis. A disrupted mucosal surface due to ulceration and erosion and increased scattering due to chronic inflammatory infiltrate was visible. Inset, Magnified view of the mucosal surface. Right, Histology, Hematoxylin and Eosin 40x. (Wavelength 1.09 μm, Resolution 3.5 μm axial x 6 μm transverse)

Figure 5.12 shows an OCT image and corresponding histology of a polypoid adenoma of the colon. The OCT images showed highly irregular glands and regions of high scattering intensity. Individual cells were not visible, but increased scattering at the basal boundary was suggestive of higher numbers and crowding of nuclei.

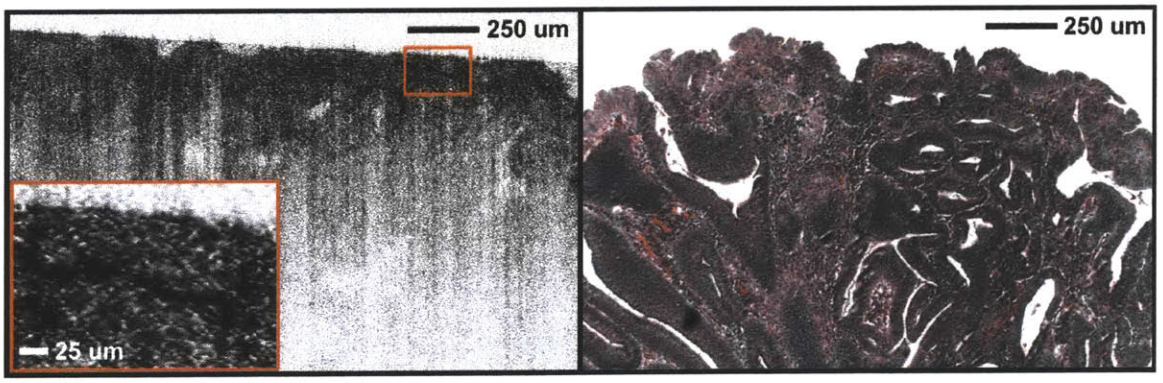

Figure 5.12: Left, Ultrahigh resolution OCT image of a polypoid adenoma of the colon. Highly irregular glands and regions of high scattering intensity were observed. Inset, Magnified view of the OCT image. Individual cells were not visible, but increased scattering at the basal boundary was suggestive of higher numbers and crowding of nuclei. Right, Histology, Hematoxylin and Eosin 40x. (Wavelength 1.09 μm, Resolution 3.5 μm axial x 6 μm transverse)

Figures 13 and 14 show representative 3D OCT volume renderings of normal colon and a polypoid adenoma of the colon, respectively. Rendered 3D OCT data can be viewed from a

virtual surface perspective, yielding a view similar to that of magnification endoscopy. 3D OCT data can also provide a subsurface view. In normal mucosa, crypts were sometimes difficult to identify within individual cross-sectional OCT images. However using 3D OCT, crypts can be visualized based on their shape and distribution in the *en face* plane. Folds in the epithelium which can appear similar to crypts in an individual cross-sectional OCT image can be readily identified and differentiated from crypts in 3D OCT. Comparison of the 3D OCT rendering of normal colon versus polypoid adenoma shows striking differences in both the surface views as well as the cutaway views. Normal colon exhibits a well organized distribution of crypts which are uniform in size and spacing in the *en face* plane. In contrast, polypoid adenoma exhibits irregular glandular structure. Sequential rendered *en face* views at different depths beneath the surface of normal colon and polypoid adenoma can also be generated (Figures 15 and 16). Note that crypts have increased light transmission artifacts at deeper depths. Videos showing sequential *en face* slices through normal colon mucosa and polypoid adenoma are available in the supplementary materials.

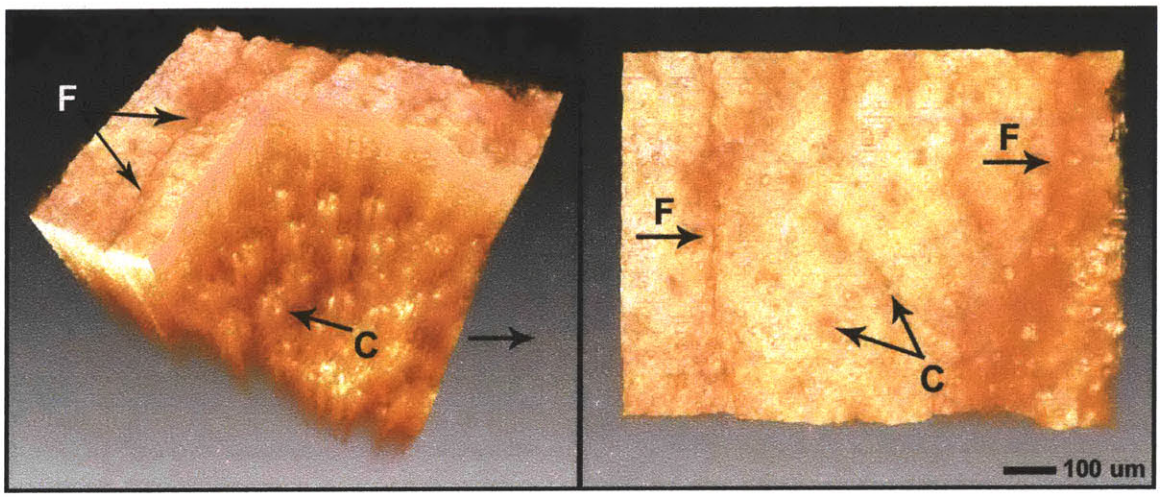

Figure 5.13: Volume rendering of normal colon mucosa: Left, Rendered cutaway view showing individual crypts (C) and folds (F) in the *en face* plane. Right, *En face* view of the surface of the colon mucosa. Folds in the mucosa could be clearly distinguished from crypts. Distinctive surface pit patterns in normal mucosa could be seen. The rendered volume is approximately 1 mm x 1.2 mm x 1.3 mm in dimension and consists of 330 transverse slices. (Wavelength 1.09 μm, Resolution 3.5 μm axial x 6 μm transverse)

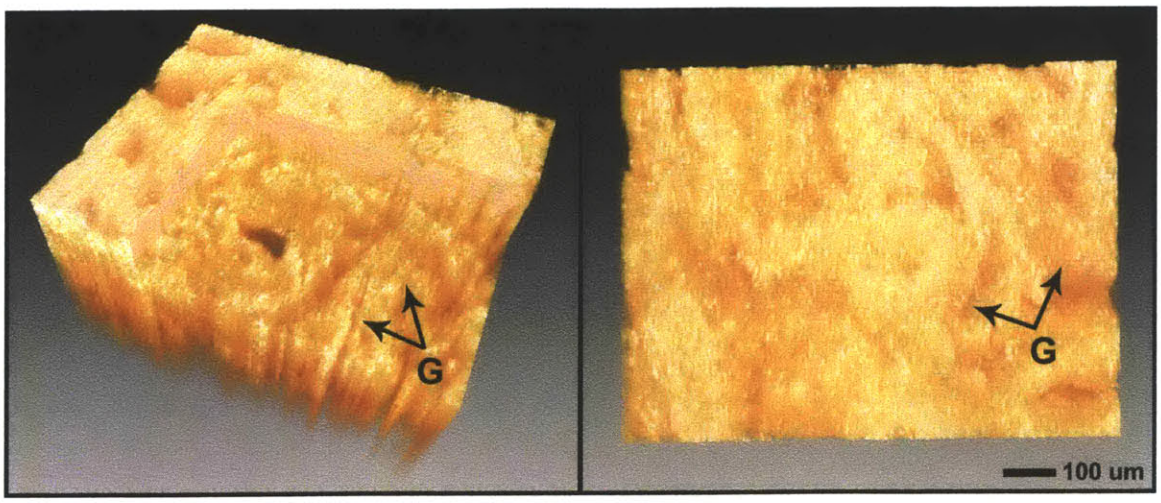

Figure 5.14: Volume rendering of a polypoid adenoma of the colon. Left, Rendered cutaway view shows irregular glandular structures in adenoma (G, arrows) which were distinct from the uniform crypt distribution in normal colon mucosa in Figure 5.13. Right, *En face* view of the surface of the adenoma. Both the surface pattern and subsurface architecture were distinct from that of normal colon mucosa. The rendered volume is approximately 1 mm x 1.2 mm x 1.3 mm in dimension and consists of 275 transverse slices. (Wavelength 1.09 µm, Resolution 3.5 µm axial x 6 µm transverse)

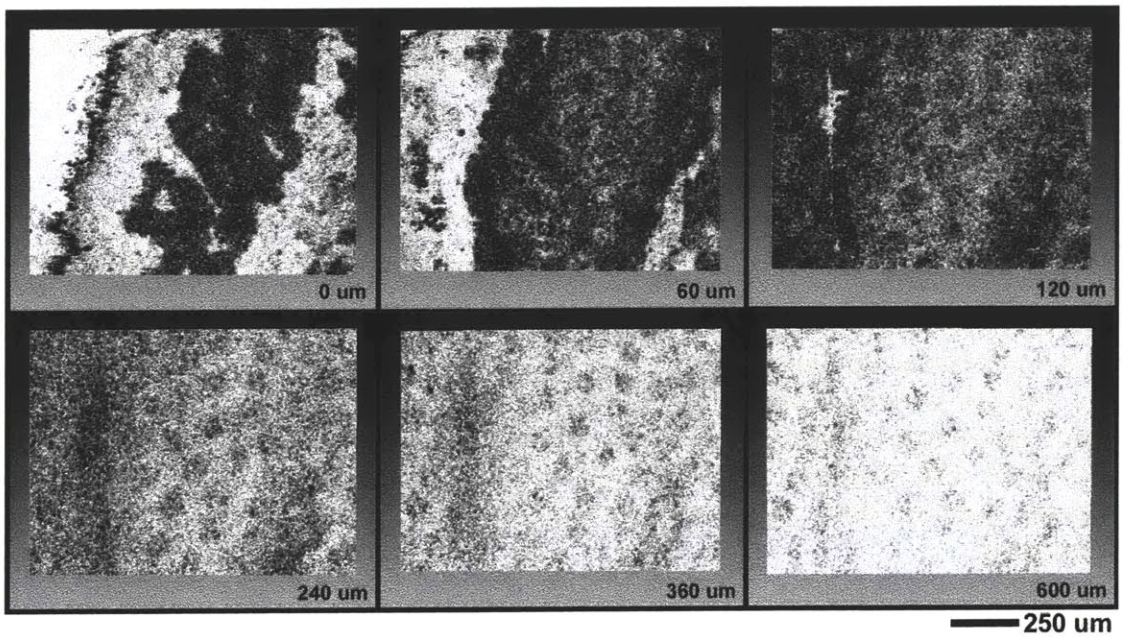

Figure 5.15: 3D imaging enables sequential rendered *en face* views at different depths beneath the surface of normal colon mucosa. Crypts can be visualized based on their shape and distribution in the *en face* plane. Folds in the epithelium which can appear similar to crypts in an individual cross-sectional OCT image can be readily identified and differentiated from crypts in 3D OCT. The rendered image consists of 330 transverse slices. Movies showing sequential en face slices are available in the supplemental materials. (Wavelength 1.09 µm, Resolution 3.5 µm axial x 6 µm transverse)

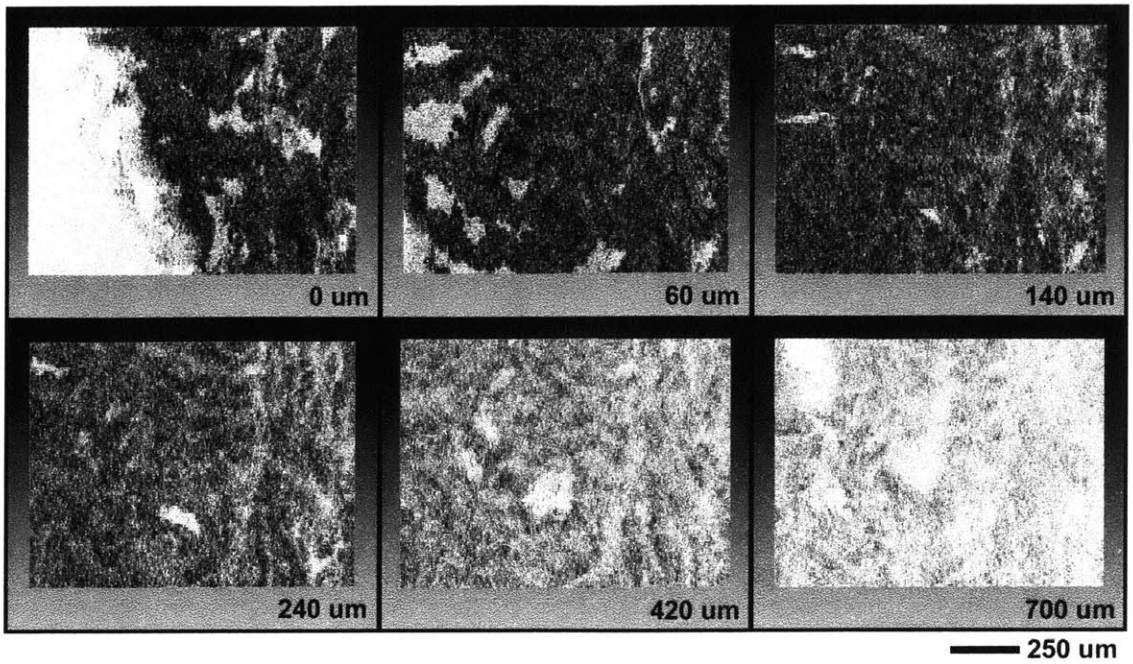

Figure 5.16: Sequential rendered *en face* views at different depths beneath the surface of a polypoid adenoma of the colon. Irregular glandular structures can be seen in adenoma which were distinct from the uniform crypt distribution in normal colon mucosa. Both the surface pattern and subsurface architecture were distinct from that of normal colon mucosa. The rendered image consists of 275 transverse slices. Movies showing sequential en face slices are available in the supplemental materials. (Wavelength 1.09 µm, Resolution 3.5 µm axial x 6 µm transverse)

DISCUSSION

Optical coherence tomography has been extensively investigated in endoscopic imaging. OCT can image glandular organization of mucosal tissue and has demonstrated high sensitivities and specificities for identifying pathologies such as Barrett's esophagus. Recent results have also suggested the possibility of using OCT to differentiate hyperplastic versus adenomatous polyps, which has implications for detecting dysplasia. However, the definitive identification of subtle structural changes associated with dysplasia and other neoplastic changes remains challenging. All clinical endoscopic imaging studies and virtually all *ex vivo* imaging studies to date have been performed with standard resolution OCT using 10-15 µm axial image resolutions. For these reasons, there has been considerable interest in improving the resolution and performance of OCT imaging.

The application of ultrahigh resolution OCT in other fields such as ophthalmology has yielded dramatic improvements in image quality and improved the ability to visualize internal retinal structure.[127, 148, 155] Ultrahigh resolution endoscopic OCT imaging with 3.7 µm axial resolution has recently been demonstrated *in vivo* in the rabbit esophagus and colon.[154] This study presented here is the highest resolution OCT imaging of human GI pathology that has been performed to date. Performing imaging in the clinical pathology laboratory is more challenging than imaging specimens transported to the research laboratory, but has the important advantage of allowing access to specimens immediately after surgical excision, reducing tissue degradation and significantly improving registration accuracy with histology. Imaging in the pathology

laboratory is also an important step toward developing and validating new technology for future endoscopic studies.

Ultrahigh resolution OCT improves image quality by improving axial imaging resolutions, image sharpness, while also reducing speckle noise. OCT images, like ultrasound images, have speckle which results in a grainy appearance, degrading image quality and making boundaries between structures difficult to resolve.[156] Imaging with a shorter coherence length, broader bandwidth light source yields a finer grain speckle pattern and thereby improves image quality. Imaging with improved transverse resolution also improves image quality by further reducing image degradation due to speckle.

The first part of this ultrahigh resolution OCT imaging study used a Cr:Forsterite laser light source at 1.3 μm wavelength with a 4.5 μm axial image resolution and ~11 μm spot size. Imaging was performed at the same wavelength as previous endoscopic and *ex vivo* studies but with a 2-3x improvement in axial resolution and a 1.5-2x improvement in transverse resolution. Ultrahigh resolution *ex vivo* OCT images had improved image quality compared to standard resolution images in previous *ex vivo* studies.[9, 106-108, 117] Ultrahigh resolution images had improved sharpness, reduced speckle and comparable imaging depths compared to standard resolution images. The epithelial layer as well as the crypt structure and organization could be imaged, but the overall improvement in image quality in this *ex vivo* imaging study was not as dramatic as expected.

The second part of this ultrahigh resolution OCT imaging study used a Nd:Glass laser light source at 1.1 μm wavelengths with a 3.5 μm axial image resolution and ~6 μm spot size. This study is of interest because compact and turnkey Nd:Glass laser light sources are commercially available at this wavelength. Compact, high performance, fiber laser light sources at this wavelength are also rapidly becoming available.[157] It is therefore likely that future clinical endoscopic imaging studies will be at this wavelength.

The second OCT system at 1.1 μm wavelength used a smaller 6 μm spot size which improved the ability to visualize mucosal microstructure. Epithelial layers and glandular structure were visualized better than at 1.3 μm wavelength using a 11 μm spot size. However, achieving 6 μm spot sizes required high numerical aperture focusing which resulted in decreased the depth of field. Visualization of the epithelial layer was possible only up to depths of 200-250 μm, sufficient for assessing the upper 2/3 of the mucosa. The limited depths of field may be overcome in the future by using focus tracking methods.[86, 130, 158] The spot sizes used in this study are achievable using standard micro-optics and could be incorporated into endoscopic OCT systems. Further resolution improvement may be possible with microscopy techniques, which will become available in the future for endoscopic applications.[117, 159, 160]

In the studies at both 1.3 μm and 1.1 μm wavelengths, carcinoma and adenoma showed clear loss of normal mucosal organization and increased backscattering in the epithelial layer, which may be the result of nuclear crowding and enlarged nuclei. The presence of inflammatory infiltrate may also contribute to increased scattering.

The third part of the study demonstrated ultrahigh resolution 3D OCT imaging. This is the first demonstration of ultrahigh resolution 3D OCT for GI pathology. 3D imaging and volume rendering provided complementary information to cross-sectional OCT images, enabling visualization of arbitrary planes and rendering of surface topography as well as subsurface tissue microstructure. The ability to visualize *en face* planes at different depths enables glandular organization to be assessed in a way not possible using individual OCT images.

Pervious studies of optical coherence microscopy (OCM) have demonstrated the value of *en face* visualization.[117] Recent work using high-magnification chromoscopic colonoscopy has shown that classification of the colorectal pit pattern in flat and depressed lesions has high sensitivity and specificity for differentiating neoplastic from non-neoplastic lesions, and could potentially be used for assessing suitability for endoscopic mucosal resection.[76, 161-164] 3D OCT can provide additional information on subsurface architectural morphology which is not available with high-magnification endoscopy and thus might be a valuable tool in future endoscopic studies.

Acquisition of 3D OCT data is possible in the *ex vivo* setting because motion artifacts are absent. However, with recent advances in OCT imaging technology using spectral/Fourier domain detection, dramatic improvements in imaging speed are possible.[165-167] Results in ophthalmic imaging have achieved ~100x improvements in imaging speeds.[168-171] These high imaging speeds make 3D OCT feasible *in vivo*. In addition to high speed imaging, novel scanning devices such as micromechanical mirror or piezoelectric fiber scanners have also been recently developed.[172-175] These advances promise to enable 3D OCT endoscopic imaging in the future.

CONCLUSION

In conclusion, this chapter demonstrated ultrahigh resolution OCT imaging of GI pathology in the large and small intestine and correlation with histology. Performing the study in the pathology laboratory setting enabled rapid access to tissue specimens, reducing degradation effects and enabling accurate registration of OCT imaging with histology. Imaging at 1.3 μm wavelengths with a 4.5 μm axial image resolution and 11 μm spot size was first performed to investigate the effect of improved axial resolution at standard OCT wavelengths. Studies were also performed at 1.1 μm wavelengths with a 3.5 μm axial image resolution and 6 μm spot size. These studies are important because high performance lasers are commercially available at this wavelength. Ultrahigh resolution imaging demonstrated clear delineation of the epithelium from the lamina propria and visualization of individual crypts and glandular structure, but individual cells were not visible. Decreasing the transverse spot size improved transverse image resolution, but resulted in decreased depth of field. Image quality was improved compared to previous *ex vivo* imaging studies, but was not as dramatic as expected. Recent studies of ultrahigh resolution endoscopic OCT imaging in animals have shown excellent image quality *in vivo*.[154] It is possible that even with rapid access to specimens provided by this study, imaging in *ex vivo* specimens may have lower contrast and sharpness than *in vivo* imaging. Further investigations using ultrahigh resolution imaging in clinical endoscopic studies will be necessary to evaluate the impact of improved resolution. Three-dimensional OCT imaging was demonstrated and enables improved differentiation of *en face* and three-dimensional structure of glandular organization. These studies can be used as a baseline for development of new OCT technology and could aid the interpretation of future ultrahigh resolution endoscopic imaging studies.

Chapter 6

Ultrahigh Resolution and Three-Dimensional OCT Imaging of Benign and Malignant Lesions in the Human Breast

INTRODUCTION

Breast cancer is a common and lethal disease. Approximately 215,990 new cases of invasive breast cancer are expected to occur among women in the United States in 2004, accounting for 32% of all cancer cases in women. An estimated 40,110 deaths are expected from breast cancer in 2004, making breast cancer the leading cause of cancer deaths in women after lung cancer. In addition to invasive breast cancer, an estimated 59,390 new cases of *in situ* cancer are expected to occur in women in 2004. [2] This translates to roughly a 1 in 8 chance for women of developing invasive breast cancer in their lifetime.

Despite these high incidence rates, breast cancer mortality has declined by 2.5% per year in the last decade due to both earlier detection and improved treatment methods. Early detection increases treatment options and saves lives. The 5-year survival rate for local cancer is 97%. However, this survival rate decreases dramatically to 79% if the cancer has spread regionally and to 23% for distant metastasis. Survival is also stage-dependent, with early stage disease correlated to best survival.[2] Currently 63% of breast cancers are diagnosed at a localized stage, which is attributed to effective use of mammography for screening as well as awareness of breast cancer symptoms in the population.[18]

The fact that a significant percentage of early cancers are missed suggests that early detection methods can still be improved. Sampling error is generally recognized as a major issue of fine-needle aspiration cytology (FNAC), the standard method for obtaining breast samples for diagnosis of palpable breast lesions.[176, 177] Core-needle biopsy (CNBx) has come into more widespread use for both palpable and non-palpable lesions due to the introduction of new more sensitive spring-loaded biopsy "guns,"[178] but still suffer from false-negative rates associated with sampling error.[179] With increased use of image guidance, higher sampling success rates have been achieved,[179, 180] but improvements are limited to lesions which are visible on ultrasound or mammography, which have limited resolutions and therefore cannot adequately identify small lesions or localize the full extent of lesions. In addition to the sampling limitations of diagnostic techniques, surgical methods for cancer treatment critically depend on accurate methods for assessment of microscopic resection margins. Women with negative excision margins have low

rates of local recurrence following lumpectomy and radiation therapy, while positive resection margins are associated with greater risk of recurrence.[181-183] However, methods such as intraoperative frozen section analysis, which enables rapid histologic assessment of margins in the operating suite, are time- and labor-intensive and may lead to inadequate assessment of large specimens and loss of diagnostic material in small specimens.[184] Newer methods such as radioguided surgery [185, 186] have recently emerged as a method for resection guidance, with the potential for more accurate and less unnecessary surgery. A technique capable of performing subsurface, three-dimensional, micrometer-scale imaging in real time could permit guidance of biopsy procedures to reduce sampling errors and intraoperative monitoring of biopsy and surgical procedures, offering immediate information to the clinician and likely improving patient outcome.

OPTICAL COHERENCE TOMOGRAPHY

OCT has a number of advantages which may make it a useful adjunct to current diagnostic imaging modalities for breast cancer. OCT has higher resolution than any currently available imaging technique used in breast cancer management. OCT can be incorporated into a wide variety of endoscopic and laparoscopic imaging devices and can be used to guide open-field surgical procedures.[51, 52, 110, 135, 187, 188] Optical imaging needles have also been developed.[53] An OCT imaging needle could potentially be incorporated into core-biopsy devices to enable a less-invasive "first-look" at a tissue specimen. Imaging could be performed over a greater overall sampling volume than obtained by typical core-biopsy samples, reducing sampling error and trauma associated with multiple invasive core-biopsy procedures. OCT imaging catheters could also be used to assess the epithelial lining of the mammary duct system, in a manner similar to mammary ductoscopy.[189] While ductoscopy provides only surface information, OCT could provide real-time cross-sectional imaging of epithelial microstructure relevant for assessing intraductal lesions.

To date, OCT has not been reported for imaging benign and malignant lesions of the human breast. The role of OCT for research and image-guided surgery for breast cancer has recently been shown *ex vivo* in the carcinogen-induced rat mammary tumor model.[190] In the reported study, ultrahigh resolution OCT imaging of normal fibroadipose tissue, early-stage ductal cancer, and infiltrative cancer in the rat mammary gland was presented. Three-dimensional rendering demonstrated that tumor margins could be identified. Imaging results in the rat model suggested that tumor cells exhibit increased scattering relative to the surrounding stroma.

This chapter investigates the feasibility of new ultrahigh resolution OCT technology for imaging normal and neoplastic lesions of the human breast. In this study, normal, benign, and malignant breast lesions were imaged *ex vivo* and correlated with histology. Imaging was performed using a portable, ultrahigh resolution OCT system in the clinical pathology laboratory. Imaging in the pathology laboratory allows rapid access to surgical specimens, reducing possible artifacts from tissue degradation. Imaging in the pathology laboratory also provides access to diagnostically critical specimens, such as lymph nodes, which are sensitive to removal from the hospital setting. *Ex vivo* imaging also allows image registration to be carefully controlled to enable accurate correlation of OCT images with histology.

In this study, ultrahigh resolution OCT imaging was performed at ~1.1 μm wavelength with a 3.5 μm axial resolution and 6 μm spot size using a Nd:Glass laser light source. The Nd:Glass laser has the important advantage of being compact and commercially available and is therefore suitable for future clinical imaging studies. This system performs imaging at wavelengths shorter than the wavelength typically used in clinical OCT systems, but which enable higher axial resolutions to be achieved. The transverse spot size was also chosen to be small in order to improve transverse resolution over that used in standard resolution OCT systems. Three-dimensional OCT imaging was also performed to investigate the utility of 3D visualization of breast architectural morphology.

METHODS

Imaging studies were performed on freshly excised surgical specimens in the pathology laboratory of the Beth Israel Deaconess Medical Center. These studies were approved by the Institutional Review Board (IRB) at the Beth Israel Deaconess Medical Center and the Committee for the Use of Humans as Experimental Subjects (COUHES) at the Massachusetts Institute of Technology. Informed consent was not required since the study involved only database review and *ex vivo* surgical specimens. Fresh specimens were selected based on the presence of pathology upon gross examination, prompt arrival in the pathology laboratory, and large specimen size, allowing normal and pathologic tissue to be collected from each specimen for the study without interfering with routine diagnostic procedures. In selected cases, specimens used for clinical diagnostic purposes were imaged immediately prior to placement in cassettes for standard processing. All specimens available during the duration of the study which met these criteria were imaged. For selected specimens with suspicion of *in situ* pathology, additional mammography was performed on the excised specimens to guide OCT imaging to areas of microcalcifications which have increased likelihood of pathology.

Ultrahigh Resolution OCT System and Imaging Parameters

The physical principles of OCT have been described previously.[3, 4] Ultrahigh resolution OCT imaging was performed with 3.5 μm axial resolution in tissue using a femtosecond Nd:Glass laser light source at a center wavelength of 1090 nm.[96] This laser is commercially available (High Q Laser Productions, Hohenems, Austria) and is compact, robust, and turn-key, making it suitable for future *in vivo* clinical studies. Although shorter wavelengths are attenuated more rapidly by tissue scattering, they enable finer axial resolutions for a given bandwidth as well as smaller spot sizes. The transverse spot size was set to be ~6 μm (FWHM) to examine the effects of improved transverse resolution. This transverse spot size is a factor of 3-4x finer than endoscopic OCT systems used in investigations of the gastrointestinal tract. The depth of field was calculated to be ~140 μm. OCT imaging was performed using post objective scanning in order to avoid aberrations and preserve the small spot size.

Three-dimensional OCT imaging was also performed. Three-dimensional data sets consisting of 200 to 350 individual OCT images spaced by 3 μm to 5 μm apart were generated by raster scanning the beam. A 5 μm spacing was chosen for specimens with large architectural features and a 3 μm spacing was used for all other specimens. Each OCT image in the raster scan consisted of 600-1800 transverse pixels over 1-2 mm. This resulted in an axial scan spacing of

0.6-3 μm by 3-5 μm. The 3D OCT data was processed and visualized using MRI software for 3D visualization and volume modeling (Amira, Mercury Computer Systems, Berlin).

Specimen Selection

Thirty-five cases from adult patients, consisting of a total of 142 separate specimens, were each imaged within several hours of excision. Fresh specimens were selected based on the presence of pathology upon radiographic findings or gross examination, prompt arrival in the pathology laboratory, and large specimen size, allowing normal and pathologic tissue to be collected for the study without interfering with routine diagnostic procedures. In selected cases, specimens used for clinical diagnostic purposes were imaged immediately prior to placement in cassettes for standard processing. For selected specimens with suspicion of *in situ* pathology, additional mammography was performed on the excised specimens to guide OCT imaging to areas of microcalcifications which have increased likelihood of pathology.

Collected specimens consisted of both normal and pathologic sites from each case. Benign breast tissue imaged consisted of fibroadipose tissue including mammary ducts and lobules (n = 37), fibrocystic changes (n = 8), fibroadenoma (n = 7), ductal hyperplasia (n = 6), and isolated cases of lipoma and neurofibroma. Malignant lesions imaged included ductal carcinoma-in-situ (DCIS, n = 6), infiltrating ductal carcinoma (n = 12), infiltrating lobular carcinoma (n = 8), and infiltrating carcinoma with ductal and lobular features (n = 5). Three infiltrating ductal carcinoma specimens included regions of DCIS. Nine specimens of DCIS or cancer included microcalcifications. Regions consisting of biopsy site changes (n = 23), fat necrosis (n = 3), and fibrosis/scarring (n = 2) were also imaged. In addition to grossly normal and abnormal breast lesions, lymph nodes specimens (n = 23, 5 positive, 18 negative) were imaged.

Imaging and Registration

Since the OCT light was in the near infrared and invisible to the eye, image registration was performed with a visible green guiding beam which was coincident with the OCT imaging beam. Imaging was performed without contact to the tissue. All images were scaled in the axial direction by 1.38x to correct for the approximate index of refraction of tissue.[102] When necessary, specimens were irrigated (RPMI 1640) to prevent dehydration during imaging. Specimens were marked at the beginning and end of each OCT scan with microinjections of ink to designate the imaging plane orientation. After imaging and inking, specimens were immersed in Bouin's fixative for 2 seconds to fix the ink and prevent smearing. Specimens were then placed in 10% buffered formalin, routinely processed and paraffin embedded. Multiple 5 μm thick tissue sections were obtained from the OCT imaging plane and stained with Hematoxylin and Eosin. OCT images and corresponding histology sections were compared. Minor discrepancies between histology and OCT images can be attributed to tissue fixation, processing and sectioning artifacts.

RESULTS

OCT images and histology photomicrographs at 40x to 100x magnification are shown with corresponding size scale bars. Histology is scaled with the same magnification as the OCT

image. Ultrahigh resolution OCT imaging was performed at 1.1 µm wavelengths with 3.5 µm axial resolution and ~6 µm spot size. This represents an ~1.5x coarser axial resolution and a ~2x finer transverse resolution than the previous *ex vivo* study performed in the rat model of induced breast carcinogenesis.[190] These studies use a Nd:Glass laser source which operates at a center wavelength longer than the 800 nm wavelengths used in previous studies. However, imaging at longer wavelengths permit increased penetration depth and lasers at this wavelength are more readily available and suitable for future clinical use.

Normal

Imaging of normal breast tissue produced distinct images of fibrous stroma and adipose tissue characteristic of normal breast. Figure 6.1 shows an ultrahigh resolution OCT image of normal fibroadipose tissue and corresponding histology. Normal fibrous stroma appears heterogeneous and highly scattering and can clearly be distinguished from surrounding adipose tissue. Adipocytes appeared round or oval in shape, with individual well-circumscribed cell borders. Adipose tissue exhibited decreased signal attenuation relative to the surrounding tissue at the same depth. Consequently, regions directly beneath individual adipocytes appear to have higher signal intensity than equivalent regions at the same depth.

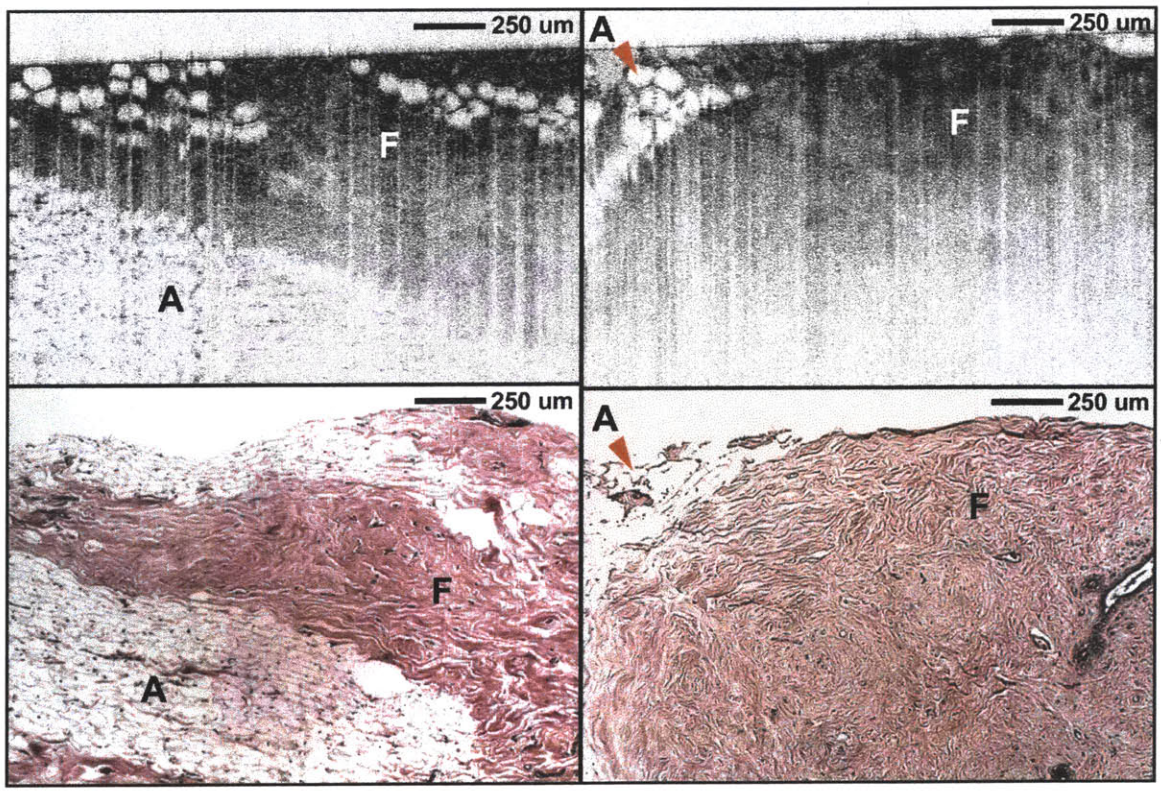

Figure 6.1: OCT images of normal fibroadipose tissue. Fibrous stroma (F) appears heterogeneous and highly scattering while individual adipocytes (A) appear low scattering, with individual well-circumscribed scattering borders. Top, OCT; Bottom, Histology, Hematoxylin and Eosin 40x. (Wavelength 1.09 µm, Resolution 3.5 µm axial x 6 µm transverse)

A second OCT image with a magnified view of normal fibrous tissue is shown in Figure 6.2. Fibrous stroma exhibits variations in scattering intensity which appear to correspond to local variations in collagen fiber density.

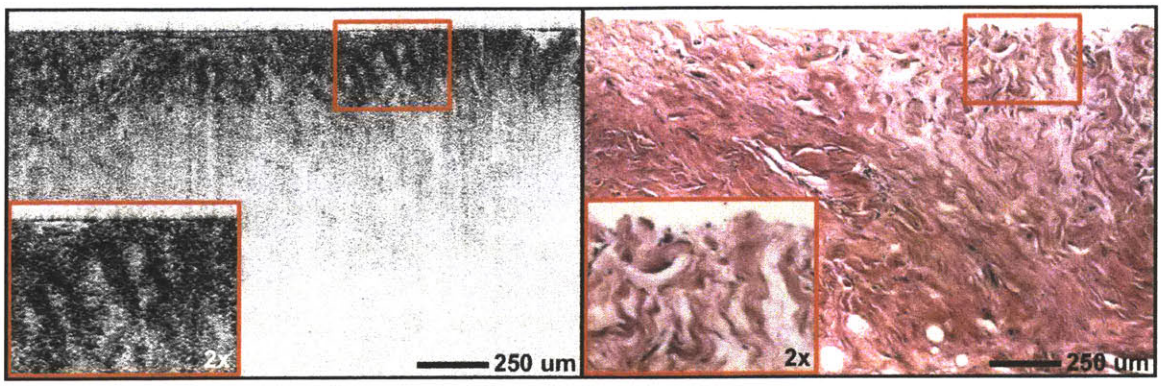

Figure 6.2: OCT image of normal fibrous stroma. Insets show magnified regions of high scattering corresponding to fibrous bundles. Left, OCT; Right, Histology, Hematoxylin and Eosin 40x and 100x. (Wavelength 1.09 μm, Resolution 3.5 μm axial x 6 μm transverse)

Figure 6.3 and 6.4 shows ultrahigh resolution OCT images of a normal lobule of glands and a terminal lobular duct unit, respectively. Normal glands were visible as round structures up to 100 μm in cross-section. Individual glands appeared less scattering than the surrounding fibrous stroma and intervening intralobular stroma, and were clearly distinguishable from adipocytes.

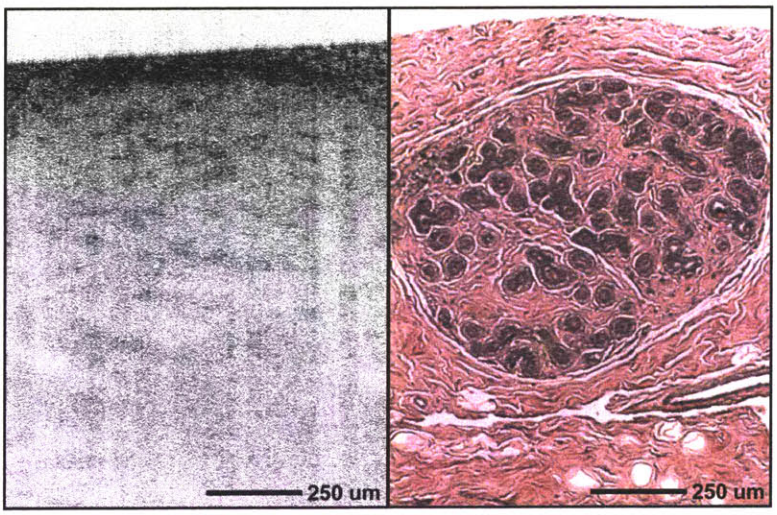

Figure 6.3: OCT image of normal lobule of glands. Individual glands appeared low scattering within higher scattering intralobular stroma. Left, OCT; Right, Histology, Hematoxylin and Eosin 40x. (Wavelength 1.09 μm, Resolution 3.5 μm axial x 6 μm transverse)

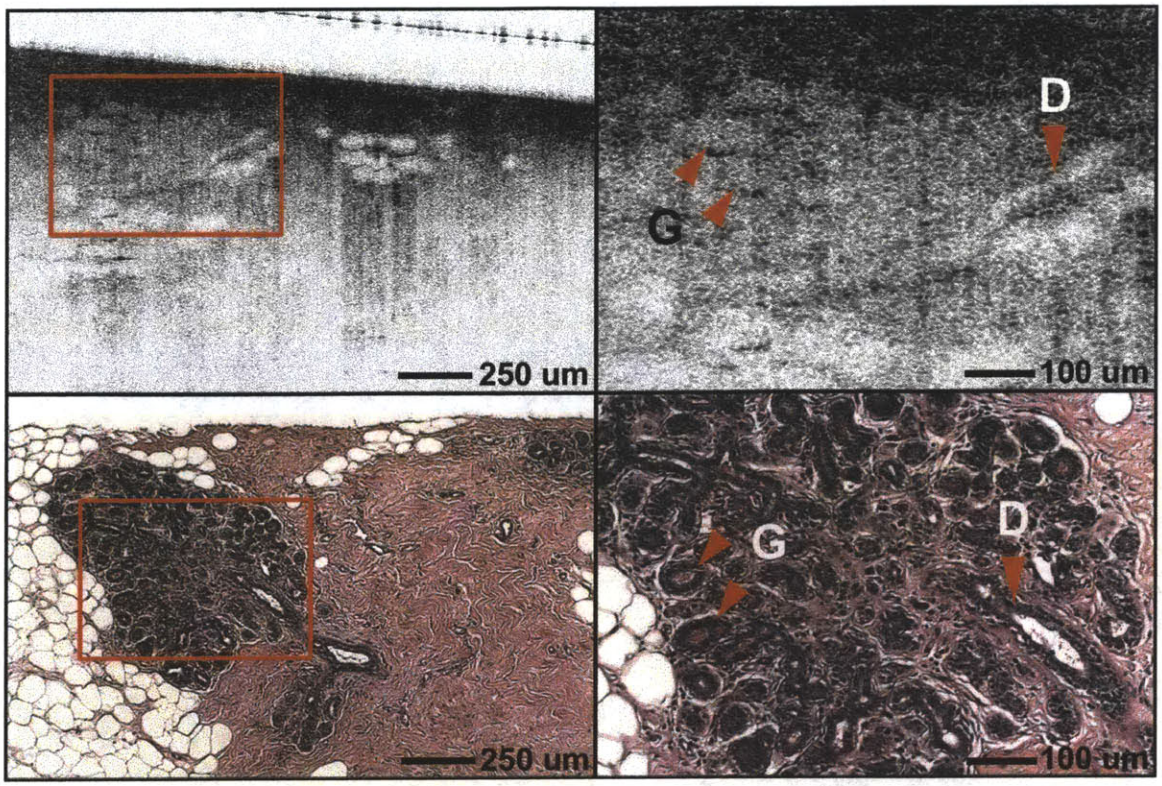

Figure 6.4: OCT images of a terminal duct lobular unit. Magnified image of the lobule (right) shows individual glands (G) as elliptical regions of lower scattering. A duct (D) is clearly visible to the right of the lobule. Top, OCT; Bottom, Histology, Hematoxylin and Eosin 40x and 100x. (Wavelength 1.09 µm, Resolution 3.5 µm axial x 6 µm transverse)

However, contrast between glandular structures and fibrous stroma was sometimes low, making conclusive determination of the size, shape, and extent of individual glandular structures difficult. Sequential images separated by 120 µm acquired in cross-section (Figure 6.5) enabled the lobular duct unit to be identified in OCT images based on three-dimensional lobular structure.

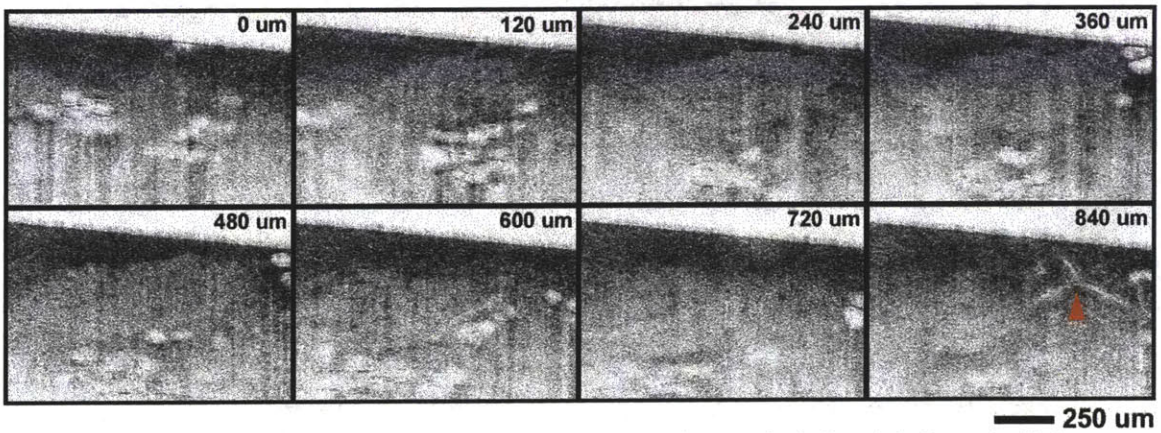

Figure 6.5: Sequence of cross-sectional OCT images of a terminal duct lobular unit. Volume imaging enables three-dimensional tissue structure to be visualized. A duct network is clearly visible in the last frame (arrow). Images are spaced by 120 µm between frames. (Wavelength 1.09 µm, Resolution 3.5 µm axial x 6 µm transverse)

Ultrahigh resolution OCT images of a normal lactiferous duct are shown in Figure 6.6. The ductal epithelium was visible as a lower scattering layer lining the duct, and was lower scattering than the surrounding fibrous stroma. Duct lumens were visible in ducts larger than ~50 μm in diameter, and the basal boundary between the myoepithelial layer and stroma could be distinguished. Ducts of different diameters appeared similar in architecture and could be distinguished by their continuous and branching structure. Ducts with diameters as small as 20-25 μm could be identified based on three-dimensional architecture in sequential transverse OCT images. Smaller ducts appeared similar in cross-section to glands, but could be distinguished based on their continuous structure.

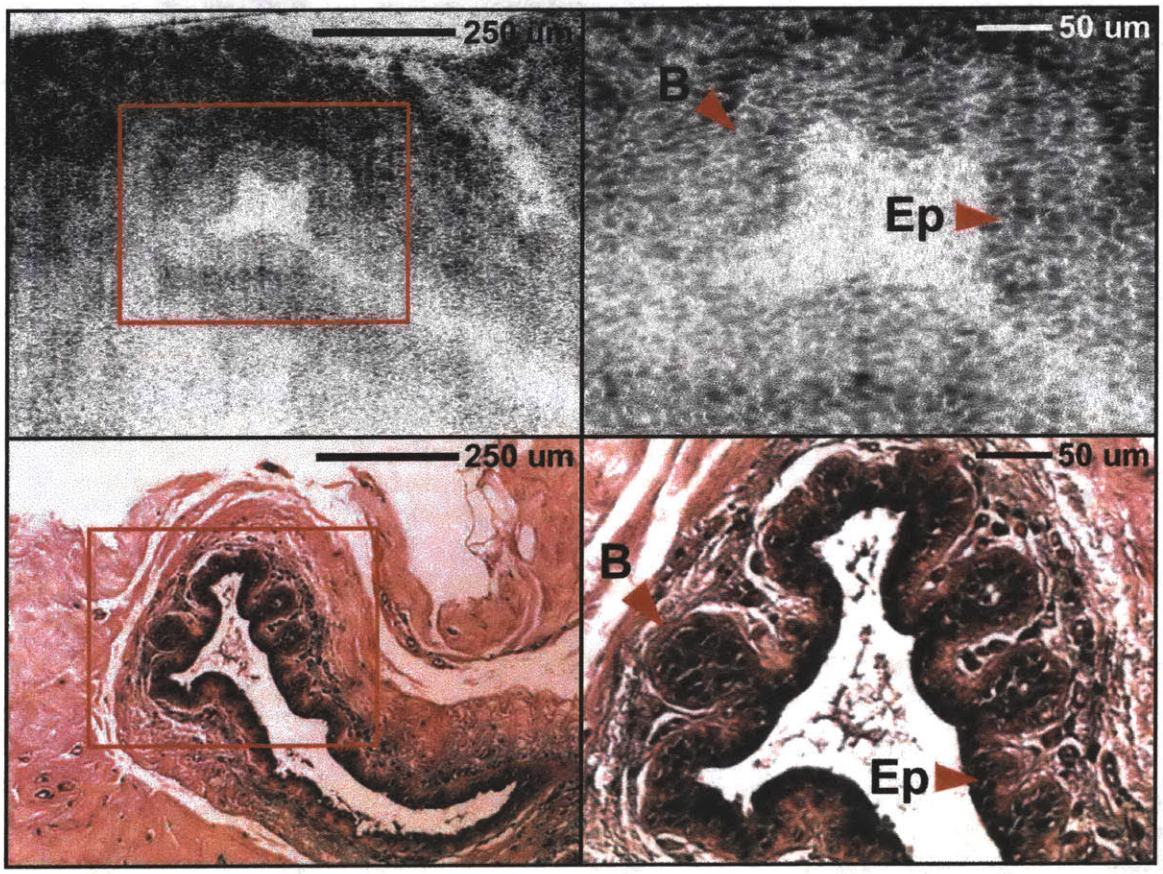

Figure 6.6: OCT images of normal lactiferous duct. Magnified image of the duct (right) shows normal ductal epithelium (Ep) appearing lower scattering than the surrounding fibrous stroma. The basal boundary (B) between the myoepithelium and stroma is visible. Top, OCT; Bottom, Histology, Hematoxylin and Eosin 40x and 100x. (Wavelength 1.09 μm, Resolution 3.5 μm axial x 6 μm transverse)

Figure 6.7 shows an image of normal lymph node imaged through the lymph node capsule with representative histology. OCT was able to identify and image through the extent of the fatty/fibrous capsule, but the body of the node appeared relatively uniformly scattering with no obvious follicular structure. Figure 6.8 shows an image of the node body acquired after the node was bisected for routine histopathology. Imaging through the bisected node identified regions of increased scattering which may correspond to boundaries between germinal centers. Highly

scattering continuous structures within the lymph node were visible which may correspond to lymphatic vessels or the trabecular sinuses. Fatty replacement of normal lymphatic tissue was also visible in OCT images.

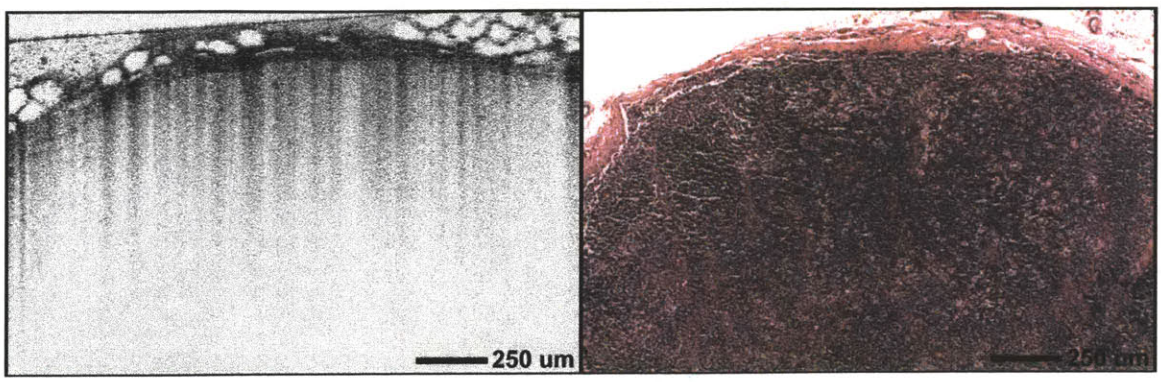

Figure 6.7: OCT image of normal lymph node imaged through capsule. Fibrous tissue of the capsule is visible as a highly scattering band. Left, OCT; Right, Histology, Hematoxylin and Eosin 40x. (Wavelength 1.09 µm, Resolution 3.5 µm axial x 6 µm transverse)

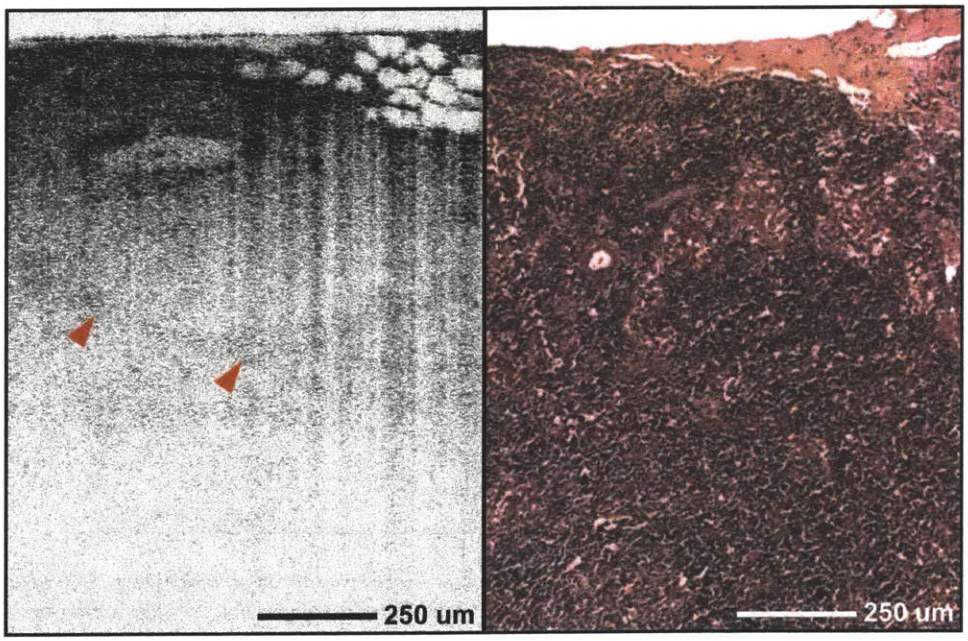

Figure 6.8: OCT image of bisected normal lymph node. Highly scattering continuous structures within the lymph node may correspond to lymphatic vessels or trabecula. Left, OCT; Right, Histology, Hematoxylin and Eosin 40x. (Wavelength 1.09 µm, Resolution 3.5 µm axial x 6 µm transverse)

Figures 6.9 and 6.10 show images of normal lymph node and normal fibrous tissue before and after averaging. Averaging reduces noise due to speckle and improves image quality. Imaging was performed in the same location for ~100 frames. Averaging images of both lymph node and fibrous tissue clearly reduces speckle, but significantly enhanced contrast between internal tissue structures was not observed.

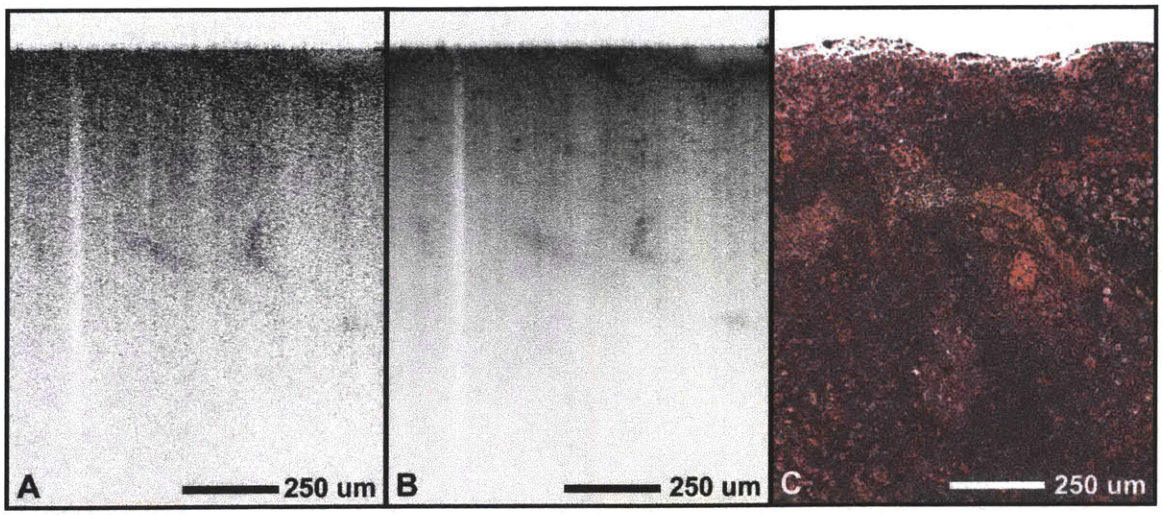

Figure 6.9: OCT image of bisected normal lymph node before and after averaging. A: Single image. B: Average of 99 images at the same location. A, B: OCT; C: Histology, Hematoxylin and Eosin 40x. (Wavelength 1.09 µm, Resolution 3.5 µm axial x 6 µm transverse)

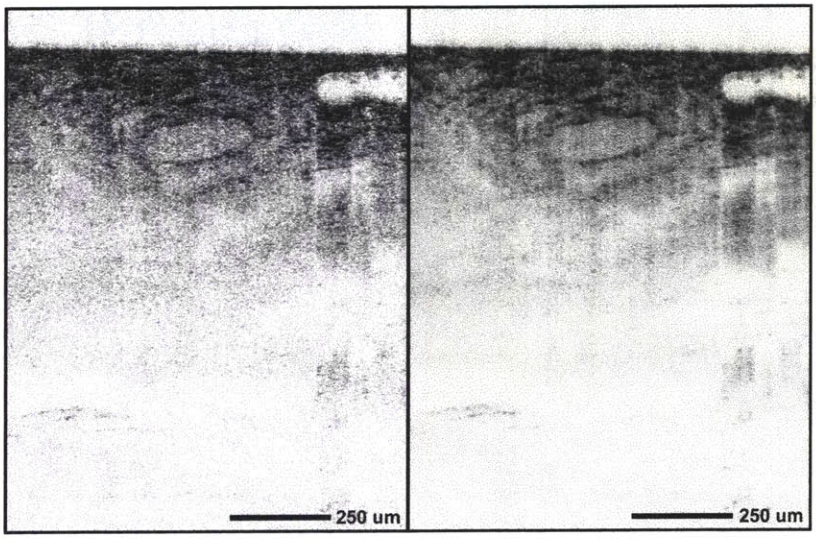

Figure 6.10: OCT image of normal fibroadipose tissue before and after averaging. Left: Single image. Right: Average of 101 images at the same location. (Wavelength 1.09 µm, Resolution 3.5 µm axial x 6 µm transverse)

Benign

Figure 6.11 shows a representative OCT image of fibrocystic changes. Individual cysts within fibrous tissue appeared well-circumscribed and contained scattering material. Epithelium lining cysts was visible as a thin, ~30-40 µm band lining cysts. In contrast, epithelium exhibiting apocrine metaplasia appeared thickened and irregular (Figure 6.12).

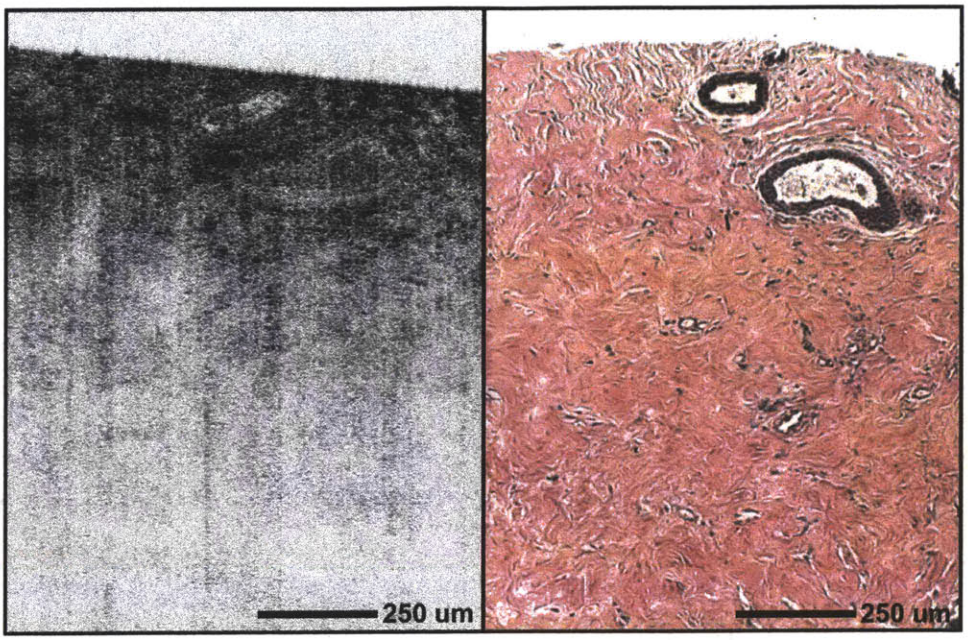

Figure 6.11: OCT image of fibrocystic changes. Individual cysts within fibrous stroma appeared well-circumscribed and irregularly filled with scattering material. Epithelium is occasionally visible as a uniform scattering band lining cysts. Left, OCT; Right, Histology, Hematoxylin and Eosin 40x. (Wavelength 1.09 µm, Resolution 3.5 µm axial x 6 µm transverse)

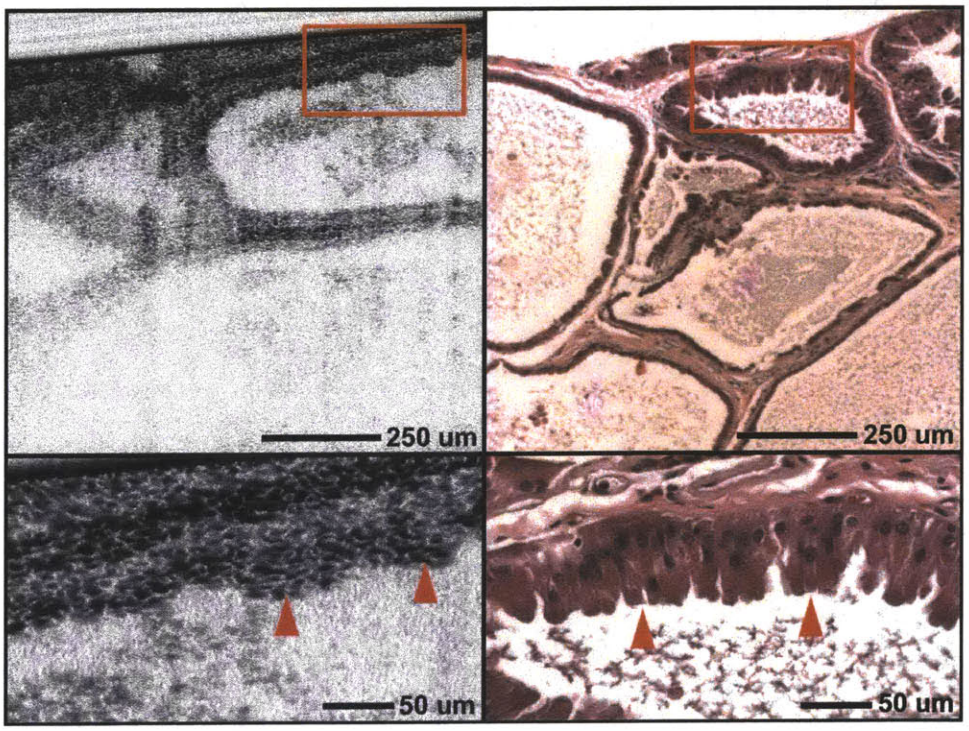

Figure 6.12: OCT images of apocrine metaplasia within cysts. Metaplastic epithelium is visible in the magnified image (bottom) as a thickened irregular band lining cysts (arrows). Left, OCT; Right, Histology, Hematoxylin and Eosin 40x and 100x. (Wavelength 1.09 µm, Resolution 3.5 µm axial x 6 µm transverse)

Figure 6.13 shows OCT image of a benign cyst within breast tissue exhibiting fibrocystic changes. Rare calcium oxalate calcification occasionally present within cysts were visible as focal regions of increased scattering with pronounced shadowing in the OCT images.

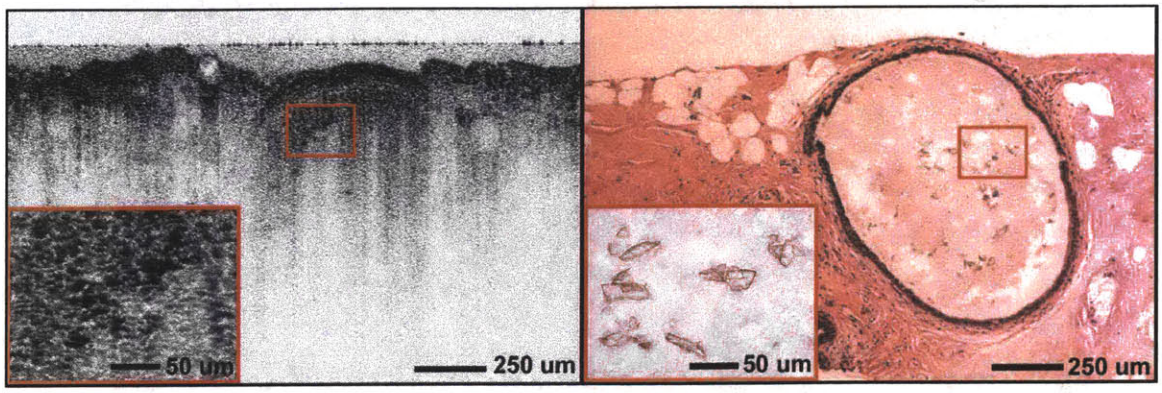

Figure 6.13: OCT image of a large cyst. Insets show calcium oxalate calcifications visible as focal regions of high scattering with pronounced shadowing. Left, OCT; Right, Histology, Hematoxylin and Eosin 40x. (Wavelength 1.09 µm, Resolution 3.5 µm axial x 6 µm transverse)

Figure 6.14 shows a representative OCT image of fibroadenoma. Fibroadenoma specimens imaged appeared more uniformly scattering than the heterogeneous fibrous stroma associated with normal fibroadipose tissue. Regions of high scattering suggestive of boundaries between stromal nodules were observed. Compressed ducts with epithelium were visible as finger-like projections of low scattering.

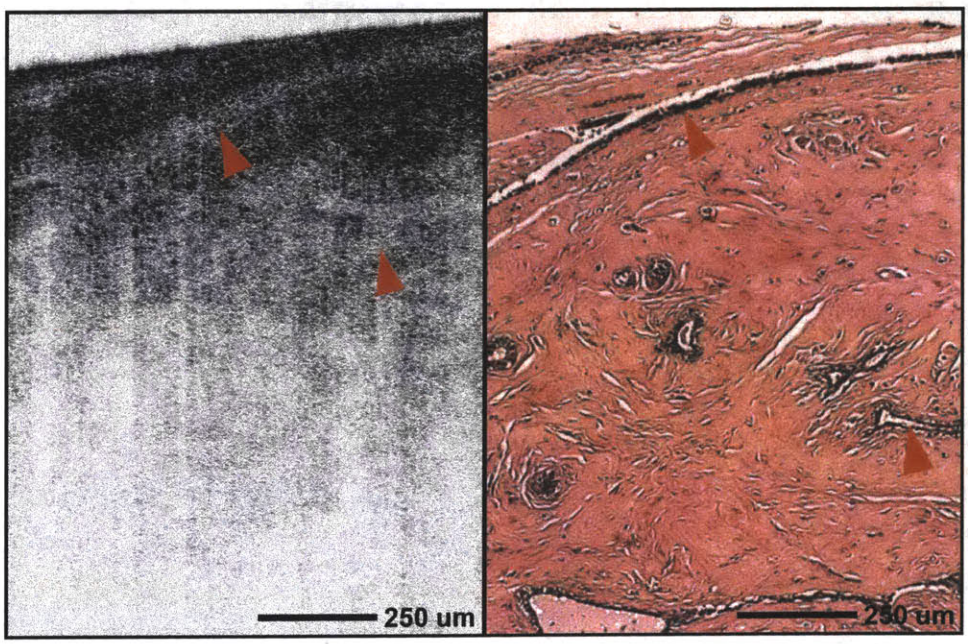

Figure 6.14: OCT image of benign fibroadenoma. Stromal nodules appeared more uniformly scattering than normal fibrous tissue and compressed ducts with epithelial component (arrows) were visible as finger-like regions of low scattering. Left, OCT; Right, Histology, Hematoxylin and Eosin 40x. (Wavelength 1.09 µm, Resolution 3.5 µm axial x 6 µm transverse)

OCT images of benign ductal hyperplasia are shown in Figure 6.15. Highly-scattering finger-like projections into the duct lumen were visible which were distinct from the appearance of normal ducts (Figure 6.6). These projections may correspond to fibrovascular cores projecting into the lumen or boundaries between folds of hyperplastic epithelium within the duct lumen. Sequential images acquired in cross-section allow the architecture of hyperplastic epithelium to be visualized (Figure 6.16).

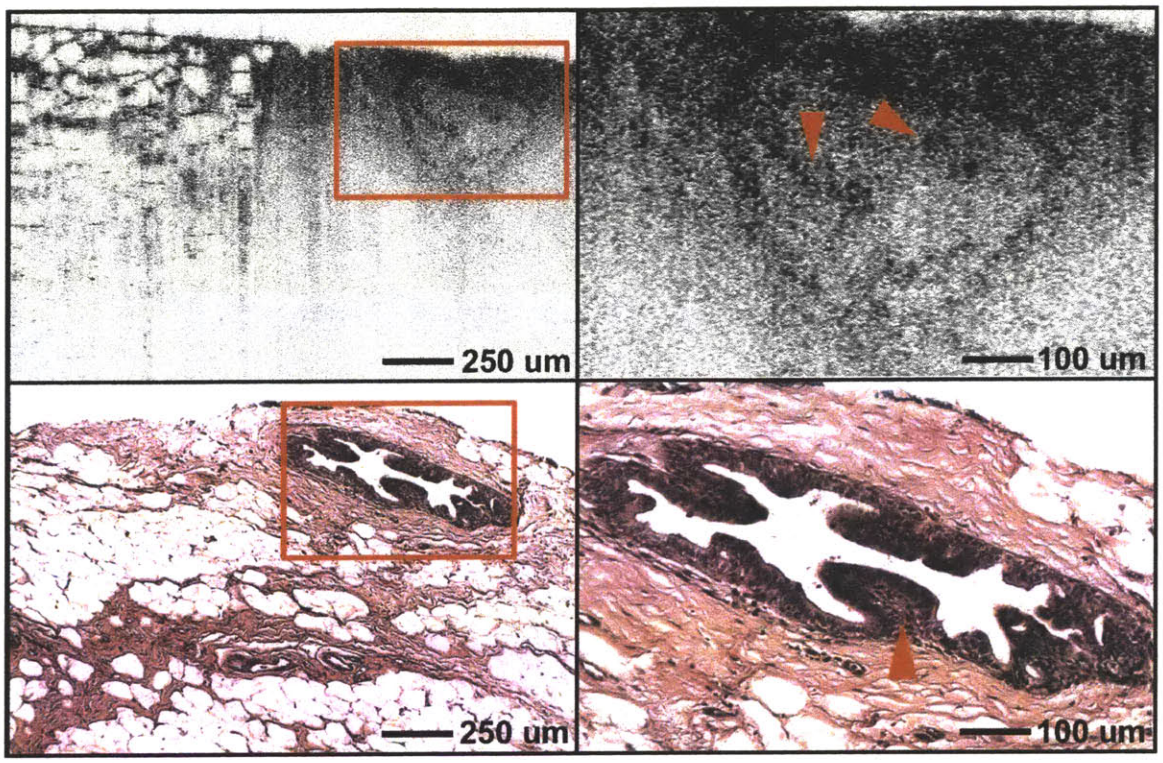

Figure 6.15: OCT images of ductal hyperplasia. Magnification of the duct region (right) shows highly scattering projections into the duct lumen corresponding to hyperplastic epithelium or fibrovascular cores (arrows). Top, OCT; Bottom, Histology, Hematoxylin and Eosin 40x and 100x. (Wavelength 1.09 μm, Resolution 3.5 μm axial x 6 μm transverse)

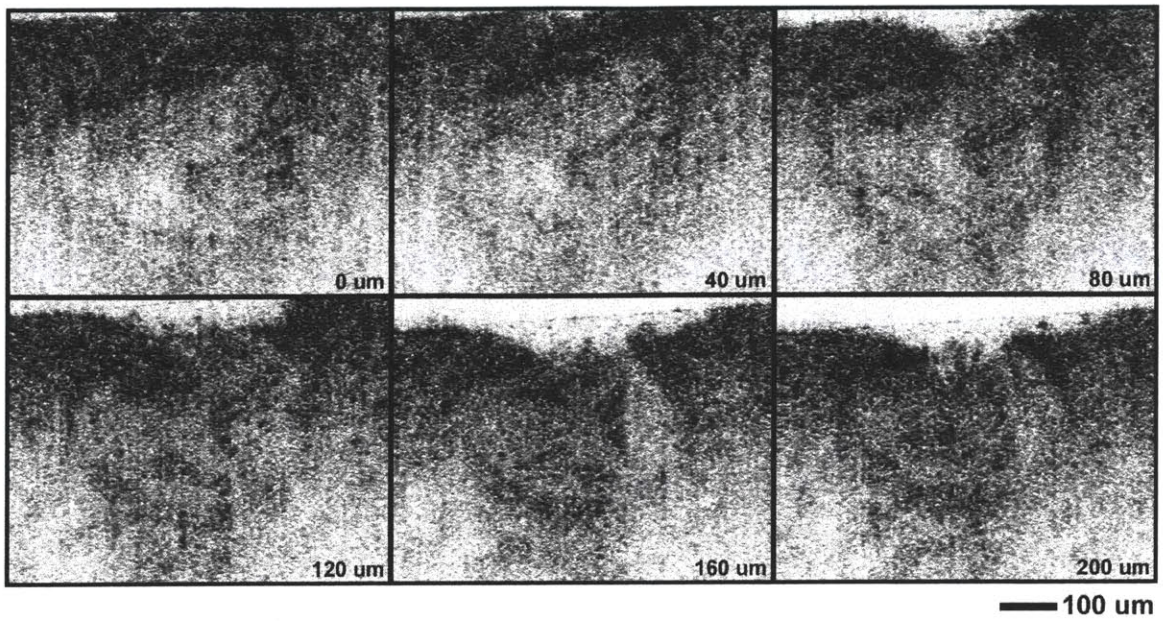

Figure 6.16: Sequence of cross-sectional OCT images of ductal hyperplasia showing three-dimensional structure of the duct lumen. Consecutive frames are spaced by 40 µm between frames. (Wavelength 1.09 µm, Resolution 3.5 µm axial x 6 µm transverse)

Figure 6.17 shows OCT images of biopsy site fat necrosis. Irregular adipose tissue and focal regions of increased scattering was observed in areas of fat necrosis, and image penetration depth was noticeably reduced.

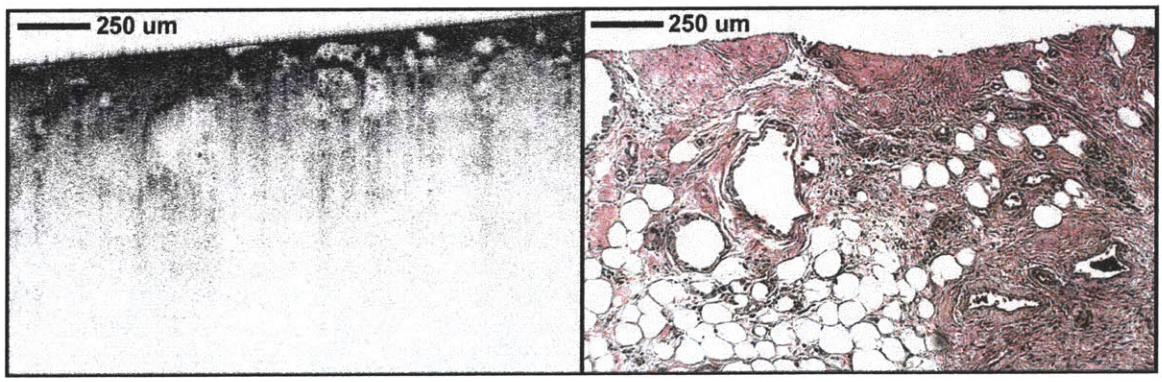

Figure 6.17: OCT image of biopsy site fat necrosis. Irregular low scattering necrotic adipose cells are clearly visible in the OCT images. Left, OCT; Right, Histology, Hematoxylin and Eosin 40x. (Wavelength 1.09 µm, Resolution 3.5 µm axial x 6 µm transverse)

Fibrosis and scarring present in specimens was visible in OCT images as regions of sharply increased scattering (Figure 6.18). Distorted ductal architecture surrounded by diffusely scattering stroma was also visible in some OCT images and corresponding to elastotic changes surrounding ducts (Figure 6.18). Anthracotic pigment was also visible in lymph nodes as focal regions of increased scattering with pronounced shadowing (Figure 6.19).

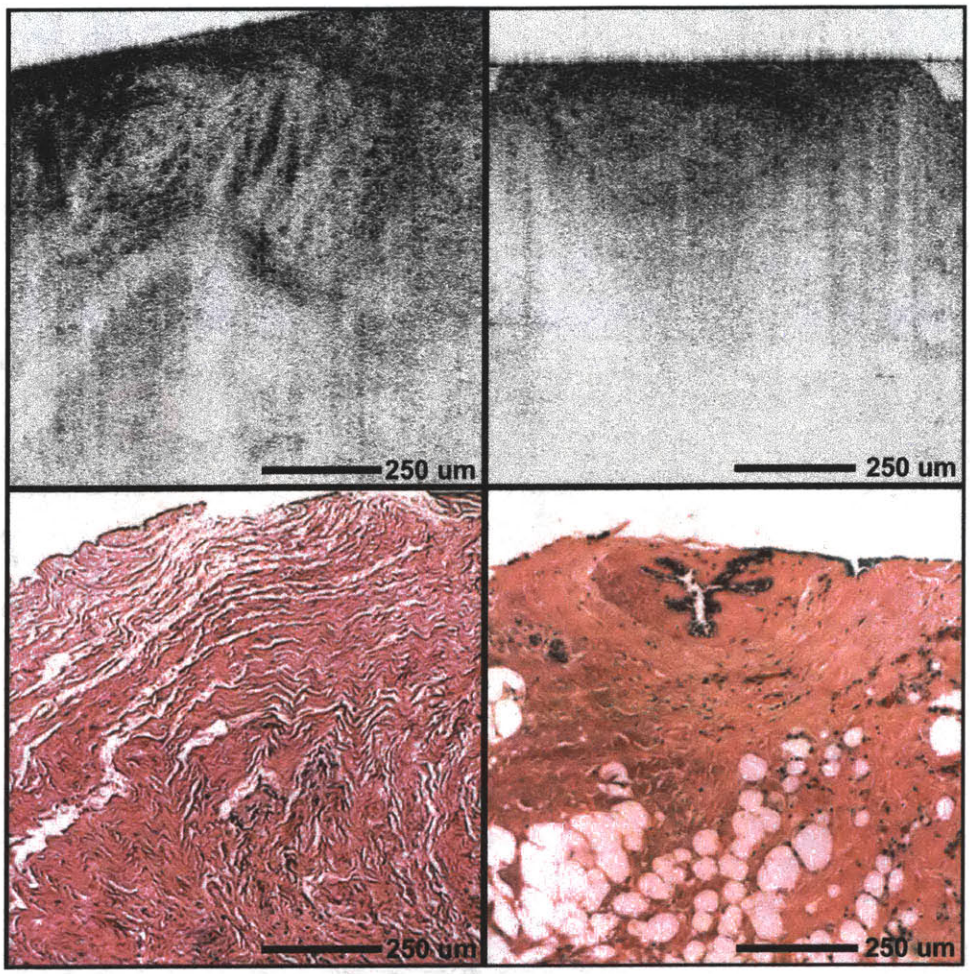

Figure 6.18: OCT images of fibrosis (left) and elastotic changes surrounding a duct (right). Top, OCT; Bottom, Histology, Hematoxylin and Eosin 40x. (Wavelength 1.09 µm, Resolution 3.5 µm axial x 6 µm transverse)

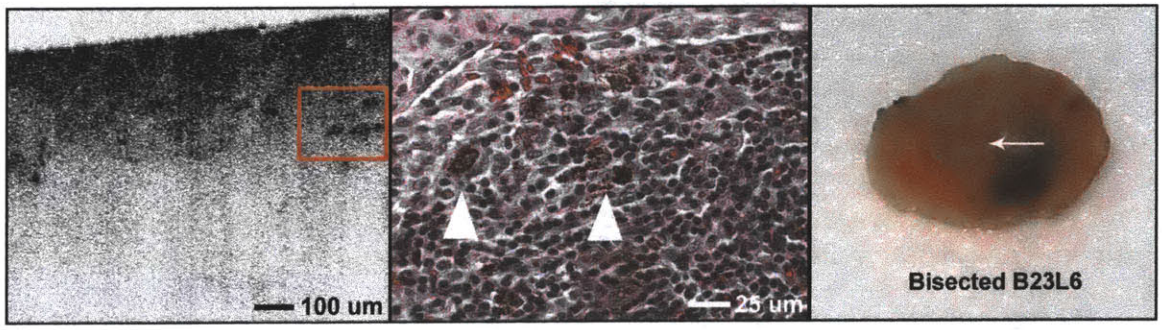

Figure 6.19: OCT image of anthracotic pigment occurring within a lymph node (inset and arrows). Left, OCT image; Center, Histology of inset region, Hematoxylin and Eosin 200x; Right, Photograph of bisected normal lymph node indicating imaging plane. (Wavelength 1.09 µm, Resolution 3.5 µm axial x 6 µm transverse)

Malignant

OCT images of DCIS within lobules and ducts are shown in Figure 6.20 and Figure 6.21, respectively. In Figure 6.20, tumor cells within the lobules appear lower scattering than the surrounding fibrous stroma. Dilation of the lobules due to the tumor cells and architectural distortion of the surrounding stroma was clearly visible. A microcalcification which was not sectioned in the corresponding histology micrograph was visible in the OCT image as a focal region of increased scattering with pronounced shadowing.

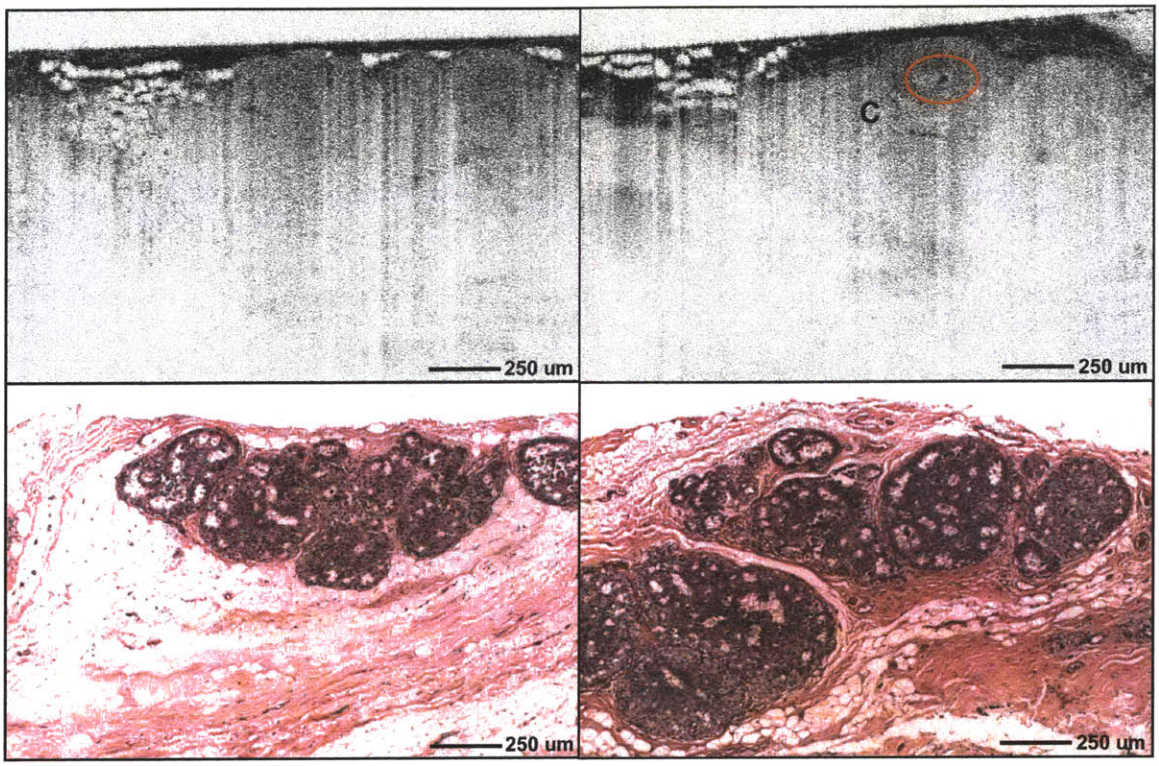

Figure 6.20: OCT images of DCIS occurring within lobules. Tumor cells appeared uniformly low-scattering and dilation and architectural distortion of the lobules is visible. A microcalcification (C, circled at right) within the lobules appears highly scattering with pronounced shadowing. Top, OCT; Bottom, Histology, Hematoxylin and Eosin 40x. (Wavelength 1.09 μm, Resolution 3.5 μm axial x 6 μm transverse)

Figure 6.21 shows OCT images of DCIS in ducts. Tumor cells within a large duct also appeared uniformly lower scattering relative to the surrounding thick collagenous stroma, and dilation of the duct is also visible.

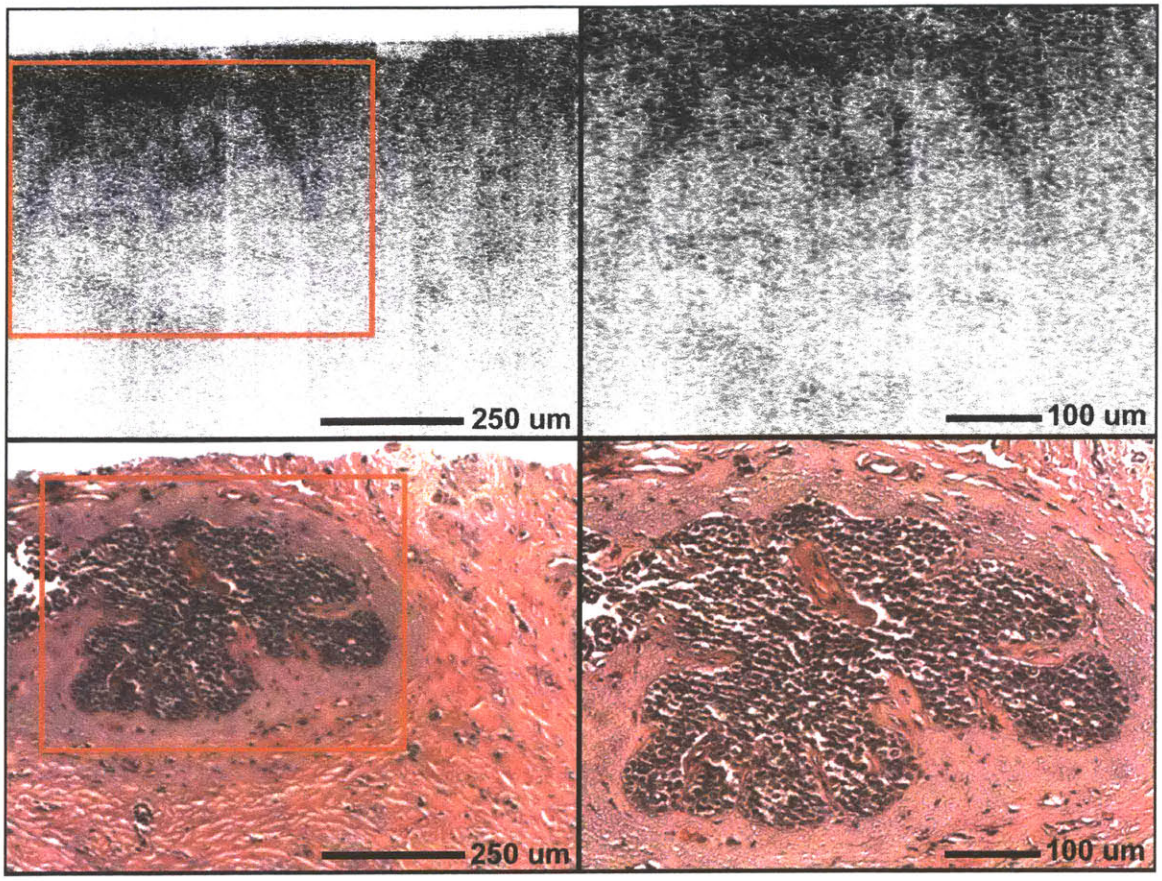

Figure 6.21: OCT images of DCIS within a duct. The duct lumen is completely occluded with low scattering tumor cells. Diffusely infilitrating tumor cells are present in the surrounding highly scattering desmoplastic stroma. Top, OCT; Bottom, Histology, Hematoxylin and Eosin 40x and 100x. (Wavelength 1.09 μm, Resolution 3.5 μm axial x 6 μm transverse)

Figure 6.22 shows OCT images of infiltrative ductal carcinoma. OCT images of ductal carcinoma revealed highly scattering and irregular regions which appeared to correspond to invasive cancer. Tongues of cancer cells exhibited increased scattering compared to surrounding regions and extended irregularly into the stroma.

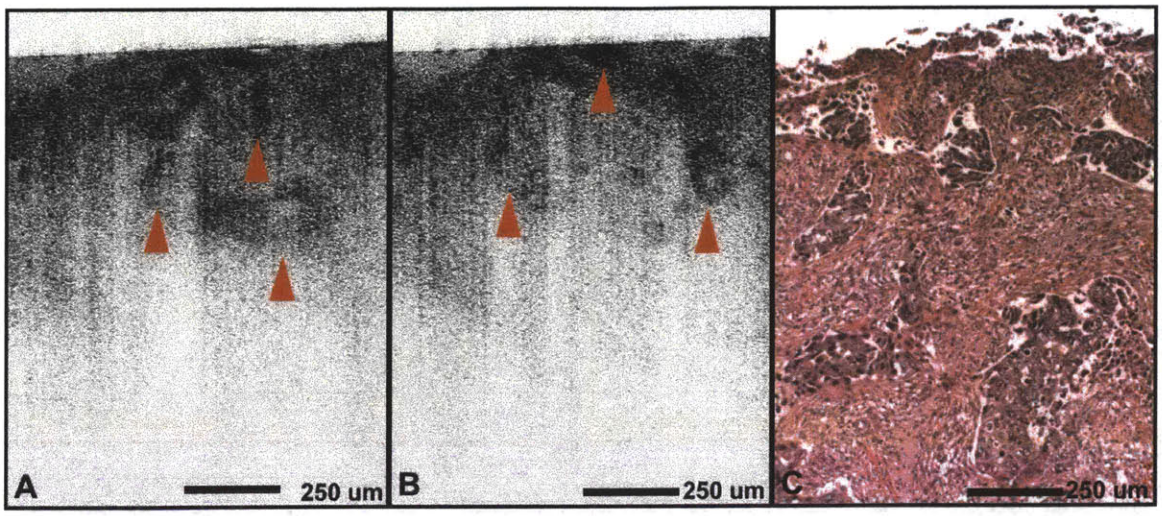

Figure 6.22: OCT images of infiltrative ductal carcinoma. Highly scattering regions (arrows) are visible in the OCT images which correspond to tongues of invasive cancer. A, B: OCT; C: Histology, Hematoxylin and Eosin 40x. (Wavelength 1.09 μm, Resolution 3.5 μm axial x 6 μm transverse)

OCT images of a microcalcification and corresponding histology of within a region of invasive ductal carcinoma are shown in Figure 6.23. Microcalcifications were visible as focal highly scattering regions which exhibited dramatic shadowing relative to regions of invasive cancer

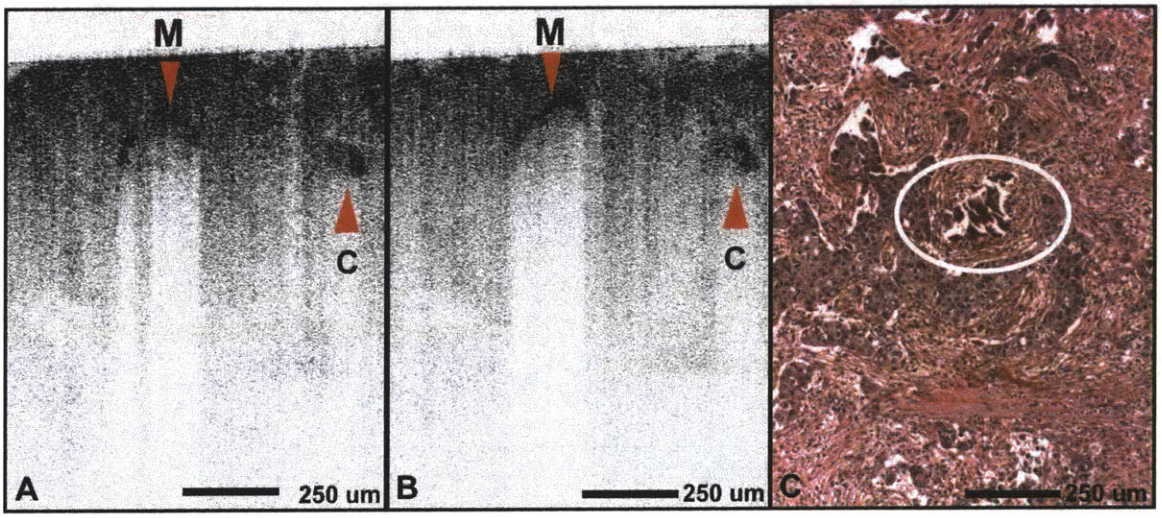

Figure 6.23: OCT images of microcalcification within a region of infiltrating ductal carcinoma. Microcalcification (M) appears as regions of high scattering which strongly shadows deeper regions. Invasive cancer (C) is visible in the vicinity of the calcification. A, B: OCT; C: Histology, Hematoxylin and Eosin 40x. (Wavelength 1.09 μm, Resolution 3.5 μm axial x 6 μm transverse)

Figure 6.24 shows and OCT image of infiltrative lobular carcinoma. In contrast to infiltrating ductal carcinoma, OCT images of lobular carcinoma appeared more homogeneously scattering. Isolated regions of increased scattering appeared to correspond to intervening fibrotic stroma, and entrapped fat was visible in some specimens. Specimens of infiltrating lobular carcinoma

were often indistinguishable on OCT from regions of fibrosis, fat necrosis, and inflammatory infiltrate associated with biopsy site changes.

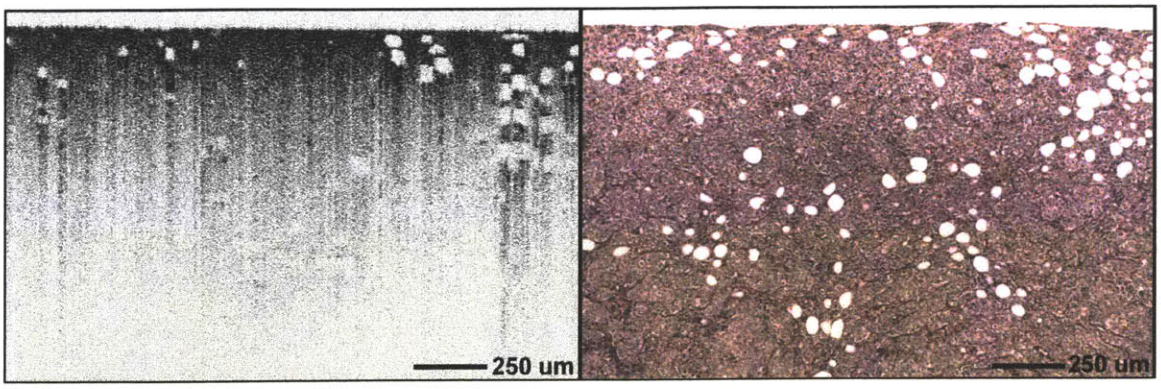

Figure 6.24: OCT image of infiltrating lobular carcinoma. Regions with densely infiltrating tumor cells appear low scattering and homogeneous, with isolated regions of entrapped fat. Left, OCT; Right, Histology, Hematoxylin and Eosin 40x. (Wavelength 1.09 μm, Resolution 3.5 μm axial x 6 μm transverse)

Figure 6.25 shows OCT images of lobular carcinoma metastasis to lymph node. Lymph nodes containing metastatic lobular carcinoma were unremarkable and were not distinguishable from normal lymph nodes based on OCT images. No specimens of lymph nodes with metastatic ductal carcinoma were available to image in this study.

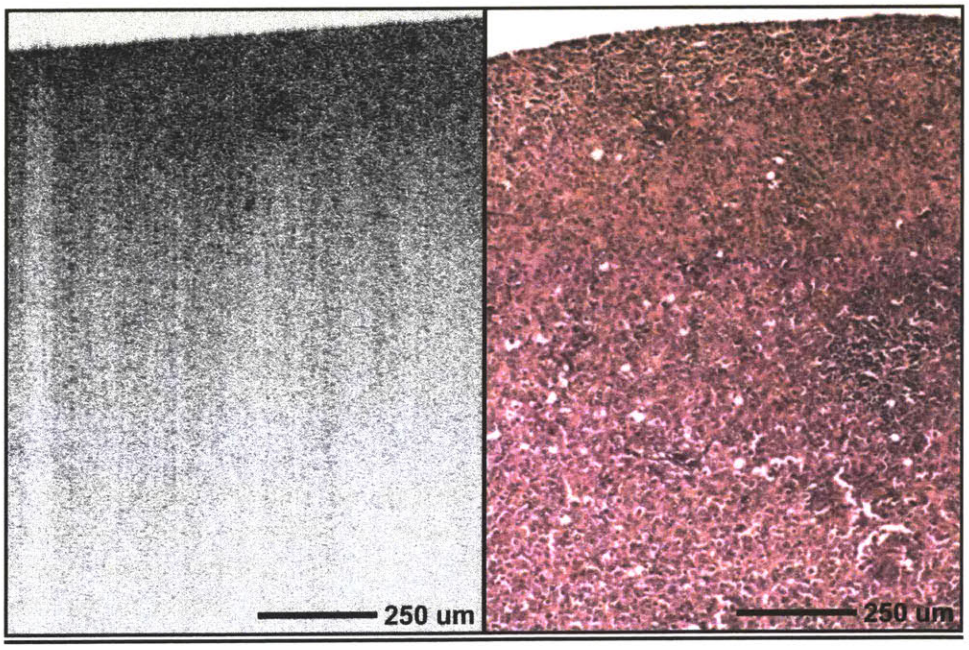

Figure 6.25: OCT image of metastatic infiltrating lobular carcinoma in a lymph node. Metastatic lobular carcinoma appears uniformly scattering. Left: OCT; Right: Histology, Hematoxylin and Eosin 40x. (Wavelength 1.09 μm, Resolution 3.5 μm axial x 6 μm transverse)

Three-dimensional rendering

3D imaging and volume rendering provided complementary information to cross-sectional OCT images, enabling visualization of arbitrary planes as well as subsurface tissue microstructure. Figures 6.26 shows a sequence of rendered *en face* images of fibroadipose tissue, similar to the view provided by microscopy. *En face* rendered images have the advantage that all image points are in constant focus. Note that regions beneath adipocytes exhibit increased scattering at deeper depths because of decreased light attenuation through adipocytes.

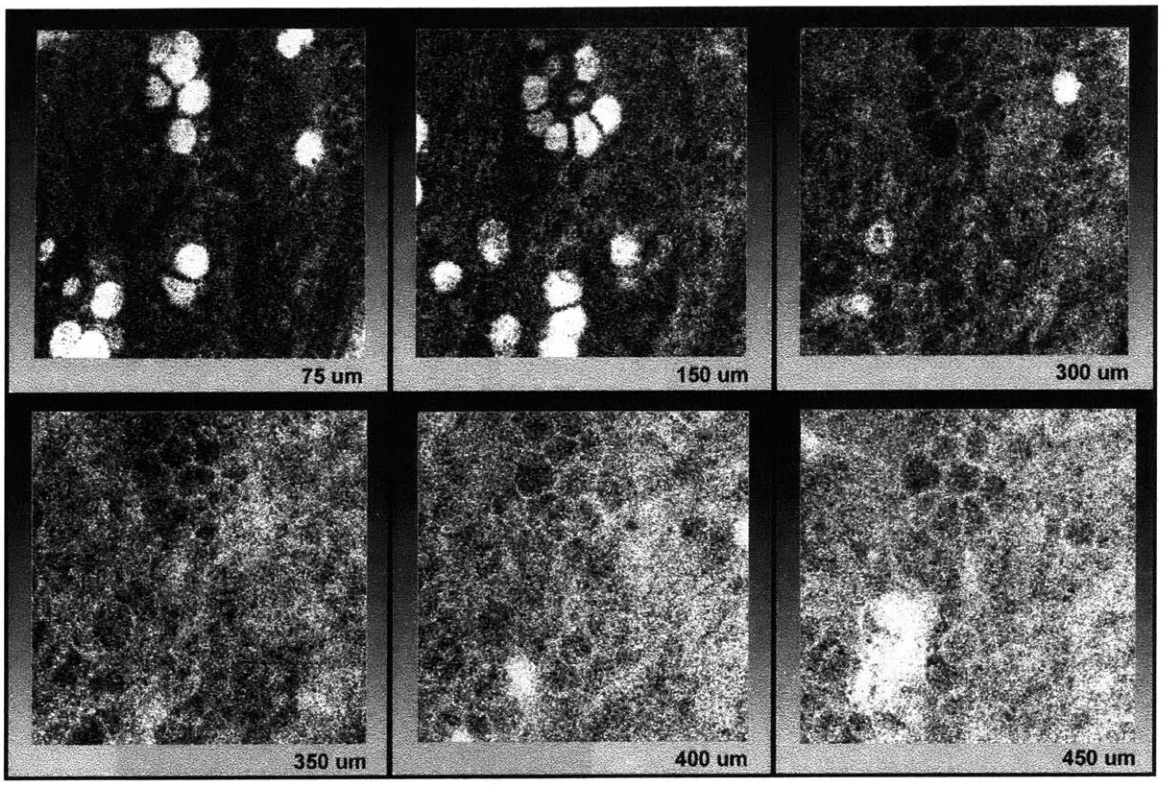

Figure 6.26: Sequence of *en face* OCT images of normal fibroadipose tissue spaced every 75 μm from the tissue surface. *En face* imaging enables the image plane to be kept in constant focus. Each image is 1 mm x 1 mm in dimension and consists of approximately 850 x 333 pixels rendered from 333 transverse slices. (Wavelength 1.09 μm, Resolution 3.5 μm axial x 6 μm transverse)

Figure 6.27 show a comparison of *en face* images of normal fibroadipose tissue and fibroadenoma. The ability to visualize arbitrary planes at different depths enables the three-dimensional tissue organization to be assessed in a way not possible using individual OCT images. Boundaries between stromal nodules (arrows) are clearly visible in the fibroadenoma which was distinct from the more heterogeneous fibrous stroma in the image of normal tissue.

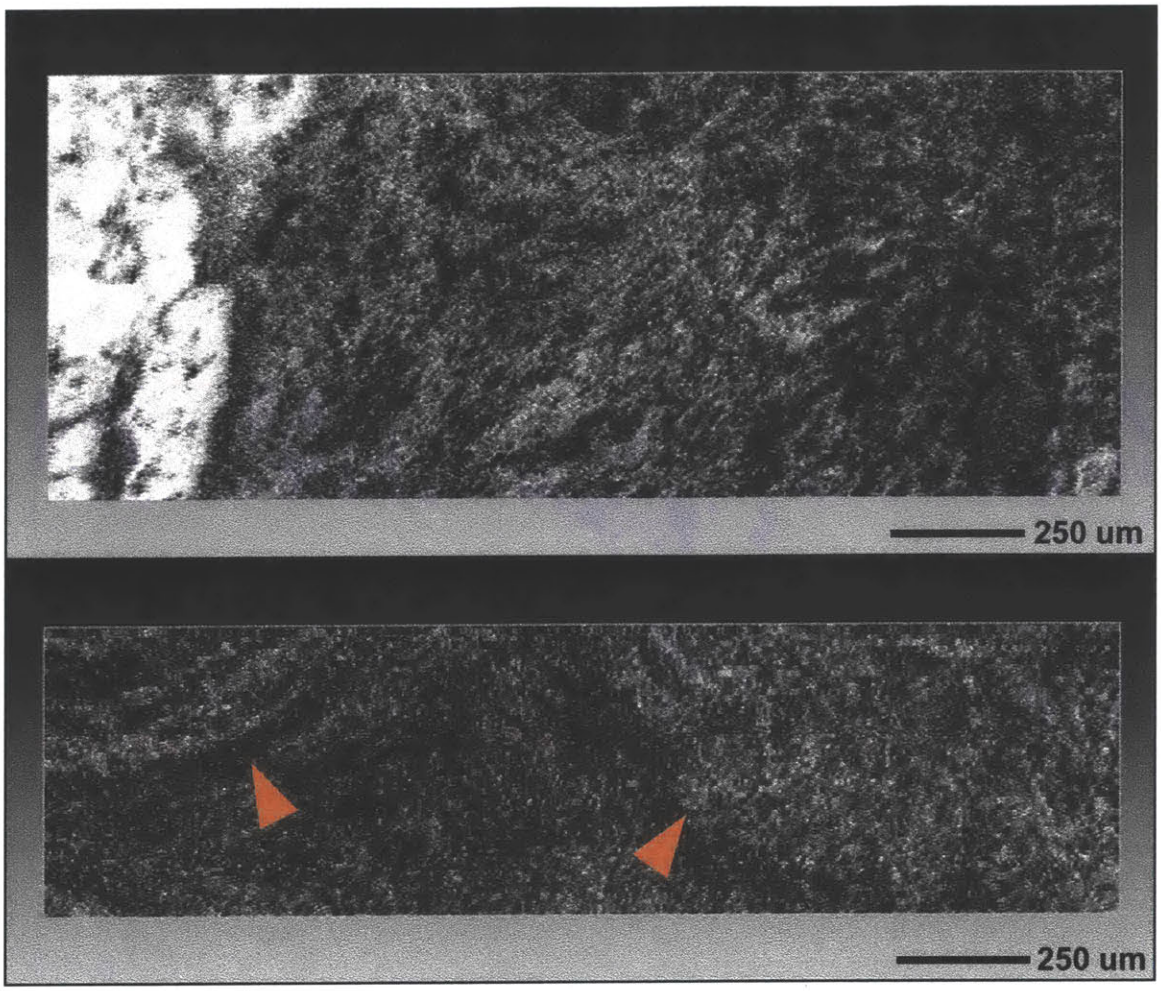

Figure 6.27: Rendered *en face* OCT images of normal fibroadipose tissue (top) and fibroadenoma (bottom). Distinctive bands indicating lobular stromal hyperplasia is visible in the fibroadenoma which is absent in normal fibrous tissue. (Wavelength 1.09 µm, Resolution 3.5 µm axial x 6 µm transverse)

Three-dimensional imaging also enables identification of low-contrast structures by tracking image features in multiple cross-sectional planes. Figure 6.28 shows normal fibroadipose tissue in contrast with DCIS within lobules and infiltrative lobular carcinoma. Large dilated lobules within regions of fat are visible in the image of DCIS which correspond to those seen in histology. Infiltrating lobular carcinoma with intervening fibrotic tissue more closely resembles structures visible in the corresponding histology in the *en face* plane than in the transverse plane (Figure 6.24).

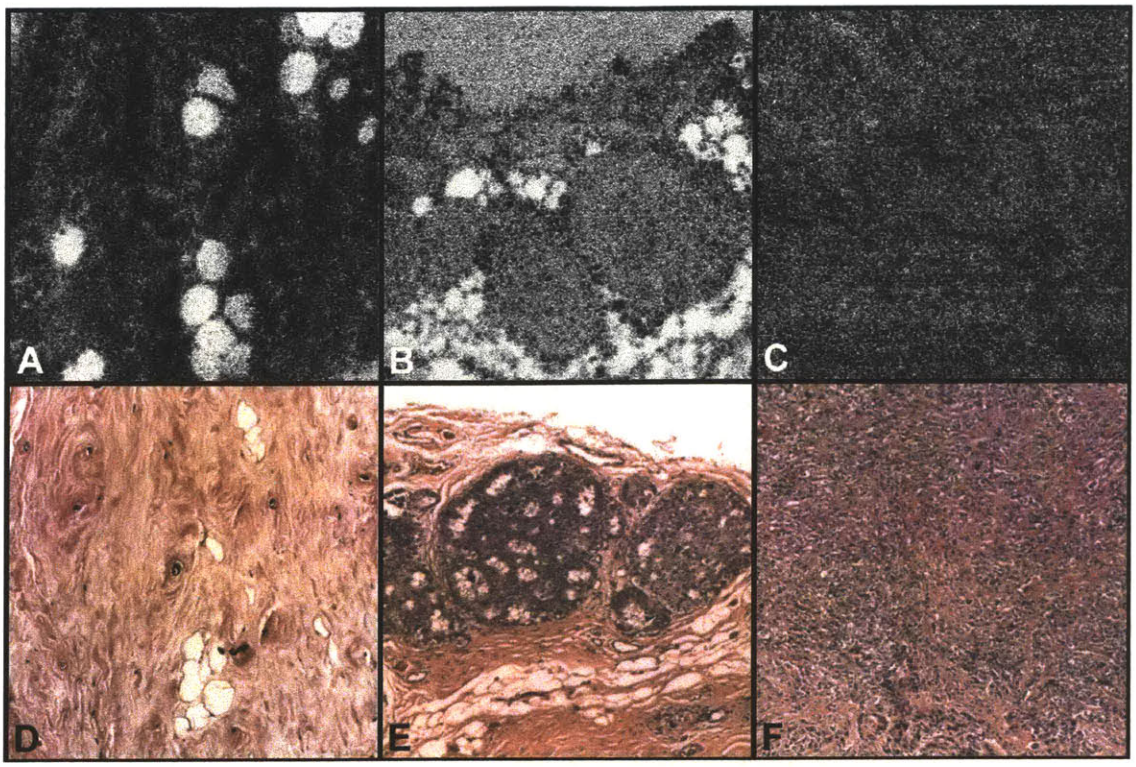

Figure 6.28: Rendered *en face* OCT images at 100 µm below the tissue surface. A, Normal breast stroma with adipocytes and fibrous tissue; B, DCIS in dilated lobules within fat; C, infiltrating lobular carcinoma. Histology (D-F) is obtained from corresponding specimens in the plane perpendicular to the OCT images. Each image is 1 mm x 1 mm in dimension and consists of approximately 850 x 333 pixels rendered from 333 transverse slices. (Wavelength 1.09 µm, Resolution 3.5 µm axial x 6 µm transverse)

Representative videos showing three-dimensional structure of a terminal lobular duct unit, normal lactiferous ducts, cystic changes, fibroadenoma, DCIS, infiltrative cancer, and microcalcifications are available in the supplemental materials.

DISCUSSION

Optical coherence tomography has been extensively investigated *in vivo* in ophthalmology, cardiology, and gastroenterology, but few published reports have examined OCT for imaging solid organs such as the breast. In part, practical considerations make *in vivo* imaging of solid organs complex. OCT imaging is limited in scattering tissues to penetration depths on the order of 2-3 mm, therefore imaging must be performed through an invasive imaging device. Scanning and image generation is also challenging from an engineering perspective because of the desire to make invasive imaging probes as small as possible. However, the high incidence and mortality associated with cancers of solid organs such as the breast and prostate make research into imaging techniques for early detection and treatment worth investigation.

Sampling error is generally recognized as a major issue of fine-needle aspiration cytology (FNAC), the standard method for obtaining breast samples for diagnosis of palpable breast lesions.[176, 177] Core-needle biopsy (CNBx) has come into more widespread use for both palpable

and non-palpable lesions due to the introduction of new more sensitive spring-loaded biopsy "guns,"[178] but still suffer from false-negative rates associated with sampling error.[179] With increased use of image guidance, higher sampling success rates have been achieved,[179, 180] but improvements are limited to lesions which are visible on ultrasound or mammography, which have limited resolutions and therefore cannot adequately identify small lesions or localize the full extent of lesions. In addition to the sampling limitations of diagnostic techniques, surgical methods for cancer treatment critically depend on accurate methods for assessment of microscopic resection margins. Negative excision margins are associated with low rates of local recurrence following lumpectomy and radiation therapy, while positive resection margins are associated with greater risk of recurrence.[181-183] Methods such as intraoperative frozen section analysis, which enables rapid histologic assessment of margins in the operating suite, are time- and labor-intensive and may lead to inadequate assessment of large specimens and loss of diagnostic material in small specimens.[184] Newer methods such as radioguided surgery[185, 186] have recently emerged as a method for resection guidance, with the potential for more accurate and less unnecessary surgery. A technique capable of performing subsurface, three-dimensional, micrometer-scale imaging in real time could permit guidance of biopsy procedures to reduce sampling errors and intraoperative monitoring of biopsy and surgical procedures, offering immediate information to the clinician and likely improving patient outcome.

The role of OCT in breast cancer research has recently been investigated *ex vivo* in the carcinogen-induced rat mammary tumor model.[190] In the reported study, ultrahigh resolution OCT imaging of normal fibroadipose tissue, early-stage ductal cancer, and infiltrative cancer in the rat mammary gland was presented. Three-dimensional rendering suggested tumor margins could be identified. Imaging results in the rat model suggested that tumor cells exhibit increased scattering relative to the surrounding stroma.

In this study, OCT was shown to enable imaging of benign and malignant lesions in the human breast. Normal mammary ducts and lobules could be identified within fibroadipose tissue. The epithelium and lumens of normal ducts larger than ~50 μm in diameter were visualized, while smaller ducts 20-25 μm in size could be distinguished based on their continuous and branching architecture in sequential transverse images. In contrast, lumens of ducts with ductal hyperplasia as well as ductal carcinoma-in-situ were not visible. These ducts were also associated with irregular scattering projections into the duct lumen which may correspond to presence of fibrovascular cores or collagenous stroma. Lobules with DCIS also were associated with pronounced architectural distortion of the surrounding stroma due to dilation of the lobules with cancer cells. Occlusion of lumens in combination with surrounding architectural distortion in the background of otherwise normal-appearing fibroadipose tissue could potentially therefore be used as a characteristic for hyperplasia or DCIS. Presence of microcalcifications within ducts and lobules, which were also visible in OCT images, could also additionally be used as an indirect sign of possible malignancy. In addition, infiltrative ductal carcinoma also appeared as regions of increased scattering relative to adjacent stroma. This increased scattering may result from relatively increased nuclear-to-cytoplasmic ratios of atypical cells compared to normal cells. This is consistent with earlier reports which describe breast cancer cells as exhibiting increased scattering relative to the surrounding stroma.[190] However, the low scattering associated with tumor cells in specimens with DCIS and infiltrative lobular carcinoma in this study suggests that the increased scattering associated with infiltrating ductal carcinoma is more likely associated

with desmoplastic reaction to infiltrating cancer than malignant cellular change. Presence of biopsy site changes, elastotic stroma, and scarring also complicate image interpretation. Given the wide range of changes associated with malignant breast lesions, imaging of larger numbers of specimens would be required to determine if these increased scattering changes can be consistently associated with neoplastic development.

This study also demonstrated ultrahigh resolution 3D OCT imaging of both benign and malignant human breast lesions. 3D imaging and rendering provided complementary information to cross-sectional OCT images, enabling visualization of arbitrary planes and tracking of features through multiple image planes, enabling identification of structures difficult to visualize from single images. The ability to render a tissue volume enables three-dimensional tissue organization to be assessed. A 3D reconstructed specimen can be rotated and arbitrary planes can be viewed from any angle, which is impossible with conventional light microscopy. OCT visualization in the *en face* plane also has the advantage that the entire plane of the image is within constant focus, allowing higher numerical aperture focusing and higher transverse resolutions to be achieved.

Acquisition of 3D OCT data is possible in the *ex vivo* setting of this study because motion artifacts are absent. However, with recent advances in OCT imaging technology using spectral/Fourier domain detection, dramatic improvements in imaging speed are possible.[165-167] Recent results in ophthalmic imaging have achieved ~100x improvements in imaging speeds.[168-171] These extremely high imaging speeds make 3D OCT feasible in an *in vivo* setting. In addition to high speed imaging, novel scanning devices such as micromechanical mirror or piezoelectric fiber scanners have also been recently developed. [172-175] These advances promise to enable 3D OCT laparoscopic imaging in the future.

CONCLUSION

This study presents the first ultrahigh resolution OCT images of normal and neoplastic lesions of the human breast. OCT imaging of normal, benign, and malignant breast lesions was performed and correlated with histology. Ultrahigh resolution imaging of normal mammary ducts and lobules was demonstrated, and ductal hyperplasia, microcalcifications, and infiltrative carcinoma could be visualized. Three-dimensional OCT imaging enables differentiation of *en face* and three-dimensional structure of tissue organization. It is possible that even with rapid access to specimens provided by this study, imaging in *ex vivo* specimens may have lower contrast and sharpness than *in vivo* imaging. Further investigations using larger numbers of specimens and blinded studies will be required in order to establish sensitivities and specificities to determine the usefulness of OCT for identifying early stage breast cancers and suitability for pursuing *in vivo* studies. These studies can be used as a baseline for development of new imaging technology for research in breast cancer and could aid the interpretation of future *in vivo* intraoperative OCT imaging studies.

Chapter 7

Summary and Conclusions

SUMMARY

Optical coherence tomography (OCT) is an emerging biomedical imaging technology that enables real-time, high-resolution imaging of tissue microstructure. OCT generates cross-sectional images of tissue optical backscattering as a function of depth with a higher resolution than any clinically available imaging technique. OCT can also be incorporated into a variety of fiber-optic devices, enabling development of minimally-invasive imaging probes for clinical applications.

Recent advances in broadband mirror and nonlinear fiber technology have allowed the development of portable broadband laser sources which enable a 3-10x improvement in OCT axial imaging resolution. This thesis describes the development of one such novel source for high-speed ultrahigh resolution OCT imaging and the application of portable ultrahigh resolution OCT technology for imaging human early neoplastic pathologies in the pathology laboratory setting. Early features of cancer are often focal, with diagnosis which may differ from slide to slide. Precise registration with histology is therefore required for correlation of OCT imaging with histology and accurate image interpretation. Imaging in the *ex vivo* setting enables careful control of imaging parameters, allowing correlation of OCT images with histology which is difficult to perform *in vivo*. *Ex vivo* studies allow systematic investigation of imaging parameters and optical markers characteristic of disease pathology to be investigated, establishing a baseline for future *in vivo* imaging studies. Studies in the pathology laboratory also enable rapid access to fresh surgical specimens, including diagnostically sensitive tissues and tumor margins, which are difficult to obtain in the laboratory setting.

It is possible that even with rapid access to specimens, imaging *ex vivo* specimens may result in lower contrast and sharpness than *in vivo* imaging. In Chapter 2, studies of the effect of tissue preservation on contrast in OCT images were performed in order to establish optimal tissue handling protocol for *ex vivo* imaging. Imaging was performed *in vivo* and *ex vivo* on the same

tissue site, and preservation using isotonic phosphate-buffered saline and DMEM cell culture media was investigated. Optical backscattering is sensitive to variations in refractive index in the tissue sample, and it was possible that local charges in tissue density as a result of tissue compression or stretching would change optical contrast. Therefore specimens approximately 1 cm x 1 cm in size were used in this study to minimize the effect of changes in optical contrast induced by loss of local supporting tissue structure. Minimal changes in the hamster cheek pouch were observed in the first 2 hours after excision using DMEM solution.

Imaging of normal, benign, and malignant lesions from fresh surgical specimens of thyroid, small and large intestine, and breast were performed in order to assess the feasibility of using ultrahigh resolution OCT for imaging early stage pathologies in these organ systems.

Current diagnostic imaging modalities of the thyroid gland cannot reliably distinguish benign from malignant lesions, primarily because of their inability to visualize microscopic structure. The feasibility of OCT for imaging thyroid tissue was explored for the first time *ex vivo* on the human thyroid gland. OCT imaging was performed at 1.3 μm wavelengths with a 4.5 μm axial image resolution and 11 μm spot size. Additional preliminary studies were also performed at 1.1 μm wavelengths with a 3.5 μm axial image resolution and 6 μm spot size. Imaging was performed in real time at 2-4 frames on three post-mortem and 20 surgically excised thyroid glands containing normal, hyperplastic and neoplastic tissue. Imaging of the thyroid gland clearly visualized individual colloid-filled follicles and their supporting stroma in normal thyroid, as well as the follicular epithelial layer in many specimens. Contrast between the colloid and follicular epithelium was high and signal attenuation was low, leading to increased image penetration depths of up to 2-3 millimeters. Images of degenerative, hyperplastic, adenomatous and malignant change within the thyroid gland were shown to correlate well with corresponding histopathologic findings. The ability of optical coherence tomography to image thyroid tissue microarchitecture makes it a potentially powerful technology that can be used to assess the thyroid gland at a resolution greater than currently available clinical imaging modalities.

Ultrahigh resolution and three-dimensional OCT was also investigated for *ex vivo* imaging of the large and small intestine. Extensive *in vivo* imaging studies in the GI tract have been performed in both animal models and in humans. Large patient studies have shown that OCT has high sensitivities and specificities for identifying Barrett's esophagus. However, currently all clinical studies have been performed using standard resolution OCT with 10-15 μm axial resolution. Ultrahigh resolution OCT could enhance imaging performance for the identification of early neoplastic changes. In this study, OCT imaging was performed on fresh surgical specimens from the large and small intestine in the pathology laboratory. Imaging at 1.3 μm wavelengths with a 4.5 μm axial image resolution and 11 μm spot size was first performed to investigate the effect of improved axial resolution at standard OCT wavelengths. Studies were also performed at 1.1 μm wavelengths with a 3.5 μm axial image resolution and 6 μm spot size. These studies are important because high performance lasers are commercially available at this wavelength. Normal and pathologic areas from 23 surgical specimens of the large and small intestine were imaged. Ultrahigh resolution OCT distinguished the epithelial layer of the mucosa and visualized individual villi, glands, and crypts. Finer transverse resolutions improved visualization of features such as the epithelium, but reduced depth of field. Architectural distortion of glands from inflammatory and neoplastic processes was observed. Three-dimensional rendering

enabled visualization of surface pit pattern and mucosal folds as well as subsurface crypt microstructure. The potential of OCT to both render surface morphology and visualize subsurface tissue microstructure has the potential to aid in real-time staging of lesions for endoscopic mucosal resection. These studies can be used as a baseline for development of new OCT technology and could aid the interpretation of future ultrahigh resolution endoscopic imaging studies.

This thesis also investigated the feasibility of OCT for imaging benign and malignant lesions of the human breast. This study presents the first ultrahigh resolution OCT images of human breast to our knowledge. Studies were performed at 1.1 μm wavelengths with a 3.5 μm axial image resolution and 6 μm spot size. Thirteen cases from adult patients, consisting of a total of 41 separate specimens, were each imaged within several hours of excision. Collected specimens consisted of both normal and pathologic sites from each case. Selected specimens with suspicion of *in situ* carcinoma were also mammogrammed separately to guide OCT imaging to regions of identified microcalcifications suspicious for carcinoma. OCT was demonstrated to enable visualization of normal mammary ducts and lobules as well as normal fibroadipose tissue. The epithelial layer lining normal ducts was identified. Specimens of atypical ductal hyperplasia, fibroadenoma, lipoma, microcalcifications, and infiltrating ductal carcinoma exhibited characteristic features and correlated well with histology. Three-dimensional imaging and rendering was also performed. Optical imaging contrast between normal glandular structure and fibrous stroma in breast tissue was relatively low. Tracking suspected glandular structures through multiple imaging planes was important for identifying characteristic features differentiating glands from the adjacent stroma and differentiating glands from small ducts in cross-section. Further investigations using larger numbers of specimens and blinded studies will be required in order to establish sensitivities and specificities to determine the usefulness of OCT for identifying early stage breast cancers. These studies can be used as a baseline for development of new imaging technology for research in breast cancer and could serve as an adjunct to investigative studies of mammary ductoscopy or aid the interpretation of *in vivo* intraoperative OCT imaging studies.

FUTURE STUDIES

Hamster model of squamous carcinoma

The ability of ultrahigh resolution OCT to identify features associated with early stage dysplastic changes can also be investigated in animal models of tumor carcinogenesis. Tumor induction in animal models is well-characterized, and provides controlled timepoints for imaging at different stages of development. Imaging *in vivo* in animal models is well-controlled and histology can be obtained at different timepoints, enabling OCT images to be directly correlated with developing pathology to establish optical markers for neoplastic progression.

The Syrian golden hamster cheek pouch carcinogenesis model closely resemble the events involved in the development of premalignant and malignant human oral cancers.[191-193] In addition, it is one of the most well-characterized models for squamous cell carcinomas, which affects a wide variety of organs including the skin, oral cavity, pharynx, larynx, and cervix. Using 7,12-dimethylbenzaanthracene (DMBA)-induced carcinogenesis, early dysplastic changes

through invasive squamous cell carcinoma can be induced during a 12 week timecourse.[194] Because it has a well-controlled cancer progression, the hamster cheek pouch model has been used in other studies involving fluorescence and optical imaging of neoplastic changes.[121, 123, 195-198] The feasibility of using OCT for imaging hamster cheek pouch tumorigenesis has recently been reported.[199] However, this study used lower resolutions and did not demonstrate imaging of early dysplastic changes which arise in the epithelium.

In this thesis, ultrahigh resolution OCT was shown to enable clear visualization of normal keratinized squamous epithelium in the hamster cheek pouch, as well as the underlying muscle and supporting tissue layers and vessels. Normal hamster cheek pouch epithelium appeared homogeneous and uniformly scattering and could be clearly delineated from the underlying lamina propria. Clear visualization and characterization of normal squamous epithelium has been demonstrated, therefore this model would be ideally suited for investigating the ability of OCT to identify optical scattering changes associated with dysplasia occurring within the squamous epithelial layer. It is possible that early dysplastic changes may be beyond the imaging resolution and contrast of even ultrahigh resolution OCT, therefore microscopy methods should be investigated in parallel.[159, 200] The hamster cheek pouch model allows repeatable imaging of the tissue architecture, and therefore serves as an excellent model for assessing the ability of ultrahigh resolution OCT for imaging early neoplastic changes in squamous epithelial tissues and assessing neoplastic progression.

AOM murine model

The use of azoxymethane (AOM) carcinogen is an established model for colorectal cancer that has been demonstrated to induce tumors within the murine colon. AOM is metabolite of 1,2-Dimethylhydrazine (DMH) which has been used extensively to induce colon tumors in a number of rodent species.[201-207] AOM tumors share similar histological characteristics with human tumors,[208, 209] and thus serves as a good model to study tumor progression within the colon. The use of colon-specific carcinogens in murine models has been shown to induce early stage morphological changes (aberrant crypts) through dysplasia to invasive adenocarcinoma.[201-203, 206] In the rat AOM model, neoplastic progression from ACF begin as early as 5 weeks, progress through multiple crypts through gross adenoma, with invasive adenocarcinoma by 53 weeks.[203, 206, 210] Flat dysplastic lesions occurring in the AOM models may also serve as a useful model for detection of non-pedunculated dysplasia-associated lesions, which can occur in human patients with chronic inflammatory bowel disease. These lesions are often difficult to distinguish and associated with a significantly increased risk of colorectal cancer.[147, 211]

By studying colonic epithelium during tumor induction in the AOM model, the architectural and morphological changes associated with gastrointestinal tumor progression can be investigated. These studies would allow investigation of OCT imaging markers for dysplasia in model of adenocarcinoma, the most common form of carcinoma in the prostate as well as the colorectal tract. Previous studies have demonstrated the capability of fiberoptic confocal imaging to visualize architecture within the rat colon.[212, 213] *In vivo* imaging of colonic tumors in mice has also been investigated with standard resolution OCT imaging.[214] Ultrahigh resolution imaging techniques can first be performed *ex vivo* in order to investigate imaging of early stage colonic tumors based on architectural changes. As it is possible that early dysplastic changes may be

beyond the imaging resolution and contrast of even ultrahigh resolution OCT, microscopy techniques can also be investigated in this model in parallel to assess cellular-level features.[159, 200] Identification of morphological changes in the early stages of neoplastic development and progression would lead to valuable insight into this and other colonic cancer models.

***In vivo* studies in the upper gastrointestinal tract**

A particularly promising application of optical biopsy using OCT is as an adjunct to endoscopic imaging of the gastrointestinal tract. Numerous *in vivo* endoscopic OCT studies have been performed indicating that OCT has the potential to distinguish morphological changes associated with gastrointestinal pathologies. However, all clinical studies to date have used standard resolution OCT with 10-15 μm axial resolution and have been unable to identify early neoplastic changes associated with high-grade dysplasia. If ultrahigh resolution OCT can be demonstrated to significantly enhance imaging performance for the identification of dysplastic changes, OCT could become a powerful tool for guiding excisional biopsy to improve sensitivity and reduce false negative rates in patients at risk for developing esophageal cancer.

These ongoing studies use a prototype compact Cr^{4+}:Forsterite laser source, identical to one of the two sources used in Chapters 4 and 5 of this thesis. Figure 7.1A shows a representative *in vivo* ultrahigh resolution OCT image of normal esophagus in a human subject. The OCT image shows the relatively homogeneous squamous epithelium (ep), the higher-backscattering lamina propria (lp), the lower-backscattering muscularis mucosa (mm), the higher-backscattering submucosa (sm), and the low-backscattering and thick muscularis propria (mp). In contrast, Figure 7.1B shows a representative OCT image of a region of Barrett's esophagus from the same patient. The OCT images demonstrate clear differences between Barrett's esophagus when compared to normal squamous epithelium. The uniformly layered structure of normal esophagus has been disrupted by the presence of multiple gland-like structures. Boundaries between individual glands appear highly scattering, with a lower-scattering epithelial layer lining the glands.

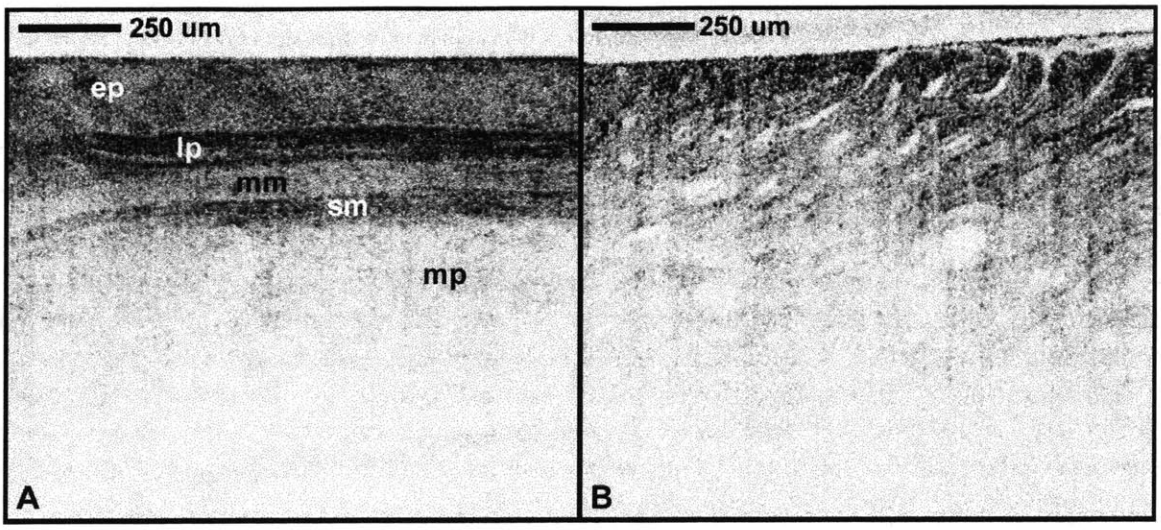

Figure 7.1: A. Image of normal esophagus *in vivo*. The normal layered structure of the esophagus is well defined with a clearly visible homogeneous squamous epithelium (ep) above the highly backscattering lamina propria (lp). Deeper layers of the muscularis mucosa (mm), submucosa (sm), and muscularis propria (mp) are also visible. B. Image of Barrett's esophagus from the same patient shows characteristic disruption of the epithelium, with multiple gland-like structures. (Wavelength 1.26 μm, Resolution 3.7 μm axial x 15 μm transverse)

The sensitivity and specificity of standard resolution OCT for detecting Barrett's esophagus has recently been demonstrated.[72] Improving axial resolution and reducing speckle using ultrahigh resolution OCT imaging improves visualization of architectural morphology. However, ongoing investigations are required to determine whether OCT can identify optical markers which may enable differentiation of dysplasia *in vivo*.

One obstacle in this challenge is ensuring correlation between *in vivo* OCT images and histologic diagnosis from biopsy. Many histologic diagnoses of dysplasia are focal, implying that reliable correlation of imaging with histology will be difficult to achieve *in vivo*. Groups have attempted to overcome this by designing special OCT catheter probes which minimizing catheter motion during imaging and enable immediate acquisition of biopsy samples from the imaging site after imaging. Another strategy has been to use adenomatous colonic polyps as models for dysplasia, since polyps are removed in entirety during polypectomy.[73]

Registration can also be achieved by directly imaging biopsy specimens immediately after excision. Figure 7.2 and Figure 7.3 shows preliminary *ex vivo* biopsy images of normal squamous epithelium and a region at the junction between normal squamous and Barrett's esophagus. The relatively homogeneous and uniformly scattering squamous epithelium can be clearly distinguished from heterogeneous glandular epithelium.

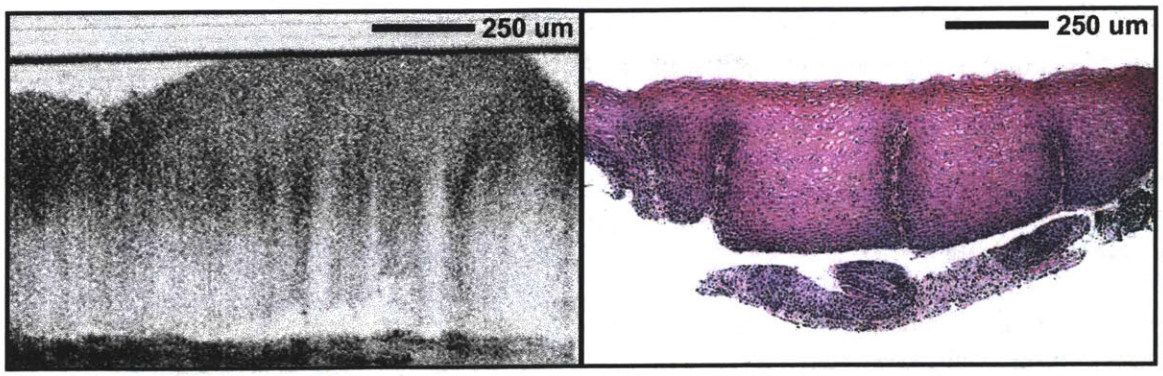

Figure 7.2: Left, *Ex vivo* OCT biopsy imaging of normal squamous epithelium. The squamous epithelium is uniformly scattering. The highly scattering band corresponds to the bottom surface of a glass coverslip used to minimize imaging aberrations. Right, Histology, Hematoxylin and Eosin, 40x. (Wavelength 1.26 µm, Resolution 3.7 µm axial x 6 µm transverse)

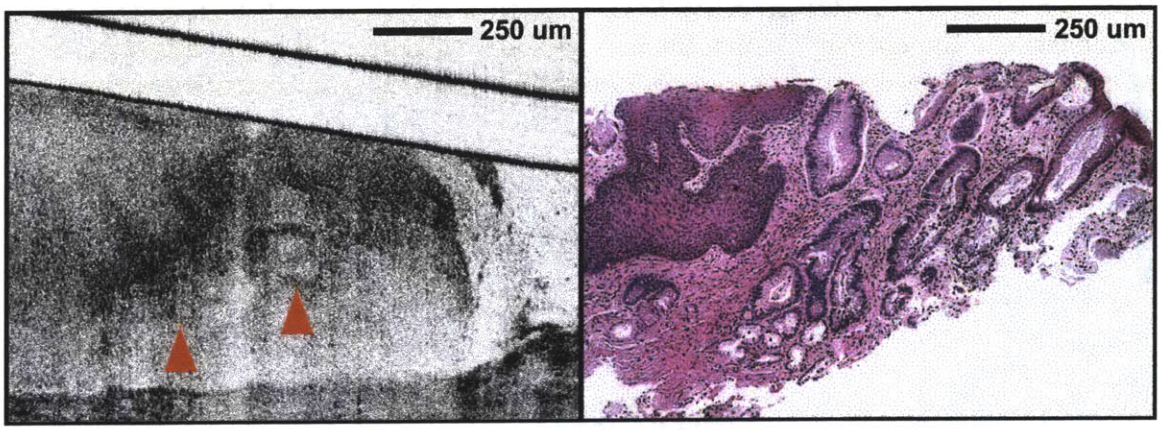

Figure 7.3: Left, *Ex vivo* OCT biopsy imaging of junction between squamous epithelium and Barrett's esophagus shows characteristic glandular structures (arrows). Right, Histology, Hematoxylin and Eosin, 40x. (Wavelength 1.26 µm, Resolution 3.7 µm axial x 6 µm transverse)

Biopsy specimens are typically shallow, allowing imaging and correlation with specimens of relatively superficial regions of the esophagus. However, precise registration possible by imaging biopsies in entirety *ex vivo* may enable unambiguous identification of optical markers associated with dysplasia. It is possible that the small size of specimens and therefore loss of supporting tissue structure influences architectural integrity, which may alter the contrast of *ex vivo* structures compared to *in vivo* imaging. Image analysis techniques will also likely be required in order to identify optical markers which can be correlated to dysplasia both in *ex vivo* and *in vivo* images. These questions are of significant interest and are being addressed in ongoing studies.

CONCLUSION

Recent advances in OCT imaging technology have enabled improvements in axial resolution, imaging speed, and imaging sensitivity, improved image quality and enabling studies to be

performed in the clinical setting. *Ex vivo* investigations performed *ex vivo* in the pathology laboratory examined the feasibility of using OCT for imaging normal and neoplastic pathologies in the thyroid, intestinal tract, and breast. These studies elucidated the optimal imaging parameters, potential and limitations of this technique, and established the microstructural markers visible in OCT images that are characteristic of pathology in these organ systems. These studies should serve as a useful baseline for development of new OCT technologies and aid in interpretation of future *in vivo* investigations.

A major unresolved question is whether OCT is capable of detecting hallmarks of changes associated with early dysplasia. This thesis has shown that larger-scale tissue architectural features, such as glandular and ductal structure and epithelial thickening, can be visualized using OCT in selected human tissue types. However, standard histologic features of dysplasia, such as enlarged nuclei and increased nuclear-to-cytoplasmic ratio, are based on cellular characteristics and may therefore require cellular-level imaging techniques to distinguish. The role of OCT in early cancer detection may therefore depend on the ability to establish a definitive correlation between tissue architectural organization and early stage disease. As with any diagnostic technique, the relative effectiveness of OCT will need to be weighed against alternative methods. Optical coherence tomography will ultimately require validation through extensive *in vivo* patient studies to assess sensitivities and specificities for detecting early neoplastic pathologies.

REFERENCES

1. National Center for Health Statistics: Deaths/Mortality: Center for Disease Control, 2002:http://www.cdc.gov/nchs/fastats/deaths.htm.
2. American Cancer Society: Cancer Facts & Figures, 2004.
3. Huang D, Swanson EA, Lin CP, Schuman JS, Stinson WG, Chang W, Hee MR, Flotte T, Gregory K, Puliafito CA, Fujimoto JG. Optical coherence tomography. Science 1991;254:1178-81.
4. Fujimoto JG, Brezinski ME, Tearney GJ, Boppart SA, Bouma B, Hee MR, Southern JF, Swanson EA. Optical biopsy and imaging using optical coherence tomography. Nature Medicine 1995;1:970-2.
5. Pitris C. High resolution imaging of neoplasia using optical coherence tomography. Electrical Engineering and Computer Science and Health Sciences and Technology. Cambridge: Massachusetts Institute of Technology, 2000:156.
6. Pitris C, Brezinski ME, Bouma BE, Tearney GJ, Southern JF, Fujimoto JG. High resolution imaging of the upper respiratory tract with optical coherence tomography - A feasibility study. American Journal of Respiratory and Critical Care Medicine 1998;157:1640-4.
7. Jesser CA, Boppart SA, Pitris C, Stamper DL, Nielsen GP, Brezinski ME, Fujimoto JG. High resolution endoscopic evaluation of transitional cell carcinoma with optical coherence tomography. British Journal of Radiology 1999;72:1170-6.
8. Pitris C, Goodman A, Boppart SA, Libus JJ, Fujimoto JG, Brezinski ME. High-resolution imaging of gynecologic neoplasms using optical coherence tomography. Obstetrics and Gynecology 1999;93:135-9.
9. Pitris C, Jesser C, Boppart SA, Stamper D, Brezinski ME, Fujimoto JG. Feasibility of optical coherence tomography for high-resolution imaging of human gastrointestinal tract malignancies. Journal of Gastroenterology 2000;35:87-92.
10. Jemal A, Tiwari RC, Murray T, Ghafoor A, Samuels A, Ward E, Feuer EJ, Thun MJ. Cancer statistics, 2004. CA: A Cancer Journal for Clinicians 2004;54:8-29.
11. Ho GY, Burk RD, Klein S, Kadish AS, Chang CJ, Palan P, Basu J, Tachezy R, Lewis R, Romney S. Persistent genital human papillomavirus infection as a risk factor for persistent cervical dysplasia. Journal of the National Cancer Institute 1995;87:1365-71.
12. Chang MH, Chen CJ, Lai MS, Hsu HM, Wu TC, Kong MS, Liang DC, Shau WY, Chen DS. Universal hepatitis B vaccination in Taiwan and the incidence of hepatocellular carcinoma in children. Taiwan Childhood Hepatoma Study Group. New England Journal of Medicine 1997;336:1855-9.
13. Folkman J. How is blood vessel growth regulated in normal and neoplastic tissue? G.H.A. Clowes memorial Award lecture. Cancer Research 1986;46:467-73.
14. Folkman J, Klagsbrun M. Angiogenic factors. Science 1987;235:442-7.
15. Liotta LA. Tumor invasion and metastases--role of the extracellular matrix: Rhoads Memorial Award lecture. Cancer Research 1986;46:1-7.
16. Liotta LA. Tumor invasion and metastases: role of the basement membrane. Warner-Lambert Parke-Davis Award lecture. American Journal of Pathology 1984;117:339-48.
17. Paget S. The distribution of secondary growths in cancer of the breast. 1889. Cancer Metastasis Reviews 1989;8:98-101.

18. American Cancer Society: Cancer Prevention and Early Detection Facts & Figures 2004.
19. Freeman HP. Cancer in the socioeconomically disadvantaged. CA: A Cancer Journal for Clinicians 1989;39:266.
20. DeVita VT, Rosenberg SA, Hellman S. Cancer: Principles and Practices of Oncology. Lippincott Williams & Wilkins, 1993.
21. American Cancer Society: Radation Therapy Principles. 2004.
22. American Cancer Society: Chemotherapy Principles. 2004.
23. American Cancer Society: Surgery. 2004.
24. American Cancer Society: Nonspecific Immunotherapies and Adjuvants, 2004.
25. U.S. Food and Drug Administration: FDA Drug Approvals List: Intron A (Interferon alfa-2b). 1997.
26. Goldenberg DM. New developments in monoclonal antibodies for cancer detection and therapy. CA: A Cancer Journal for Clinicians 1994;44:43-64.
27. American Cancer Society: Monoclonal Antibody Therapy (Passive Immunotherapy), 2004.
28. Smith RA, Saslow D, Sawyer KA, Burke W, Costanza ME, Evans WP, Foster RS, Hendrick E, Eyre HJ, Sener S. American Cancer Society guidelines for breast cancer screening: update 2003. CA: A Cancer Journal for Clinicians 2003;53:141-69.
29. Diederich S. Screening for early lung cancer with low-dose spiral computed tomography. Lancet 2003;362:588-9.
30. Patz EF, Jr., Swensen SJ, Herndon JE, 2nd. Estimate of lung cancer mortality from low-dose spiral computed tomography screening trials: implications for current mass screening recommendations. Journal of Clinical Oncology 2004;22:2202-6.
31. Yasuda S, Ide M, Fujii H, Nakahara T, Mochizuki Y, Takahashi W, Shohtsu A. Application of positron emission tomography imaging to cancer screening. British Journal of Cancer 2000;83:1607-11.
32. Schnall MD. Application of magnetic resonance imaging to early detection of breast cancer. Breast Cancer Research 2001;3:17-21.
33. Abraham DC, Jones RC, Jones SE, Cheek JH, Peters GN, Knox SM, Grant MD, Hampe DW, Savino DA, Harms SE. Evaluation of neoadjuvant chemotherapeutic response of locally advanced breast cancer by magnetic resonance imaging. Cancer 1996;78:91-100.
34. Rifkin MD, Zerhouni EA, Gatsonis CA, Quint LE, Paushter DM, Epstein JI, Hamper U, Walsh PC, McNeil BJ. Comparison of magnetic resonance imaging and ultrasonography in staging early prostate cancer. Results of a multi-institutional cooperative trial. New England Journal of Medicine 1990;323:621-6.
35. Karlan BY, Platt LD. The current status of ultrasound and color Doppler imaging in screening for ovarian cancer. Gynecological Oncology 1994;55:S28-33.
36. Cohen CJ, Jennings TS. Screening for ovarian cancer: the role of noninvasive imaging techniques. American Journal of Obstetrics and Gynecology 1994;170:1088-94.
37. Wallace MB, Fritscher-Ravens A, Savides TJ. Endoscopic ultrasound for the staging of non-small-cell lung cancer. Endoscopy 2003;35:606-10.
38. D'Amico AV, Whittington R, Schnall M, Malkowicz SB, Tomaszewski JE, Schultz D, Wein A. The impact of the inclusion of endorectal coil magnetic resonance imaging in a multivariate analysis to predict clinically unsuspected extraprostatic cancer. Cancer 1995;75:2368-72.

39. Brugge WR, Lee MJ, Carey RW, Mathisen DJ. Endoscopic ultrasound staging criteria for esophageal cancer. Gastrointestinal Endoscopy 1997;45:147-52.
40. Meyenberger C, Huch Boni RA, Bertschinger P, Zala GF, Klotz HP, Krestin GP. Endoscopic ultrasound and endorectal magnetic resonance imaging: a prospective, comparative study for preoperative staging and follow-up of rectal cancer. Endoscopy 1995;27:469-79.
41. Akahoshi K, Chijiiwa Y, Nakano I, Nawata H, Ogawa Y, Tanaka M, Nagai E, Tsuneyoshi M. Diagnosis and staging of pancreatic cancer by endoscopic ultrasound. British Journal of Radiology 1998;71:492-6.
42. Fritscher-Ravens A. Endoscopic ultrasound evaluation in the diagnosis and staging of lung cancer. Lung Cancer 2003;41:259-67.
43. Kiesslich R, Jung M. Magnification endoscopy: does it improve mucosal surface analysis for the diagnosis of gastrointestinal neoplasias? Endoscopy 2002;34:819-22.
44. Fleischer DE. Chromoendoscopy and magnification endoscopy in the colon. Gastrointestinal Endoscopy 1999;49:S45-9.
45. Technology status evaluation report. High resolution and high-magnification endoscopy. Gastrointestinal Endoscopy 2000;52:864-6.
46. Jaramillo E, Watanabe M, Befrits R, Ponce de Leon E, Rubio C, Slezak P. Small, flat colorectal neoplasias in long-standing ulcerative colitis detected by high-resolution electronic video endoscopy. Gastrointestinal Endoscopy 1996;44:15-22.
47. Axelrad AM, Fleischer DE, Geller AJ, Nguyen CC, Lewis JH, Al-Kawas FH, Avigan MI, Montgomery EA, Benjamin SB. High-resolution chromoendoscopy for the diagnosis of diminutive colon polyps: implications for colon cancer screening. Gastroenterology 1996;110:1253-8.
48. Stevens PD, Lightdale CJ, Green PH, Siegel LM, Garcia-Carrasquillo RJ, Rotterdam H. Combined magnification endoscopy with chromoendoscopy for the evaluation of Barrett's esophagus. Gastrointestinal Endoscopy 1994;40:747-9.
49. Kumagai Y, Inoue H, Nagai K, Kawano T, Iwai T. Magnifying endoscopy, stereoscopic microscopy, and the microvascular architecture of superficial esophageal carcinoma. Endoscopy 2002;34:369-75.
50. American Cancer Society: Testing Biopsy and Cytology Specimens for Cancer. 2004.
51. Tearney GJ, Brezinski ME, Bouma BE, Boppart SA, Pitris C, Southern JF, Fujimoto JG. In vivo endoscopic optical biopsy with optical coherence tomography. Science 1997;276:2037-9.
52. Boppart SA, Bouma BE, Pitris C, Tearney GJ, Fujimoto JG, Brezinski ME. Forward-imaging instruments for optical coherence tomography. Optics Letters 1997;22:1618-20.
53. Li XD, Chudoba C, Ko T, Pitris C, Fujimoto JG. Imaging needle for optical coherence tomography. Optics Letters 2000;25:1520-2.
54. Puliafito CA, Hee MR, Lin CP, Reichel E, Schuman JS, Duker JS, Izatt JA, Swanson EA, Fujimoto JG. Imaging of macular diseases with optical coherence tomography. Ophthalmology 1995;102:217-29.
55. Hee MR, Puliafito CA, Wong C, Duker JS, Reichel E, Schuman JS, Swanson EA, Fujimoto JG. Optical coherence tomography of macular holes. Ophthalmology 1995;102:748-56.

56. Hee MR, Izatt JA, Swanson EA, Huang D, Lin CP, Schuman JS, Puliafito CA, Fujimoto JG. Optical coherence tomography of the human retina. Archives of Ophthalmology 1995;113:325-32.
57. Hee MR, Puliafito CA, Duker JS, Reichel E, Coker JG, Wilkins JR, Schuman JS, Swanson EA, Fujimoto JG. Topography of diabetic macular edema with optical coherence tomography. Ophthalmology 1998;105:360-70.
58. Schuman JS, Pedut-Kloizman T, Hertzmark E, Hee MR, Wilkins JR, Coker JG, Puliafito CA, Fujimoto JG, Swanson EA. Reproducibility of nerve fiber layer thickness measurements using optical coherence tomography. Ophthalmology 1996;103:1889-98.
59. Hee MR, Baumal CR, Puliafito CA, Duker JS, Reichel E, Wilkins JR, Coker JG, Schuman JS, Swanson EA, Fujimoto JG. Optical coherence tomography of age-related macular degeneration and choroidal neovascularization. Ophthalmology 1996;103:1260-70.
60. Brezinski ME, Tearney GJ, Weissman NJ, Boppart SA, Bouma BE, Hee MR, Weyman AE, Swanson EA, Southern JF, Fujimoto JG. Assessing atherosclerotic plaque morphology: Comparison of optical coherence tomography and high frequency intravascular ultrasound. British Heart Journal 1997;77:397-404.
61. Brezinski ME, Tearney GJ, Bouma BE, Boppart SA, Hee MR, Swanson EA, Southern JF, Fujimoto JG. High-resolution imaging of plaque morphology with optical coherence tomography. Circulation 1995;92:103-.
62. Grube E, Gerckens U, Buellesfeld L, Fitzgerald PJ. Images in cardiovascular medicine. Intracoronary imaging with optical coherence tomography: a new high-resolution technology providing striking visualization in the coronary artery. Circulation 2002;106:2409-10.
63. MacNeill BD, Jang IK, Bouma BE, Iftimia N, Takano M, Yabushita H, Shishkov M, Kauffman CR, Houser SL, Aretz HT, DeJoseph D, Halpern EF, Tearney GJ. Focal and multi-focal plaque macrophage distributions in patients with acute and stable presentations of coronary artery disease. Journal of the American College of Cardiology 2004;44:972-9.
64. Sivak MV, Jr., Kobayashi K, Izatt JA, Rollins AM, Ung-Runyawee R, Chak A, Wong RC, Isenberg GA, Willis J. High-resolution endoscopic imaging of the GI tract using optical coherence tomography. Gastrointestinal Endoscopy 2000;51:474-9.
65. Jackle S, Gladkova N, Feldchtein F, Terentieva A, Brand B, Gelikonov G, Gelikonov V, Sergeev A, Fritscher-Ravens A, Freund J, Seitz U, Schroder S, Soehendra N. In vivo endoscopic optical coherence tomography of esophagitis, Barrett's esophagus, and adenocarcinoma of the esophagus. Endoscopy 2000;32:750-5.
66. Jackle S, Gladkova N, Feldchtein F, Terentieva A, Brand B, Gelikonov G, Gelikonov V, Sergeev A, Fritscher-Ravens A, Freund J, Seitz U, Soehendra S, Schrodern N. In vivo endoscopic optical coherence tomography of the human gastrointestinal tract--toward optical biopsy. Endoscopy 2000;32:743-9.
67. Li XD, Boppart SA, Van Dam J, Mashimo H, Mutinga M, Drexler W, Klein M, Pitris C, Krinsky ML, Brezinski ME, Fujimoto JG. Optical coherence tomography: advanced technology for the endoscopic imaging of Barrett's esophagus. Endoscopy 2000;32:921-30.
68. Brand S, Poneros JM, Bouma BE, Tearney GJ, Compton CC, Nishioka NS. Optical coherence tomography in the gastrointestinal tract. Endoscopy 2000;32:796-803.

69. Bouma BE, Tearney GJ, Compton CC, Nishioka NS. High-resolution imaging of the human esophagus and stomach in vivo using optical coherence tomography. Gastrointestinal Endoscopy 2000;51:467-74.
70. Das A, Sivak MV, Jr., Chak A, Wong RC, Westphal V, Rollins AM, Willis J, Isenberg G, Izatt JA. High-resolution endoscopic imaging of the GI tract: a comparative study of optical coherence tomography versus high-frequency catheter probe EUS. Gastrointestinal Endoscopy 2001;54:219-24.
71. Zuccaro G, Gladkova N, Vargo J, Feldchtein F, Zagaynova E, Conwell D, Falk G, Goldblum J, Dumot J, Ponsky J, Gelikonov G, Davros B, Donchenko E, Richter J. Optical coherence tomography of the esophagus and proximal stomach in health and disease. American Journal of Gastroenterology 2001;96:2633-9.
72. Poneros JM, Brand S, Bouma BE, Tearney GJ, Compton CC, Nishioka NS. Diagnosis of specialized intestinal metaplasia by optical coherence tomography. Gastroenterology 2001;120:7-12.
73. Pfau PR, Sivak MV, Jr., Chak A, Kinnard M, Wong RC, Isenberg GA, Izatt JA, Rollins A, Westphal V. Criteria for the diagnosis of dysplasia by endoscopic optical coherence tomography. Gastrointestinal Endoscopy 2003;58:196-202.
74. Hameeteman W, Tytgat GN, Houthoff HJ, van den Tweel JG. Barrett's esophagus: development of dysplasia and adenocarcinoma. Gastroenterology 1989;96:1249-56.
75. Fearon ER, Vogelstein B. A genetic model for colorectal tumorigenesis. Cell 1990;61:759-67.
76. Kudo S, Tamura S, Nakajima T, Yamano H, Kusaka H, Watanabe H. Diagnosis of colorectal tumorous lesions by magnifying endoscopy. Gastrointestinal Endoscopy 1996;44:8-14.
77. Guelrud M, Ehrlich EE. Endoscopic classification of Barrett's esophagus. Gastrointestinal Endoscopy 2004;59:58-65.
78. Schmitt JM, Kumar G. Optical scattering properties of soft tissue, a discrete particle model. Applied Optics 1998;37:2788-97.
79. Mourant JR, Freyer JP, Hielscher AA, Eick AA, Shen D, Johnson TM. Mechanisms of light scattering from biological cells relevant to noninvasive optical-tissue diagnostics. Applied Optics 1998;37:3586-93.
80. Saidi IS, Jacques SL, Tittel FK. Mie and Rayleigh modeling of visible-light scattering in neonatal skin. Applied Optics 1995;34:7410-8.
81. Lee TM, Oldenburg AL, Sitafalwalla S, Marks DL, Luo W, Toublan FJ, Suslick KS, Boppart SA. Engineered microsphere contrast agents for optical coherence tomography. Optics Letters 2003;28:1546-8.
82. Xu C, Ye J, Marks DL, Boppart SA. Near-infrared dyes as contrast-enhancing agents for spectroscopic optical coherence tomography. Optics Letters 2004;29:1647-9.
83. Yang C, McGuckin LE, Simon JD, Choma MA, Applegate BE, Izatt JA. Spectral triangulation molecular contrast optical coherence tomography with indocyanine green as the contrast agent. Optics Letters 2004;29:2016-8.
84. Adler D, Ko TH, Herz PR, Fujimoto JG. Optical coherence tomography contrast enhancement using spectroscopic analysis with spectral autocorrelation. Optics Express 2004;12:5487-501.

85. Bouma B, Tearney GJ, Boppart SA, Hee MR, Brezinski ME, Fujimoto JG. High-resolution optical coherence tomographic imaging using a mode-locked Ti-Al_2O_3 laser source. Optics Letters 1995;20:1486-8.
86. Drexler W, Morgner U, Kartner FX, Pitris C, Boppart SA, Li XD, Ippen EP, Fujimoto JG. In vivo ultrahigh-resolution optical coherence tomography. Optics Letters 1999;24:1221-3.
87. Hartl I, Li XD, Chudoba C, Ghanta RK, Ko TH, Fujimoto JG, Ranka JK, Windeler RS. Ultrahigh-resolution optical coherence tomography using continuum generation in an air-silica microstructure optical fiber. Optics Letters 2001;26:608-10.
88. Povazay B, Bizheva K, Unterhuber A, Hermann B, Sattmann H, Fercher AF, Drexler W, Apolonski A, Wadsworth WJ, Knight JC, Russell PSJ, Vetterlein M, Scherzer E. Submicrometer axial resolution optical coherence tomography. Optics Letters 2002;27:1800-2.
89. Wang YM, Zhao YH, Nelson JS, Chen ZP, Windeler RS. Ultrahigh-resolution optical coherence tomography by broadband continuum generation from a photonic crystal fiber. Optics Letters 2003;28:182-4.
90. Kowalevicz AM, Ko T, Hartl I, Fujimoto JG, Pollnau M, Salathe RP. Ultrahigh resolution optical coherence tomography using a superluminescent light source. Optics Express 2002;10:349-53.
91. Unterhuber A, Povazay B, Hermann B, Sattmann H, Drexler W, Yakovlev V, Tempea G, Schubert C, Anger EM, Ahnelt PK, Stur M, Morgan JE, Cowey A, Jung G, Le T, Stingl A. Compact, low-cost Ti:Al_2O_3 laser for in vivo ultrahigh-resolution optical coherence tomography. Optics Letters 2003;28:905-7.
92. Bizheva K, Povazay B, Hermann B, Sattmann H, Drexler W, Mei M, Holzwarth R, Hoelzenbein T, Wacheck V, Pehamberger H. Compact, broad-bandwidth fiber laser for sub-2-micron axial resolution optical coherence tomography in the 1300-nm wavelength region. Optics Letters 2003;28:707-9.
93. Schmitt JM, Knuttel A, Yadlowsky M, Eckhaus MA. Optical coherence tomography of a dense tissue - statistics of attenuation and backscattering. Physics in Medicine and Biology 1994;39:1705-20.
94. Bouma B, Tearney G, Bilinsky I, Golubovic B, Fujimoto J. Self phase modulated Kerr-lens mode locked Cr:forsterite laser source for optical coherence tomography. Optics Letters 1996;21:1839-41.
95. Wang Y, Nelson JS, Chen Z, Reiser BJ, Chuck RS, Windeler RS. Optimal wavelength for ultrahigh-resolution optical coherence tomography. Optics Express 2003;11.
96. Bourquin S, Aguirre AD, Hartl I, Hsiung P, Ko TH, Fujimoto JG, Birks TA, Wadsworth WJ, Bunting U, Kopf D. Ultrahigh resolution real time OCT imaging using a compact femtosecond Nd:glass laser and nonlinear fiber. Optics Express 2003;11:3290-7.
97. Corwin KL, Newbury NR, Dudley JM, Coen S, Diddams SA, Weber K, Windeler RS. Fundamental noise limitations to supercontinuum generation in microstructure fiber. Physical Review Letters 2003;90:113904-1.
98. Provino L, Dudley JM, Maillotte H, Grossard N, Windeler RS, Eggleton BJ. Compact broadband continuum source based on microchip laser pumped microstructured fibre. Electronics Letters 2001;37:558-60.
99. Champert PA, Popov SV, Taylor JR. Generation of multiwatt, broadband continua in holey fibers. Optics Letters 2002;27:122-4.

100. Avdokhin AV, Popov SV, Taylor JR. Continuous-wave, high-power, Raman continuum generation in holey fibers. Optics Letters 2003;28:1353-5.
101. Abbas GL, Chan VWS, Yee TK. Local-oscillator excess-noise suppression for homodyne and heterodyne detection. Optics Letters 1983;8:419-21.
102. Knuttel A, Boehlau-Godau M. Spatially confined and temporally resolved refractive index and scattering evaluation in human skin performed with optical coherence tomography. Journal of Biomedical Optics 2000;5:83-92.
103. Brezinski ME, Tearney GJ, Bouma BE, Izatt JA, Hee MR, Swanson EA, Southern JF, Fujimoto JG. Optical coherence tomography for optical biopsy: properties and demonstration of vascular pathology. Circulation 1996;93:1206-13.
104. Izatt JA, Hsing-Wen W, Kulkarni M, Kobayashi K, Canto MI, Sivak MV. Optical coherence tomography and microscopy in gastrointestinal tissues. OSA Trends in Optics and Photonics on Advances in Optical Imaging and Photon Migration 1996;2:203-6.
105. Tearney GJ, Brezinski ME, Southern JF, Bouma BE, Boppart SA, Fujimoto JG. Optical biopsy in human urologic tissue using optical coherence tomography. Journal of Urology 1997;157:1915-9.
106. Tearney GJ, Brezinski ME, Southern JF, Bouma BE, Boppart SA, Fujimoto JG. Optical biopsy in human gastrointestinal tissue using optical coherence tomography. American Journal of Gastroenterology 1997;92:1800-4.
107. Kobayashi K, Izatt JA, Kulkarni MD, Willis J, Sivak MV, Jr. High-resolution cross-sectional imaging of the gastrointestinal tract using optical coherence tomography: preliminary results. Gastrointestinal Endoscopy 1998;47:515-23.
108. Tearney GJ, Brezinski ME, Southern JF, Bouma BE, Boppart SA, Fujimoto JG. Optical biopsy in human pancreatobiliary tissue using optical coherence tomography. Digestive Disease Sciences 1998;43:1193-9.
109. D'Amico AV, Weinstein M, Li X, Richie JP, Fujimoto J. Optical coherence tomography as a method for identifying benign and malignant microscopic structures in the prostate gland. Urology 2000;55:783-7.
110. Sergeev AM, Gelikonov VM, Gelikonov GV, Feldchtein FI, Kuranov RV, Gladkova ND, Shakhova NM, Snopova LB, Shakov AV, Kuznetzova IA, Denisenko AN, Pochinko VV, Chumakov YP, Streltzova OS. In vivo endoscopic OCT imaging of precancer and cancer states of human mucosa. Optics Express 1997;1:432-40.
111. Cilesiz I, Fockens P, Kerindongo R, Faber D, Tytgat G, Ten Kate F, Van Leeuwen T. Comparative optical coherence tomography imaging of human esophagus: how accurate is localization of the muscularis mucosae? Gastrointestinal Endoscopy 2002;56:852-7.
112. Anger EM, Unterhuber A, Hermann B, Sattmann H, Schubert C, Morgan JE, Cowey A, Ahnelt PK, Drexler W. Ultrahigh resolution optical coherence tomography of the monkey fovea. Identification of retinal sublayers by correlation with semithin histology sections. Experimental eye research 2004;78:1117-25.
113. Wang RK, Xu X, Tuchin VV, Elder JB. Concurrent enhancement of imaging depth and contrast for optical coherence tomography by hyperosmotic agents. Journal of the Optical Society of America B (Optical Physics) 2001;18:948-53.
114. Palmer GM, Marshek CL, Vrotsos KM, Ramanujam N. Optimal methods for fluorescence and diffuse reflectance measurements of tissue biopsy samples. Lasers in Surgery and Medicine 2002;30:191-200.

115. Wang RK, Elder JB. Propylene glycol as a contrasting agent for optical coherence tomography to image gastrointestinal tissues. Lasers Surg Med 2002;30:201-8.
116. Shen B, Zuccaro G, Gramlich TL, Gladkova N, Lashner BA, Delaney CP, Connor JT, Remzi FH, Kareta M, Bevins CL, Feldchtein F, Strong SA, Bambrick ML, Trolli P, Fazio VW. Ex vivo histology-correlated optical coherence tomography in the detection of transmural inflammation in Crohn's disease. Clin Gastroenterol Hepatol 2004;2:754-60.
117. Izatt JA, Kulkarni MD, Wang HW, Kobayashi K, Sivak MV. Optical coherence tomography and microscopy in gastrointestinal tissues. IEEE Journal of Selected Topics in Quantum Electronics 1996;2:1017-28.
118. Pantanowitz L, Hsiung PL, Ko TH, Schneider K, Herz PR, Fujimoto JG, Raza S, Connolly JL. High-resolution imaging of the thyroid gland using optical coherence tomography. Head Neck 2004;26:425-34.
119. MacDonald DG. Comparison of epithelial dysplasia in hamster cheek pouch carcinogenesis and human oral mucosa. Journal of Oral Pathology 1981;10:186-91.
120. Coghlan L, Utzinger U, Drezek R, Heintzelman D, Zuluaga A, Brookner C, Richards-Koryum R, Gimenez-Conti I, Follen M. Optimal fluorescence excitation wavelengths for detection of squamous intra-epithelial neoplasia: results from an animal model. Optics Express 2000;7.
121. Coghlan L, Utzinger U, Richards-Kortum R, Brookner C, Zuluaga A, Gimenez-Conti I, Follen M. Fluorescence spectroscopy of epithelial tissue throughout the dysplasia-carcinoma sequence in an animal model: spectroscopic changes precede morphologic changes. Lasers in Surgery and Medicine 2001;29:1-10.
122. Matheny ES, Hanna NM, Jung WG, Chen Z, Wilder-Smith P, Mina-Araghi R, Brenner M. Optical coherence tomography of malignancy in hamster cheek pouches. Journal of Biomedical Optics 2004;9:978-81.
123. Wilder-Smith P, Jung W-G, Brenner M, Osann K, Beydoun H, Messadi D, Chen Z. In vivo optical coherence tomography for the diagnosis of oral malignancy. Lasers in Surgery and Medicine 2004;35:269-75.
124. Pearse AGE. Histochemistry, theoretical and applied. Church Livingstone, 1991.
125. Start RD, Layton CM, Cross SS, Smith JH. Reassessment of the rate of fixative diffusion. Journal of Clinical Pathology 1992;45:1120-1.
126. Ghoshal NG, Bal HS. Histomorphology of the hamster cheek pouch. Laboratory Animals 1990;24:228-33.
127. Gloesmann M, Hermann B, Schubert C, Sattmann H, Ahnelt PK, Drexler W. Histologic correlation of pig retina radial stratification with ultrahigh-resolution optical coherence tomography. Investigative Ophthalmology & Visual Science 2003;44:1696-703.
128. Goldstein NS, Soman A, Sacksner J. Disparate surgical margin lengths of colorectal resection specimens between in vivo and in vitro measurements. The effects of surgical resection and formalin fixation on organ shrinkage. American Journal of Clinical Pathology 1999;111:349-51.
129. He Y, Wang RK. Dynamic optical clearing effect of tissue impregnated with hyperosmotic agents and studied with optical coherence tomography. Journal of Biomedical Optics 2004;9:200-6.
130. Schmitt JM, Lee SL, Yung KM. An optical coherence microscope with enhanced resolving power in thick tissue. Optics Communications 1997;142:203-7.

131. Kneafsey B, Gillen P, Brady MP. Limitations of thyroid scanning in solitary thyroid nodules. Irish Journal of Medical Science 1994;163:451-4.
132. Jennings AS. Non-isotopic techniques for imaging the thyroid. In: Braverman LE, Utiger RD. Werner and Ingbar's The Thyroid (7th edition). Lippincot-Raven Publishers, 1996.
133. Kountakis SE, Skoulas IG, Maillard AA. The radiologic work-up in thyroid surgery: fine-needle biopsy versus scintigraphy and ultrasound. Ear Nose and Throat Journal 2002;81:151-4.
134. Chan F-Y, Chau MT, Pun T-C, Lam C, Ngan HYS, Leong L, Wong RLC. Limitations of transvaginal sonography and color Doppler imaging inthe differentiation of endometrial carcinoma from benign lesions. J. Ultrasound Med. 1994;13:623-8.
135. Boppart SA, Bouma BE, Pitris C, Tearney GJ, Southern JF, Brezinski ME, Fujimoto JG. Intraoperative assessment of microsurgery with three-dimensional optical coherence tomography. Radiology 1998;208:81-6.
136. Fujimoto JG, Pitris C, Boppart SA, Brezinski ME. Optical coherence tomography: an emerging technology for biomedical imaging and optical biopsy. Neoplasia 2000;2:9-25.
137. Bouma BE, Tearney GJ. Clinical imaging with optical coherence tomography. Academic Radiology 2002;9:942-53.
138. Larson PR, Ingbar SH. The thyroid gland. In: Wilson JD, Foster DW. Williams textbook of endocrinology (8th edition). W.B. Saunders Company, 1992.
139. Koike E, Noguchi S, Yamashita H, Murakami T, Ohshima A, Kawamoto H. Ultrasonographic characteristics of thyroid nodules: prediction of malignancy. Archives of Surgery 2001;136:334-7.
140. Weber AL, Randolph G, Aksoy FG. The thyroid and parathyroid glands. CT and MR imaging and correlation with pathology and clinical findings. Radiologic Clinics of North America 2000;38:1105-29.
141. Carcangiu ML. Thyroid. In: Sternberg SS. Histology for pathologists (2nd edition). Lippincott-Raven Publishers, 1997.
142. Rosai J, Carcangiu ML, DeLillis RA. Tumors of the thyroid gland. Atlas of tumor pathology (3rd series). Armed Forces Institute of Pathology, 1992.
143. Boppart SA, Bouma BE, Pitris C, Southern JF, Brezinski ME, Fujimoto JG. In vivo cellular optical coherence tomography imaging. Nature Medicine 1998;4:861-5.
144. Yazdanfar S, Rollins AM, Izatt JA. Imaging and velocimetry of the human retinal circulation with color Doppler optical coherence tomography. Optics Letters 2000;25:1448-50.
145. Zhao Y, Chen Z, Saxer C, Xiang S, de Boer JF, Nelson JS. Phase-resolved optical coherence tomography and optical Doppler tomography for imaging blood flow in human skin with fast scanning speed and high velocity sensitivity. Optics Letters 2000;25:114-6.
146. Kobayashi K, Sivak MV, Jr. Flat adenoma: are western colonoscopists careful enough? Endoscopy 1998;30:487-9.
147. Fujii T, Rembacken BJ, Dixon MF, Yoshida S, Axon AT. Flat adenomas in the United Kingdom: are treatable cancers being missed? Endoscopy 1998;30:437-43.
148. Fujimoto JG. Optical coherence tomography for ultrahigh resolution in vivo imaging. Nature Biotechnology 2003;21:1361-7.
149. Feldchtein FI, Gelikonov GV, Gelikonov VM, Kuranov RV, Sergeev A, Gladkova ND, Shakhov AV, Shakova NM, Snopova LB, Terent'eva AB, Zagainova EV, Chumakov YP,

Kuznetzova IA. Endoscopic applications of optical coherence tomography. Optics Express 1998;3:257-70.
150. Rollins AM, Ung-arunyawee R, Chak A, Wong CK, Kobayashi K, Sivak MV, Izatt JA. Real-time in vivo imaging of human gastrointestinal ultrastructure by use of endoscopic optical coherence tomography with a novel efficient interferometer design. Optics Letters 1999;24:1358-60.
151. Bouma BE, Tearney GJ. Power-efficient nonreciprocal interferometer and linear-scanning fiber-optic catheter for optical coherence tomography. Optics Letters 1999;24:531-3.
152. Seitz U, Freund J, Jackle S, Feldchtein F, Bohnacker S, Thonke F, Gladkova N, Brand B, Schroder S, Soehendra N. First in vivo optical coherence tomography in the human bile duct. Endoscopy 2001;33:1018-21.
153. Poneros JM, Tearney GJ, Shiskov M, Kelsey PB, Lauwers GY, Nishioka NS, Bouma BE. Optical coherence tomography of the biliary tree during ERCP. Gastrointestinal Endoscopy 2002;55:84-8.
154. Herz PR, Chen Y, Aguirre A, Fujimoto JG, Mashimo H, Schmitt JM, Koski A, Goodnow J, Petersen C. Ultrahigh resolution optical biopsy with endoscopic optical coherence tomography. Optics Express 2004;12:3532-42.
155. Drexler W, Morgner U, Ghanta RK, Kaertner FX, Schuman JS, Fujimoto JG. Ultrahigh resolution ophthalmic optical coherence tomography. Nature Medicine 2001;7:502-7.
156. Schmitt JM, Xiang SH, Yung KM. Speckle in optical coherence tomography. Journal of Biomedical Optics 1999;4:95-105.
157. Ilday FO, Lim H, Buckley JR, Wise FW. Practical all-fiber source of high-power, 120-fs pulses at 1 μm. Optics Letters 2003;28:1362-4.
158. Herz PR, Chen Y, Aguirre A, Schneider K, Hsiung P. Micromotor endoscope catheter for in vivo ultrahigh resolution optical coherence tomography. Optics Letters 2004;29:2261-3.
159. Aguirre AD, Hsiung P, Ko TH, Hartl I, Fujimoto JG. High-resolution optical coherence microscopy for high-speed, in vivo cellular imaging. Optics Letters 2003;28:2064-6.
160. Wang TD, Mandella MJ, Contag CH, Kino GS. Dual-axis confocal microscope for high-resolution in vivo imaging. Optics Letters 2003;28:414-16.
161. Kato S, Fujii T, Koba I, Sano Y, Fu KI, Parra-Blanco A, Tajiri H, Yoshida S, Rembacken B. Assessment of colorectal lesions using magnifying colonoscopy and mucosal dye spraying: can significant lesions be distinguished? Endoscopy 2001;33:306-10.
162. Hurlstone DP, Cross SS, Adam I, Shorthouse AJ, Brown S, Sanders DS, Lobo AJ. Efficacy of high magnification chromoscopic colonoscopy for the diagnosis of neoplasia in flat and depressed lesions of the colorectum: a prospective analysis. Gut 2004;53:284-90.
163. Hurlstone DP, Cross SS, Drew K, Adam I, Shorthouse AJ, Brown S, Sanders DS, Lobo AJ. An evaluation of colorectal endoscopic mucosal resection using high-magnification chromoscopic colonoscopy: a prospective study of 1000 colonoscopies. Endoscopy 2004;36:491-8.
164. Hurlstone DP, Cross SS, Brown S, Sanders DS, Lobo AJ. A prospective evaluation of high-magnification chromoscopic colonoscopy in predicting completeness of EMR. Gastrointestinal Endoscopy 2004;59:642-50.

165. Choma MA, Sarunic MV, Yang C, Izatt JA. Sensitivity advantage of swept sournce and Fourier domain optical coherence tomography. Optics Express 2003;11:2183-9.
166. Yun SH, Tearney GJ, de Boer JF, Iftimia N, Bouma BE. High-speed optical frequency-domain imaging. Optics Express 2003;11:2953-63.
167. Yun SH, Tearney GJ, Bouma BE, Park BH, de Boer JF. High-speed spectral-domain optical coherence tomography at 1.3 mu m wavelength. Optics Express 2003;11:3598-604.
168. Nassif NA, Cense B, Park BH, Pierce MC, Yun SH, Bouma BE, Tearney GJ, Chen TC, de Boer JF. In vivo high-resolution video-rate spectral-domain optical coherence tomography of the human retina and optic nerve. Optics Express 2004;12:480-2.
169. Leitgeb RA, Drexler W, Unterhuber A, Hermann B, Bajraszewski T, Le T, Stingl A, Fercher AF. Ultrahigh resolution Fourier domain optical coherence tomography. Optics Express 2004;12:2156-65.
170. Nassif NA, Cense B, Park BH, Yun SH, Chen TC, Bouma BE, Tearney GJ, de Boer JF. In vivo human retinal imaging by ultrahigh-speed spectral domain optical coherence tomography. Optics Letters 2004;29:480-2.
171. Wojtkowski M, Srinivasan VJ, Ko TH, Fujimoto JG, Kowalczyk A, Duker JS. Ultrahigh-resolution, high-speed, Fourier domain optical coherence tomography and methods for dispersion compensation. Optics Express 2004;12:2404-22.
172. Pan Y, Xie H, Fedder GK. Endoscopic optical coherence tomography based on a microelectromechanical mirror. Optics Letters 2001;26:1966-8.
173. Helmchen F, Fee M, Tank D, Denk W. A miniature head-mounted two-photon microscope: High-resolution brain imaging in freely moving animals. Neuron 2001;31:903-12.
174. Zara JM, Yazdanfar S, Rao KD, Izatt JA, Smith SW. Electrostatic micromachine scanning mirror for optical coherence tomography. Optics Letters 2003;28:628-30.
175. Liu X, Cobb MJ, Chen Y, Kimmey MB, Li XD. Rapid-scanning forward-imaging miniature endoscope for real-time optical coherence tomography. Optics Letters 2004;29:1763-5.
176. Palombini L, Fulciniti F, Vetrani A, De Rosa G, Di Benedetto G, Zeppa P, Troncone G. Fine-needle aspiration biopsies of breast masses. A critical analysis of 1956 cases in 8 years (1976-1984). Cancer 1988;61:2273-7.
177. Zajdela A, Ghossein NA, Pilleron JP, Ennuyer A. The value of aspiration cytology in the diagnosis of breast cancer: experience at the Fondation Curie. Cancer 1975;35:499-506.
178. McMahon AJ, Lutfy AM, Matthew A, Walls AD, McOrmick JS, Henderson MA, Auld CD. Needle core biopsy of the breast with a spring-loaded device. Br J Surg 1992;79:1042-5.
179. Shah VI, Raju U, Chitale D, Deshpande V, Gregory N, Strand V. False-negative core needle biopsies of the breast: an analysis of clinical, radiologic, and pathologic findings in 27 concecutive cases of missed breast cancer. Cancer 2003;97:1824-31.
180. Chare MJ, Flowers CI, O'Brien CJ, Dawson A. Image-guided core biopsy in patients with breast disease. Br J Surg 1996;83:1415-6.
181. Anscher MS, Jones P, Prosnitz LR, Blackstock W, Hebert M, Reddick R, Tucker A, Dodge R, Leight G, Jr., Iglehart JD, et al. Local failure and margin status in early-stage breast carcinoma treated with conservation surgery and radiation therapy. Ann Surg 1993;218:22-8.

182. Pittinger TP, Maronian NC, Poulter CA, Peacock JL. Importance of margin status in outcome of breast-conserving surgery for carcinoma. Surgery 1994;116:605-8; discussion 8-9.
183. Park CC, Mitsumori M, Nixon A, Recht A, Connolly J, Gelman R, Silver B, Hetelekidis S, Abner A, Harris JR, Schnitt SJ. Outcome at 8 years after breast-conserving surgery and radiation therapy for invasive breast cancer: influence of margin status and systemic therapy on local recurrence. J Clin Oncol 2000;18:1668-75.
184. Sabel MS, Pierce LJ. Masectomy and breast conserving therapy for invasive breast cancer. UpToDate. Wellesley, 2004.
185. Schneebaum S, Even-Sapir E, Cohen M, Shacham-Lehrman H, Gat A, Brazovsky E, Livshitz G, Stadler J, Skornick Y. Clinical applications of gamma-detection probes - radioguided surgery. Eur J Nucl Med 1999;26:S26-35.
186. Veronesi U, Paganelli G, Viale G, Luini A, Zurrida S, Galimberti V, Intra M, Veronesi P, Robertson C, Maisonneuve P, Renne G, De Cicco C, De Lucia F, Gennari R. A randomized comparison of sentinel-node biopsy with routine axillary dissection in breast cancer. New England Journal of Medicine 2003;349:546-53.
187. Boppart SA, Herrmann JM, Fujimoto JG. Optical coherence tomography: Applications in surgical diagnosis, guidance and intervention. Medical Imaging International 2000;10:14-20.
188. Hsiung P, Schneider K, Herz PR, Bourquin S, Ko TH, Li XD, Fujimoto JG, Weinstein M, Hirsch M, D'Amico AV, Richie JP. Ultrahigh resolution OCT of prostate pathology in the clinic using a portable Cr:forsterite laser, In SPIE Photonics West - BIOS, San Jose, CA, January 2003, SPIE Int. Soc. Opt. Eng. Proceedings of Spie the International Society for Optical Engineering, 2003.
189. Matsunaga T, Ohta D, Misaka T, Hosokawa K, Fujii M, Kaise H, Kusama M, Koyanagi Y. Mammary ductoscopy for diagnosis and treatment of intraductal lesions of the breast. Breast Cancer 2001;8:213-21.
190. Boppart SA, Luo W, Marks DL, Singletary KW. Optical coherence tomography: feasibility for basic research and image-guided surgery of breast cancer. Breast Cancer Research and Treatment 2004;84:85-97.
191. Slaga TJ, Gimenez-Conti IB. An animal model for oral cancer. J Natl Cancer Inst Monogr 1992:55-60.
192. Gimenez-Conti IB, Slaga TJ. The hamster cheek pouch model of carcinogenesis and chemoprevention. Advances in Experimental Medicine and Biology 1992;320:63-7.
193. Gimenez-Conti IB, Slaga TJ. The hamster cheek pouch carcinogenesis model. J Cell Biochem Suppl 1993;17F:83-90.
194. Andrejevic S, Savary J-F, Fontolliet C, Monnier P, Van Den Bergh H. 7,12-Dimethylbenz[a]anthracene-induced 'early' squamous cell carcinoma in the Golden Syrian Hamster: evaluationof an animal model and comparison with 'early' forms of human squamous cell carcinoma inthe upper aero-digestive tract. Int. J. Exp. Path. 1996;77:7-14.
195. Pathak I, Davis NL, Hsiang YN, Q NF, Palcic B. Detection of squamous neoplasia by fluorescence imaging comparing porfimer sodium fluoresence to tissue autofluorescence in the hamster cheek pouch model. American Journal of Medicine 1995;170:423-6.

196. Guo Y, Savage HE, Liu F, Schantz SP, Ho PP, Alfano RR. Subsurface tumor progression investigated by noninvasive optical second harmonic tomography. Proc Natl Acad Sci U S A 1999;96:10854-6.
197. Ebihara A, Krasieva TB, Liaw LH, Fago S, Messadi D, Osann K, Wilder-Smith P. Detection and diagnosis of oral cancer by light-induced fluorescence. Lasers Surg Med 2003;32:17-24.
198. Wang CY, Tsai T, Chen HC, Chang SC, Chen CT, Chiang CP. Autofluorescence spectroscopy for in vivo diagnosis of DMBA-induced hamster buccal pouch pre-cancers and cancers. Journal of Oral Pathology and Medicine 2003;32:18-24.
199. Wilder-Smith P, Osann K, Hanna N, El Abbadi N, Brenner M, Messadi D, Krasieva T. In vivo multiphoton fluorescence imaging: a novel approach to oral malignancy. Lasers in Surgery and Medicine 2004;35:96-103.
200. Izatt JA, Hee MR, Owen GM, Swanson EA, Fujimoto JG. Optical Coherence Microscopy in Scattering Media. Optics Letters 1994;19:590-2.
201. Reddy BS, Watanabe K, Weisburger JH. Effect of high-fat diet on colon carcinogenesis in F344 rats treated with 1,2-dimethylhydrazine, methylazoxymethanol acetate, or methylnitrosourea. Cancer Research 1977;37:4156-9.
202. Reddy BS, Tanaka T. Interactions of selenium deficiency, vitamin E, polyunsaturated fat, and saturated fat on azoxymethane-induced colon carcinogenesis in male F344 rats. Journal of the National Cancer Institute 1986;76:1157-62.
203. McLellan E, Medline A, Bird R. Sequential analysis of the growth and morphological characteristics of aberrant crypt foci: putative preneoplastic lesions. Cancer Research 1991;51.
204. Bird R. Observation and quantification of aberrant crypts in the murine colon treated with a colon carcinogen: preliminary findings. Cancer Letters 1987;37.
205. Druckrey E. Carcinoma of the Colon and Antecedent Epithelium. Thomas, 1970.
206. Holt P, Mokuloulu A, Distler P, Liu T, Reddy B. Regional distribution of carcinogen-induced colonic neoplasia in the rat. Nutrition and Cancer 1996;25:129-35.
207. Bi S, Geng B, Yong D. Effects of menadione on 1,2-dimethylhydrazine-induced mouse colon adenocarcinoma. Acta Pharmacologica Sinica 1993;14:17-20.
208. Corpet D, Fabrice P. Point: From animal models to prevention of colon cancer. A systematic review of chemoprevention in min mice and choice of a model system. Cancer Epidemiology 2003;12:391-400.
209. Takayama T, Katsuki S, Takahashi Y, Ohi M, Nojiri S, Sakamaki S, Kato J, Kogawa K, Miyake H, Niitsu Y. Aberrant crypt foci of the colon as precursors of adenoma and cancer. New England Journal of Medicine 1998;339:1277-84.
210. Kim DJ, Kang JS, Ahn B, Kim KS, Park KH, Choi KS, Surh YJ, Kim ND. Chemopreventive effect of 2-(allylthio)pyrazine (2-AP) on rat colon carcinogenesis induced by azoxymethane (AOM). Cancer Letters 2001;166:125-33.
211. Blackstone MO, Riddell RH, Rogers BH, Levin B. Dysplasia-associated lesion or mass (DALM) detected by colonoscopy in long-standing ulcerative colitis: an indication for colectomy. Gastroenterology 1981;80:366-74.
212. McLaren W, Anikijenko P, Barkla D, Delaney TP, King R. In vivo detection of experimental ulcerative colitis in rats using fiberoptic confocal imaging (FOCI). Digestive Diseases and Sciences 2001;46:2263-76.

213. McLaren W, Anikijenko P, Thomas S, Delaney T, King R. In vivo detection of morphological and microvascular changes of the colon in association with colitis using fiberoptic confocal imaging (FOCI). Digestive Disease Sciences 2002;47:2424-33.
214. Tumlinson A, Hariri L, Barton J. Miniature endoscope for a combined OCT-LIF system, In SPIE Conference of Biomedical Optics, San Jose, CA, 2003.

LIST OF FIGURES

Chapter 2 – High-power, Continuous-wave, Raman Continuum Light Source for Optical Coherence Tomography

Chapter 3 – Effect of Tissue Preservation on Imaging using Ultrahigh Resolution Optical Coherence Tomography

Chapter 4 – Ultrahigh Resolution Imaging of the Thyroid Gland using Optical Coherence Tomography

Chapter 5 – Ultrahigh Resolution and Three-Dimensional OCT Imaging of the Large and Small Intestine

Chapter 6 – Ultrahigh Resolution and Three-Dimensional OCT Imaging of Benign and Malignant Lesions in the Human Breast

Chapter 7 – Summary and Conclusions